ANALYTICAL AND EXPERIMENTAL STUDIES OF THERMOELECTRIC DEVICES AND MATERIALS

by

Matthew M. Barry

B.A., University of Pittsburgh, 2010

B.S. in Mechanical Engineering, University of Pittsburgh, 2010

M.S. in Mechanical Engineering, University of Pittsburgh, 2012

Submitted to the Graduate Faculty of
the Swanson School of Engineering in partial fulfillment
of the requirements for the degree of

Doctor of Philosophy

University of Pittsburgh

2016

UNIVERSITY OF PITTSBURGH

SWANSON SCHOOL OF ENGINEERING

This dissertation was presented

by

Matthew M. Barry

It was defended on

December 18, 2015

and approved by

Minking K. Chyu, Ph.D., Associate Dean for International Initiatives, Dean, Sichuan University - Pittsburgh Institute, Leighton and Mary Orr Chair Professor, Department of Mechanical Engineering and Materials Science

Calixto Isaac Garcia, Ph.D.,Ph.D., Research Professor, Department of Mechanical Engineering and Materials Science

Sung Kwon Cho, Ph.D., Associate Professor, Department of Mechanical Engineering and Materials Science

Sangyeop Lee, Ph.D., Assistant Professor, Department of Mechanical Engineering and Materials Science

Dissertation Director: Minking K. Chyu, Ph.D., Associate Dean for International Initiatives, Dean, Sichuan University - Pittsburgh Institute, Leighton and Mary Orr Chair Professor, Department of Mechanical Engineering and Materials Science

ANALYTICAL AND EXPERIMENTAL STUDIES OF THERMOELECTRIC DEVICES AND MATERIALS

Matthew M. Barry, PhD

University of Pittsburgh, 2016

Interest in thermoelectric devices (TEDs) for waste-heat recovery applications has recently increased due to a growing global environmental consciousness and the potential economic benefits of increasing cycle efficiency. Unlike conventional waste-heat recovery systems like the organic Rankine cycle, TEDs are steady-state, scalable apparatus that directly convert a temperature difference into electricity using the Seebeck effect. The benefits of TEDS, namely steady-state operation and scalability, are often outweighed by their low performance in terms of thermal conversion efficiency and power output. To address the issue of poor device performance, this dissertation takes a multi-faceted approach focusing on device modeling, analysis and design and material processing.

First, a complete one-dimensional thermal resistance network is developed to analytically model a TED, including heat exchangers, support structures and thermal and electrical contact resistances. The purpose of analytical modeling is twofold: to introduce an optimization algorithm of the thermoelectric material geometry based upon the realized temperature difference to maximize thermal conversion efficiency and power output; and to identify areas within the conventional TED that can be restructured to allow for a greater temperature difference across the junction and hence increased performance. Additionally, this model incorporates a component on the numerical resolution of radiation view factors within a TED cavity to properly model radiation heat transfer. Results indicate that geometric optimization increases performance upwards of 30% and the hot-side ceramic diminishes realized

temperature difference. The resulting analytical model is validated with published numerical and comparable analytical models, and serves as a basis for experimental studies.

Second, an integrated thermoelectric device is presented. The integrated TED is a re-structured TED that eliminates the hot-side ceramic and directly incorporates the hot-side heat exchanger into the hot-side interconnector, reducing the thermal resistance between source and hot-side junction. A single-state and multi-stage pin-fin integrated TED are developed and tested experimentally, and the performance characteristics are shown for a wide range of operating fluid temperatures and flow rates. Due to the eliminated to thermal restriction, the integrated TED shows unique performance characteristics in comparison to conventional TED, indicating increased performance.

Finally, a grain-boundary engineering approach to material processing of bulk bismuth telluride (Bi_2Te_3) is presented. Using uniaxial compaction and sintering techniques, the preferred crystallographic orientation (PCO) and coherency of grains, respectively, are controlled. The effect of sintering temperature on thermoelectric properties, specifically Seebeck coefficient, thermal conductivity and electrical resistivity, are determined for samples which exhibited the highest PCO. It is shown the performance of bulk Bi_2Te_3 produced by the presented method is comparable to that of nano-structured materials, with a maximum figure of merit of 0.40 attained at 383 K.

TABLE OF CONTENTS

LIST OF TABLES

LIST OF FIGURES

PREFACE

This work is dedicated to my family, friends and colleagues. Without your support, none of this would have been possible. I would like to thank from the bottom of my heart: my parents, who have selflessly supported me in my endeavors through undergraduate and graduate school; my wife who patiently understood the consuming nature of this program and who provided comfort to my often stressed mind; to my late grandparents who made the opportunity of college possible with their love and support; and lastly, my brother for providing enough distractions to keep me grounded.

Through the course of this work, there have been many tremendous graduate and undergraduate students who have lent time, effort and attention to various topics within this thesis. I would like to thank Dr. Youngsoo Jung for his efforts on our two collaborative manuscripts and for being my best friend, mentor and part of my family during our time at the University together. Youngsoo is a truly brilliant and wonderful person to work with and spend time with in and outside of work, becoming like a brother to me. Michael J. Durka, Austen D. Fradeneck and Corey E. Clifford are held with high esteem for their countless hours of conversation spent on course and research topics and for their help in numerical modeling and experimental set-up; without their advice and opinions, much of this would not have been possible. Dr. B. V. K. Reddy; I would like to thank you for being my mentor, colleague and friend over the course of our short time together. Without your patience and guidance, none of this would have been possible. Dr. Parthib Rao, currently of Rice University, you are immeasurably thanked for your friendship and countless hours of providing guidance and insight into problems and topics and for stimulating my thinking and always playing devil's advocate.

Our lab has been graced with some brilliant undergraduate students whom have helped with projects beyond what was ever expected of them. I would like to personally thank Kenechi A. Agbim who is currently at Georgia Tech for her assistance with developing the analytical model used for optimization of thermoelectric unicouples, for her help on building and testing the pin-fin integrated thermoelectric device and for her wonderful friendship which she shared over the course of a year in our laboratory. It was truly a pleasure to work with her on a daily basis. I am indebted to Jonathon Kim for his help on the pin-fin integrated thermoelectric device construction, his two semesters of work on the bismuth telluride material processing project and his friendship both during and after working hours. Jonathon is a truly bright and hardworking student with limitless potential and a fun-loving person with a contagious personality. Over the course of a year, Cain Hung, now at the University of Connecticut, was a marvelous addition to our laboratory. His abilities and analtyical thinking far exceeded most undergraduate and graduate students, making him an invaluable contributor to our material research projects. Justin Ying, whom was with our laboratory on-and-off over the course of four years, is another tremendous student who helped develop studies on diffusion barriers and GPU acceleration of in-house computer codes that transformed an impossible project into something manageable. His abilities and dedication to projects far exceeded what was expected of him and a portion of this thesis would not have been possible within my lifetime without his efforts. There are many other students, too many to list, whom have helped through various senior design groups and although not mentioned, do not go unappreciated.

I would like to thank from the bottom of my heart the staff of this University; they are the backbone of research and without their continued efforts, none of this would have come into existent. Kelly Wodnicki, thank you for putting up with my constant requests for orders and purchasing, room reservations, schedule inquiries and the multitude of remaining items too numerous to count, as well as your friendship. Without you, I would not have been able to function. Thank you to the secretarial staff Heather Manns, Shannon Kelly and Carolyn Chuha; your friendship has been a pleasure and you have made my stay here much less stressful and more enjoyable. Thank you Andrew Holmes and Thorin Tobiassen of SCPI for unfathomable efforts in helping design, evaluate, machine and construct prototypes, lab

equipment and for giving advice on various topics. The time spent in the shop with you both was truly rewarding and enjoyable. Thank you Dr. Susheng Tan of NFCF for your untiring assistance in acquiring the hundreds of high-resolution transmission electron micrographs used throughout our various projects and providing insight into measurement techniques.

Lastly, but not in the least, there are the faculty that I would like to thank. I have great regard for Professor J. K. Lee who has helped collaborate on various projects and manuscripts and whom has provided laboratory facilities. I would like to thank Professor Isaac C. Garcia for his patience and support with out material processing project, and for his guidance and friendship. Dr. Phuoc Tran has been of tremendous help and support on various projects and our time spent together was invaluable. I would like to thank the late Dr. John Metzger who inspired me to pursue graduate school and ignited my passion for science; it was a pleasure to have known him. Lastly, but not in any way the least, I would like to thank Professor Minking K. Chyu for being my adviser over the course of my graduate career and providing insight and suggestions to improve my performance. Your continued and undetermined support motivated me to accomplish all enclosed in this dissertation and our other works.

1.0 INTRODUCTION

This dissertation deals with the multifaceted approach of increasing thermoelectric device performance in terms of efficiency and power output, namely through device modeling, analysis and design, and thermoelectric material processing. It is necessary to provide a historical context of the theory of thermoelectricity and subsequent efforts that have been made toward device design and material processing for increased performance.

1.1 HISTORICAL CONTEXT

Since the industrial revolution, we have developed tremendous technological processes, of which included electrical energy production. Electrical energy production comes in the form of coal, oil and gas fired power plants, boiling and pressurized water nuclear reactors, geothermal, hydro, and photovoltaic (PV) power generation plants and wind turbines, to name some. It is quite evident power production through the usage of fossil fuels has adverse effects in terms of pollution to the environment and the release of greenhouse gases (GHG). The emission of GHG, in the form of carbon dioxide, and more harmful gases like methane, cholorfluorocarbons (CFCs) and nitrous oxide [1, 2] can lead to a change of global climate. Although the levels of GHG, in particular carbon dioxide, are not the highest they have been in the past 60 million years [3], an increase in GHG does lead to a change in the climate, as evidenced by an increase in the global temperature within the past century.

From the start of the 20^{th} century to 1960, the global temperature increased 0.2 °C, and from 1960 to 1980, another 0.2 °C [4]. The global temperature has continued to increase at a rate of 0.15-0.20 °C per decade since the late 1970's [5]. Curbing the emission of greenhouse

gases could mitigate the effects of global climate change [6], therefore much policy-making attention has been devoted to renewable and sustainable energy (RSE) production technologies [7]. Moreover, the decarbonization of electricity generation is not enough to reduce the emission of GHG [8], and RSE technologies need to be developed concurrently to diversify the energy production portfolio [9].

Fossil fuels emit greenhouse gases and waste heat. Based on the DOE's "Waste Heat Recovery" report [10], up to 50% of energy used within industrial applications alone, not considering transportation and other applications powered by fossil fuels, is lost to the environment as waste heat. Although RSE production technologies like PV, concentrated solar power, geothermal, fuel cells and biomass are promising alternatives to fossil-fuel based power generation systems, they have an inherently similar deficiency with the aforementioned fossil-fuel systems: waste heat. Recovering any amount of waste heat and converting it into electrical energy can increase the efficiency of any cycle, device or process while mitigating potential environmental impacts. For fossil-fuel based power generation and transportation, the system can achieve more power output per unit fuel, effectively reducing GHG emissions.

Thermeoelectric devices (TEDs) are well-suited for waste heat recovery applications. These steady-state devices emit no noise, are scalable per application and have long operational lifetimes, making them ideal for various waste heat recovery applications. These devices have a long-standing history with tremendous potential to recover waste heat from any power-production application, or any system that rejects thermal energy.

The theory of thermoelectricity dates back nearly two centuries and has foundations in electromagnetism. The first indication of thermoelectricity, in the form of electromagnetism, was published by Hans Christian Oersted in 1820 when he observed a magnetic compass needle was deflected by the flow of electrical current in an adjacent wire located parallel to the needle [11]. His early experiments on electricity clearly indicated the presence of electromagnetic fields in which a force was produced perpendicular to the direction of current flow within a conductor [12]. Despite his breakthrough in 1820, his discovery of the connection between electricity and magnetism was declared an accident [13] and was later formulated mathematically by the likes of Ampère [14], Faraday [15], Maxwell [16, 17, 18], Heaviside [19, 20, 21, 22] and Hertz [23], providing a complete theory of electromagnetism.

Around the same time as Oersted's discovery, Thomas Johann Seebeck noted that a magnetic compass needle also deflected when near an electrically conducting circuit comprised of two differing materials carrying a current; this deflection was attributed to the temperature difference between the poles (terminals) of the circuit and was termed thermomagnetism [24]. Seebeck ignored the presence of an electrical current generated within the electrical circuit due to the temperature difference across the junction of the dissimilar materials, such as bismuth and tellurium, allowing others to develop his discovery into devices known as thermocouples and thermopiles. Georg Simon Ohm furthered Seebeck's findings by developing the relationship between resistance and current to electromotive force using thermocouples [25, 26], with his work providing the mathematical foundation for the analysis of electrical circuits [27]. Thermopiles, or thermoelectric generators, were then proposed and built based upon Seebeck's and Ohm's work, with Gülcher building a system capable of producing 6 amperes and 4 volts [28] and achieving an efficiency of less than one percent [29]. It is noted that the efficiency of these thermopiles was comparable to coal-fired steam engines at the time.

Building upon Ohm's law, Jean Charles Peltier discovered the passage of current through an electrical circuit comprised of dissimilar conducting materials caused either the absorption or liberation of heat at said junction [30]. Like his predecessors, Peltier was unable to completely see the full thermoelectric phenomena and attributed his findings strictly to Ohm's law. However, in 1838 Heinrich Friedrich Emil Lenz used Peltier's findings to show that heat could be removed from the junction of a bismuth-antimony wire via the application of a voltage potential across the terminals and thus water could be frozen [31].

It was not until William Thomson, later known as Lord Kelvin, that the Seebeck and Peltier effects (first and second thermoelectric effects) were combined into one thermodynamic principle, and thus the discovery of the Thomson effect, which was the third thermoelectric effect [32]. The Thomson effect stated that a homogeneous conductor experiencing a temperature difference and the passage of an electrical current in the same direction as said temperature difference will experience lateral heating or cooling; that is, the temperature difference for a given cross-sectional area in the in-plane direction of current will not be uniform. Although a theory of thermoelectricity was forming from experimental data

and thermodynamic derivations, the importance of using materials with high thermoelectric performance, such as large Seebeck coefficients, was not fully understood as a means of maximizing efficiency.

At the turn of the twentieth century, Edmund Altenkirch derived the basic theory of thermoelectricity and calculated the maximum efficiency and performance of thermoelectric generators [33] and coolers [34]. Altenkirch's studies identified the key parameters necessary for well-performing thermoelectric materials; a high Seebeck coefficient as to produce a large voltage potential per given temperature difference, high electrical conductivity as to minimize Joule heating due to internal resistance and low thermal conductivity as to reduce the amount of heat transferred through the material as to maintain a larger temperature difference across said material. Materials that satisfied each of these requirements were unavailable until the development of semiconductors in the mid-twentieth century.

Abram Ioffe was one of the first to study semiconductor usage for thermoelectric couples, introducing the dimensionless term figure of merit, ZT, which is the ratio of the square of the Seebeck coefficient times the electrical conductivity and absolute temperature $\overline{T}$ over the thermal conductivity [35]. The figure of merit depends on both materials' intrinsic properties and both the hot and cold side temperatures, T_h and T_c, respectively. The combination of these properties for both the p- and n-type materials, evaluated at the average temperature between the cold and hot junction $\overline{T}$, yields the modified dimensionless figure of merit,

$$Z\overline{T} = \frac{(|\alpha_p| + |\alpha_n|)\overline{T}}{[(\rho_p\kappa_p)^{\frac{1}{2}} + (\rho_n\kappa_n)^{\frac{1}{2}}]^2}. \tag{1.1}$$

The thermal conductivity κ is the summation of the electronic and lattice contributions, κ_{e^-} and κ_{ph}, respectively, and ρ is the electrical resistivity, or inverse of electrical conductivity.

Ioffe applied his findings to increasing the performance of thermoelectric materials and devices [36, 37, 38] and quantified the importance of carrier mobility and thermal conductivity [39]. Ioffe's work provided a solid foundation for physicists such as Goldsmid who investigated the performance of bismuth-telluride Peltier coolers which achieved a figure of merit of 0.76 at room temperature [40]. Additionally, Goldsmid found that high mean atomic weight materials provided high Seebeck coefficients, which are favorable for cooling applications [41]. Goldsmid's findings made a strong argument for the use of bismuth-telluride compounds,

which were then studied by Birkholz who alloyed bismuth-telluride with bismuth-selenide and antimony-telluride [42]. The alloyed compounds proposed by Birkholz are still the most commonly used thermoelectric materials to date due to their relatively high figure of merit. Although tremendous progress was made since mid-twentieth century, the figure of merit for bismuth-telluride compounds has not increased substantially since, remaining near unity [43].

1.2 DEVICE PERFORMANCE

Sine the development of moderate performance thermoelectric materials, conventional thermoelectric generators (TEGs) have been studied extensively in terms of waste heat recovery applications, taking the form of analytical, numerical and experimental investigations. Liu et al. [44] provided a summary of the progress and challenges of implementing TEGs for waste heat recovery applications, stating that system efficiency is always reduced due to the temperature drop between source and sink due to device construction (i.e. inclusion of necessary support materials, heat exchangers and interconnectors). Liang et al. [45] have shown the thermal contact resistance between the TED module and heat source and sink affects the power output of a multistage TED by reducing the temperature difference ΔT across the thermoelectric (TE) material. Therefore, design, analysis, optimization and modeling have been pursued to better increase the performance of existing TEG designs, and consequently will be a focus of this dissertation.

In terms of design and optimization of TED systems, cascading and segmenting of TE materials are the best methods for efficiently recovering waste heat from high temperature sources. Cascading optimizes temperature-dependent material properties along the direction of temperature gradient, allowing each material to operate at a temperature difference that maximizes either power output or efficiency. Fujisaka et al. [46] demonstrated that cascaded TEDs can increase the power output by 1.24 times and efficiency by nearly 50% as compared to conventional designs. Kaibe et al. [47] developed a cascaded TEG that was able to achieve a conversion efficiency for 12% over an operational range of 520 °C temperature difference.

Segmenting involves placing the high- and low-temperature materials in the waste heat up- and down-stream respectively, allowing each material to operate in the desirable temperature difference [48]. Caillat et al. [49] demonstrated a segmented TED can achieve an efficiency of 15% over an operating temperature range of 300 to 973 K. Similarly, Crane et al. [50] modeled a segmented TEG with an efficiency of 10%.

In addition to studies on cascaded and segmented TEDs, numerical studies on conventional TEG performance applied to waste heat recovery applications have been conducted. Antonova et al. [51] used coupled-field analyses to analyze thermoelectric devices under transient and steady-state operations, taking into account Joule heating and the Peltier, Seebeck and Thomson effects, demonstrating the capabilities of commercial solvers. Kousksou et al. [52] studied the application of thermoelectric generators to helicopter conical nozzles and found the device performance to be extremely sensitive to fluid conditions and operating conditions. Gould et al. [53] studied low power generation of a thermoelectric unicouple using the Technology Computer Aided Design software package. Kumar et al. [54, 55] numerically modeled and parametrically evaluated the performance of conventional TEGs installed on plate-fin heat exchangers for automotive waste heat recovery applications. Their findings suggest that an overwhelming majority of waste heat can be converted into electrical energy with an achievable system efficiency of 5.5% and maximum power output of 553 W per flow conditions. Their findings stated the power output of the modules increases near-exponentially with an increase in inlet exhaust temperature and asymptotically approaches a limit with increasing flow rate due to limits on heat transfer coefficients [54]. Additionally, the authors found that parallel-flow heat exchanger configurations yielded the best performance due to a constant temperature difference across the TEG modules as opposed to conventional cascading designs, achieving a power output of 730 W [55].

More studies by Yu et al. [56] numerically investigated the effects of transients in the form of vehicle start-up and operation on the performance of TEGs, finding that start-up conditions do not significantly affect the time to reach steady-state power output. Sun et al. [57] modeled two-stage TEGs in serial and parallel configurations in comparison to a single-stage TEG for waste-heat recovery of internal combustion engines, finding that each system performs favorably under certain operating conditions, eluding the need for system

optimization per application. Reddy et al. [58] studied the performance of conventional TEGs applied to automotive waste heat recovery using a porous media approach. Hsiao et al. [59] mathematically modeled a thermoelectric generator using a one-dimensional thermal resistance network applied to automobile waste heat recovery and compared their results to those of experiments, finding better device performance when the thermoelectric generator was installed on the exhaust pipe as opposed to the radiator.

Experimental studies have also been conducted to analyze conventional TEG waste heat recovery applications. Jang et al. [60] experimentally investigated the incorporation of heat pipes into a system of TEGs to allow remote generation of electrical energy from automotive waste heat. Additionally, Liu et al. [61] investigated the implementation of a two-stage TEG in the exhaust system of an automobile with a system efficiency of 5.35% and power output of 250 W. Furthermore, conventional TEGs were applied to the exhaust system of a Humvee, allowing for the production of 944 W maximum at ideal operating conditions [62]. Waste heat recovery applications of segmented and cascaded TEDs have also been applied to automobiles. LaGrandeur [63] and Crane et al. [64] have demonstrated TEDs can recover exhaust gas waste heat, potentially producing enough electrical energy to aid and/or replace the secondary electro-mechanical alternator systems. The replacement of the alternator would reduce load on the engine, increasing efficiency. Crane et al. [65] developed a cylindrical TED comprised of segmented elements that produced a maximum power output of 608 W. They then implemented this TED concept into two passenger cars, converting exhaust gas heat into electrical power [66]. Furthermore, Da-Jeng Yao et al. [67] discussed using TEDs in the same application using a thermal resistance network model for automobile waste heat recovery at both the radiator and post-catalytic converter, finding more heat energy was available within the exhaust gas. Additionally, K. T. Chau et al. [68] discussed using TEDs for both waste heat recovery and temperature control modules for hybrid vehicles.

Applications of TEGs do not have to be limited to automotive applications; Luo et al. [69] numerically studied the implementation of TEGs on a cement rotary kiln, stating that such a system could recover nearly 1/3 of wasted thermal energy, yielding 211 kW of electrical power and 3.3 MW of energy savings. Ma et al. [70] studied the application

of TEGs to a biomass gasifier, providing the ability to generate 6 W of electrical power from an otherwise wasted source of thermal energy. Xiong et al. [71] numerically modeled the performance of a two-stage TEG applied to the coolant water of blast furnace slag, yielding 440 W of power output for mild operating temperatures. TEDs have also been applied to hybrid photovoltaic (PV) systems [72, 73, 74] and for hybridized PV-TE systems for improved conversion efficiency [75, 76]. It has been estimated the hybrid systems could achieve nearly 23% conversion efficiency [77].

There is an overarching theme that the application of conventional, including cascaded and segmented, TEGs to waste heat recovery has tremendous, widespread potential to increase system efficiency, reduce green-house gas emissions and make processes more cost effective. To that end, there is also a flaw with the application of conventional TEGs for said applications. Conventional TEGs have a large thermal resistance associated with the ceramic support structures and adhesives [78, 79] and subsequent stress induced by various coefficients of thermal expansion within the TEG, especially at large temperature differences [80]. Effort has been made by Hu et al. [81] to study the use of gas-phase heat exchangers on a thermoelectric generator to enhance heat transfer and fluid flow for improved device performance while reducing thermal stresses.

Previous work has been conducted on an integrated thermoelectric device to reduce the thermal resistance between source and sink. The integrated thermoelectric device incorporates the hot-side heat exchanger directly into the hot-side interconnector, removing the hot-side ceramic and associated adhesives that would typically affix the said heat exchanger to ceramic and ceramic to interconnector, as seen in Fig. 1c. The integrated thermoelectric device still functions electrically in series and thermally in parallel, but has a reduced thermal resistance between source and sink, allowing for a greater temperature difference to be imposed across the thermoelectric materials for given flow conditions as compared to a conventional TEG.

The integrated thermoelectric device arose from the concept of a composite thermoelectric device; a composite thermoelectric device replaces a portion the the thermoelectric material with a high electrically and thermally conductive material. The premise of this restructuring is to keep the height of the thermoelectric elements constant within a gen-

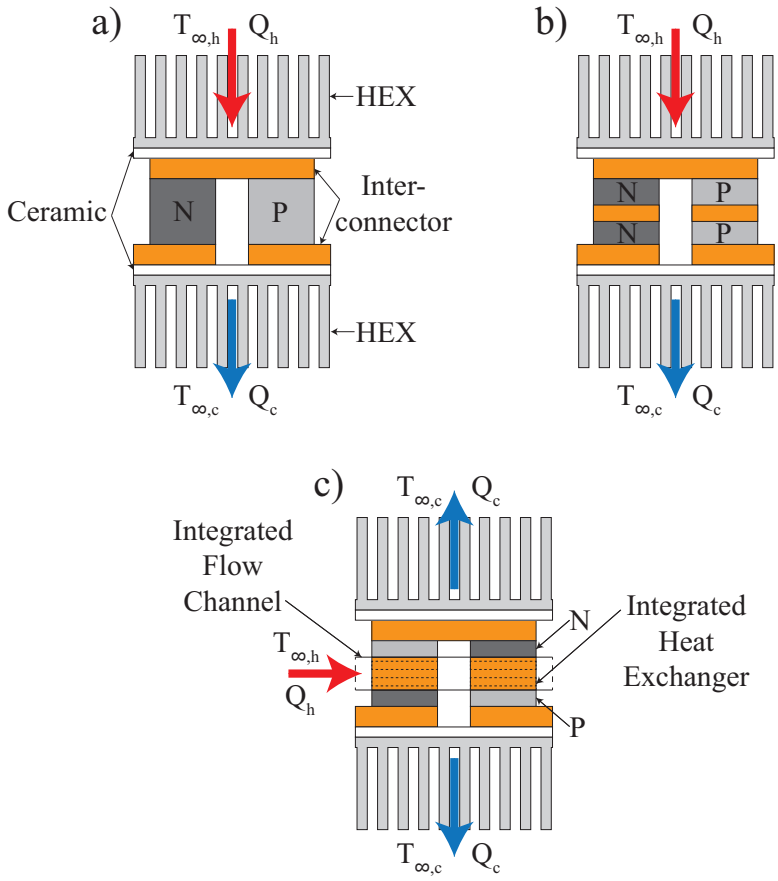

Figure 1: Illustrative representation of a a) conventional, b) composite and c) integrated thermoelectric device, without associated load resistance circuitry. The variables $T_{\infty,h}$, $T_{\infty,c}$ Q_h, Q_c, HEX, N and P refer to the hot-side fluid temperature, cold-side fluid temperature, heat input, heat output, heat exchanger, n-type and p-type, respectively.

erator that experience a large temperature difference between source and sink in terms of hot-side fluid temperature as heat is removed from the waste heat source. Reddy et al. [82] mathematically and numerically modeled the performance of conventional and composite thermoelectric devices applied to waste heat recovery applications assuming a constant hot-side temperature. Their studies showed an increase in thermal conversion efficiency and power output for a composite thermoelectric device in comparison to a conventional device due to a decrease in internal resistance and increase in heat input; this is based upon the assumption that the temperature difference across the thermoelectric device could be maintained. To more realistically model the performance of a composite thermoelectric device, Reddy et al. [83] analytically modeled their performance in comparison to conventional thermoelectric devices taking into account thermal and electrical contact resistances between the intermediate material and cold- and hot-side convective heat transfer coefficients. Their study showed that when analyzing the composite thermoelectric device using convective heat transfer coefficients and taking into account thermal and electrical contact resistances, the performance is often worse than that of a conventional thermoelectric device.

The studies of composite thermoelectric devices were then extrapolated to integrated thermoelectric devices. The hot-side heat exchanger, which is typically affixed to a ceramic plate in contact with the hot-side interconnector, is incorporated into the intermediate interconnecting material of the composite thermoelectric device. Chyu et al. [84] numerically studied composite and integrated thermoelectric devices and the effects of hot surface temperature, thermoelectric element thickness and hot fluid flow rate on power output, thermal conversion efficiency and pressure drop. Their findings indicated that an increase in inlet fluid flow rate up to a Reynolds number of 500 for a fixed inlet temperature of 550 K increased the hot-side junction temperature of the integrated thermoelectric device, resulting in a greater temperature difference across the thermoelectric device for a fixed cold-side temperature, resulting in a greater power output in comparison to a conventional thermoelectric device operated under the same conditions.

Additionally, Reddy et al. [85] analytically modeled composite and integrated thermoelectric devices in comparison to conventional device designs and found the integrated thermoelectric device outperformed the composite and conventional, in terms of power out-

put, nearly eight-fold, due to an increased temperature difference across the p-n junctions. The increase in temperature difference was due to a decrease in thermal resistance between source and sink. The thermal conversion efficiency was dependent upon the hot-side convective heat transfer coefficient which is directly proportional to the flow rate as expressed by the Reynolds number. The integrated thermoelectric device, even though exhibiting an increase in power output, displayed a decrease in thermal conversion efficiency with an increase in flow rate in comparison to the conventional design due to the increased pumping power requirement to move the fluid through the integrated flow channel and heat exchanger.

The integrated thermoelectric device was then numerically studied by Reddy et al. [86]. The effect of fluid inlet temperature and flow rate were investigated for a fixed heat exchanger and thermoelectric material geometry. For low-flow rate conditions, i.e. Reynolds number less than 500, it was found increasing inlet fluid temperature increased power output, heat input and thermal conversion efficiency. Increasing the inlet fluid flow rate increased the hot-side convective heat transfer coefficient and thus heat input and power output of the integrated device, however not as drastically as an increase in fluid inlet temperature. These studies were continued through numerical investigation by Reddy et al. [87] to include the effect of thermoelectric element height on the performance on an integrated thermoelectric device. For given operating conditions, there exists an optimal thermoelectric element height that provides a maximum power out and thermal conversion efficiency.

The effects of integrated heat exchanger geometry, flow rate and hot-fluid temperature were studied numerically by Reddy et al. [88]. Three integrated heat exchanger geometries were proposed, and it was found that increasing the surface area increased the power output, thermal conversion efficiency and pressure drop for a given flow rate and fluid temperature. These studies were limited to laminar flow rates with Reynolds numbers varying between 100 and 500, not accurately reflecting real waste heat recovery application flow conditions.

Studies were then conducted on a multistage integrated thermoelectric device. Reddy et al. [89] investigated the effect of inlet fluid temperature and flow rate, thermoelectric element height and number of integrated thermoelectric stages on the device performance. As seen in previous work, there existed an optimum thermoelectric element height for given flow conditions that yielded maximum power output and thermal conversion efficiency. Increasing

fluid inlet temperature and flow rate had substantial effects on single and multistage device performance. The power output and efficiency both increase nonlinearly with an increase of flow rate, whereas efficiency increases linearly and power output quadratically with an increase in inlet fluid temperature. Increasing the number of stages increases the heat input, however the heat input per subsequent stage is decreased due to the decreased thermal energy available. The power output logarithmically increases whereas the efficiency exponentially decreases with number of modules; the efficiency is influenced by the linear increase of pressure drop with increse in number of modules.

As described within the aforementioned section, there exists a need to design, analyze and optimize conventional TEDs to increase their performance characteristics under prescribed operating conditions. Additionally, components that contribute to decreased device performance have been identified (hot-side ceramic and associated greases) but not quantified, and novel device design concepts built upon the removal of these restrictive components have been studied analytically and numerically, but not experimentally. As will be discussed in Sec. 1.4, these key concepts will serve as a basis of motivation for the work presented within this dissertation. Furthermore, as will be developed in the following section, TED performance is not limited to design and construction, but dependent on thermoelectric material properties; the thermal conversion efficiency of the device is limited by the thermal conversion efficiency of the material. To further increase device thermal conversion efficiency, higher-performance thermoelectric materials must be developed.

1.3 MATERIAL PERFORMANCE

The following section will describe methodologies employed to increase the figure of merit ZT of bismuth-telluride and alloys thereof. This summary will provide context for the studies described in Chap. 6.

Since the advent of moderate performance thermoelectric semiconductors, in particular bismuth-telluride (Bi_2Te_3), methods to fabricate bulk Bi_2Te_3 compounds with a high figure of merit have been pursued. Growth of single-crystals [90, 91, 92], cold isostatic pressing (CIP)

followed by annealing [93, 94, 95], mechanical alloying (MA) following by CIP and annealing [96, 97, 98, 99, 100, 101], hot isostatic pressing (HIP) [102, 103, 104, 105, 106] followed with mechanical alloying [107, 108, 109], cryogenic MA [110], spark plasma sintering (SPS) as compared to HIP [111, 112, 113] and rapid solidification [114] followed by HIP [115, 116, 117] have all been pursued. For high-grade applications, lead-tellurides [118, 119] and clathrates [120] are used; the methods for increasing these materials' efficiency are the same as Bi_2Te_3.

These aforementioned methods have tried to capitalize on the intrinsic anisotropy of the electrical and thermal conductivities by controlling grain orientation and size. The structure of Bi_2Te_3 belongs to the D_{3d}^5 $R\bar{3}m$ group and exhibits a rhombohedral structure, with atomic layers of $Te^{(1)}$-Bi-$Te^{(2)}$-Bi-$Te^{(1)}$ covalently bonded, stacking in the direction perpendicular to the basal plane (c-axis). The intermolecular bond between $Te^{(1)}$-$Te^{(1)}$ is a van der Waals bond, which exists perpendicular to the c-axis [121]. Manipulating grain orientation and size allows for an increases in ZT. For example, comparing intrinsic material properties measured perpendicular and parallel to the basal plane for single-crystal samples, the thermal conductivity ($\kappa_\perp/\kappa_{||}$) increases by a factor of 2.1 [90] to 2.3 [122]. The electrical conductivity ($\sigma_\perp/\sigma_{||}$) increases by a factor of 2.6 to 3.0 [122]. The Seebeck coefficient ($\alpha_\perp/\alpha_{||}$), although assumed to be isotropic, increases by a factor of 1.1 [123, 122]. These anisotropic effects leads to an approximate 1.5- to 1.6-fold increase in ZT if proper crystal orientation is developed.

Decoupling thermal conductivity and electrical resistivity are somewhat difficult, placing a limit on the potential gain in performance due to anisotropic properties. For instance, the electronic contribution to the thermal conductivity κ_{el} (κ=κ_{el}+κ_{ph}) is proportional to the electrical conductivity such that κ_{el}=σTL [124] where L is the Lorenz factor [125]. Reducing the phononic contribution to thermal conductivity via phonon scattering at grain boundaries would yield an increase in performance. However, if the electronic contribution to thermal conductivity was reduced from non-coherent grain boundaries, the electrical resistivity would increase, potentially diminishing performance.

Of these stated methods, CIP followed by annealing offers a marked increase in ZT in bulk Bi_2Te_3-based alloys without the need for energy-intensive procedures. During compaction, Bi_2Te_3 particles cleave at the van der Waals bonds (i.e. the Te^1-Te^1 bonds perpendicular to the c-axis). Thus, a sample is able to have the majority of the particles with

preferred orientation of the c-axis parallel to the pressing direction if the operational parameters (powder size, compaction pressure, sintering temperature and time) are controlled. Of the CIP experiments conducted, there has been a variety of preparation conditions studied, with varying results. For simplicity, a few references are described in detail.

Navrátil et al. [93] used a compaction pressure of 1,200 MPa and an annealing time and temperature of one hour and 800 K, respectively, on 130-300 and $\leq$ 130 μm particle $Sb_{2-x}Bi_xTe_3$ ($0.43 \leq x \leq 0.51$). They found a ZT of 0.936 at 300 K irrespective of the particle size and concluded smaller particle sizes increase the electrical resistivity. Liao et al. [95] CIP and sintered $Bi_{0.5}Sb_{1.5}Te_3$ at 600 MPa and 463-473 K for 10-60 minutes. The authors found ZT values for pressed, 10-minute and 60-minute sintered samples of 0.14, 0.13 and 0.24 measured at 300 K. Performance was attributed to a balance of defect elimination and grain growth via sintering, and an increase in carrier density and mobility with increased sintering time.

O. Ben-Yehuda [94] achieved a ZT of 0.9 at 300 K for 100-175 μm $Bi_{0.4}Sb_{1.6}Te_3$ powder using a compaction pressure of 800 MPa and sintering conditions of 643 K for 24 hr. They found this method yielded a Lotgering factor, as will be introduced in Results and Discussion of Chap. 6 , of 0.75$\pm$0.03, which is attributed to increasing ZT. The high Lotgering factor is a result of the texture-inducing powder metallurgy technique used. Yu et al. [97] used a compaction pressure of 960 MPa and sintered the Bi_2Te_3 samples at 473-773 K for 3 hours. The authors found a ZT of 0.94 at 398 K and attributed the increase to high electrical conductivity and low thermal conductivity. These properties were the byproduct of small (30 nm), coherent grains. The coherent grains formed during the release of strain energy, which was imparted during compaction.

Lu et al. [101] compacted $\leq$2 μm $Bi_2(Se,Te)_3$ at 600 MPa which was subsequently sintered at 523-623 K for two hours. ZT measured at 300 K yielded values between 0.22 and 0.3. Similarly, the authors stated sintering eliminates crystal defects and microstrain generated during compaction and leads to the growth of crystal grains. A.A. Joraide [96] prepared 25% Bi_2Te_3-75% Sb_2Te_3 samples with fine grain sizes as prepared by MA, ranging from 30 to $\leq$5 μm. The powders were compacted at a pressure of 770 MPa and sintered the samples at 673 K for 6 hours. It was found samples prepared with a sintering temperature of

680 K were isotropic, whereas above 680 K the samples exhibited anisotropy. As the grain size increased, α, κ and Z increased and ρ decreased; evaluated at 300 K, ZT decreased from 2.28, 1.47, 1.23, 1.11 to 0.264 for grain-sized powders of 30-20, 20-15, 15-10, 10-5 and $\leq$5 μm, respectively. Although the materials within this experiment are different from those used by Lu et al. [101], the performance of the n- and p-type materials are comparable within this temperature range, and the smallest grain size results are in agreement.

It is evident from literature on CIP and sintering experiments that developing a highly-oriented, anisotropic bulk material with coarse grains should yield a material with low thermal conductivity and electrical resistivity, yielding a large ZT. Contrarily, it was also found through MA, HIP and SPS experiments that small, coherent grains, either uniformly or non-uniformly distributed through the material matrix, act as nanostructures which are able to reduce κ_{ph} without adversely affecting σ, thus increasing ZT [97, 100]; these effects are elaborated upon in great detail [126]. The effect of precursor particle size, compaction pressure, sintering, as well as annealing, time and temperature on the texture and performance of Bi_2Te_3 materials as prepared by CIP and sintering remain unclear. This lack of clarity on processing parameters, texture and subsequent material performance is the motivation for a part of this dissertation, as elaborated upon in the following section.

1.4 MOTIVATION

Reviewing the literature on conventional thermoelectric device design and thermoelectric material processing, it is evident deficiencies exists in the employed methodologies and means for potential improvement are present. In terms of device design and analysis, analytical optimization modeling techniques often neglect the inter-dependence of thermoelectric material cross-sectional area and leg length on performance and often focus on one aspect, for instance, optimization of leg shape or length while holding the cross-sectional areas equal and invariant. Also, analytical thermal resistance models often exclude important components such as thermal resistances associated with adhesives between heat sinks and ceramics, independent thermal and electrical contact resistances associated with the bonding of ther-

moelectric materials to the interconnectors, and properly resolving radiative and convective heat transfer within the thermoelectric device cavity. These deficiencies are presented in detail in Chap. 2 Sec. 2.1.

It is therefore essential to develop new geometric optimization techniques and more comprehensive thermal resistance networks to properly optimize thermoelectric material geometry and model heat transfer characteristics. In this dissertation, we will focus on the development of a co-optimization technique that simultaneously optimizes the leg length and cross-sectional area of a given thermoelectric material (e.g. p-type) in reference to an invariant geometry (e.g. n-type) based upon the realized temperature difference and thermal and electrical contact resistances present at the material interfaces resolved from a complete thermal resistance network. The co-optimization methodology will be employed for improved thermal conversion efficiency and power output of a thermoelectric unicouple evaluated within the thermal resistance network. The co-optimization technique is done through the derivation of an expression of the denominator of eqn. 1.1 that takes into account geometrical parameters and independent thermal and electrical contact resistances.

Additionally in terms of device design and analysis, it is known the ceramic support structures and associated adhesives between interconenctors and heat exchangers impose a large thermal resistance between the heat source and sink. This thermal resistance reduces the temperature difference imposed across the p-n junction, thereby reducing thermal conversion efficiency and power output. Although the integrated thermoelectric device has been proposed analytically [85] and numerically [84, 86, 87, 88, 89] at low Reynolds number conditions, extending this concept into an experimental study encompassing Reynolds numbers typically found within waste-heat recovery applications has not been conducted. In this dissertation, we will focus on the performance of integrated thermoelectric devices under a range of operating conditions that reflect realistic waste-heat recovery conditions to demonstrate concept viability and improvements in performance in comparison to conventional thermoelectric device designs.

In terms of material processing, the deficiency of not having consistent trends in thermoelectric properties with processing parameters and material characteristics, such as grain size and size distrubutions, orientation and coherency, provides an area of potential improvement.

As elaborated upon in Sec. 1.3, variation in precursor particle size compaction pressure, sintering temperature and time drastically effect the texture and subsequent performance of the thermoelectric material. In this dissertation, we will focus on the effects of compaction pressure and sintering temperature and time on the crystallographic texture and subsequent thermoelectric properties of bulk bismuth telluride.

1.5 OBJECTIVES

Given the areas of potential improvement related to thermoelectric device design and thermoelectric material processing in Sec. 1.4, this work focuses on various methods to improve the stated deficiencies. In particular, this work focuses on improving the thermal conversion efficiency and power output of thermoelectric devices and materials through the implementation of analytical models, novel device designs and material processing. The specific objectives of this work are:

1. To develop a geometric co-optimization technique that simultaneously optimizes the cross-sectional areas and lengths of the thermoelectric elements to maximize thermal conversion efficiency and power output based upon a.) the experienced temperature difference across the p-n junctions as determined by a complete one-dimensional thermal resistance network b.) that incorporates independent thermal and electrical contact resistances. The model will be analyzed to determine areas of design improvement in terms of thermal resistance between heat source and sink;
2. To develop a numerical scheme to resolve the three-dimensional radiation view factors between the hot- and cold-side ceramic plates within a unit-cell thermoelectric device cavity taking into account a.) the shadow effect produced by interconnector and thermoelectric material geometry, b.) various packing density configurations and c.) various height-to-width ratios of thermoelectric elements and heights of interconnectors, as to aid in the development of Item 1;
3. To extend the determination of areas of improvement per Item 1 to experimentally determine the performance characteristics of novel a.) single-stage and b.) multi-stage pin-fin

thermoelectric devices under operating conditions reflecting realistic waste-heat recovery applications (i.e. high Reynolds numbers);

4. To determine the effect of a.) compaction pressure, b.) sintering time and c.) temperature on the texture, in terms of crystallography and grain size distributions, and thermoelectric performance, in terms of Seebeck coefficient, thermal conductivity and electrical conductivity, expressed independently and in terms of the figure of merit, of bulk bismuth telluride.

1.6 ORGANIZATION

Since this dissertation presents a mulitfaceted approach to thermoelectric device and material improvement in performance, it is organized into three parts, each representing one component of the multifaceted approach to increase device performance. Part I, which consists of Chaps. 2 and 3 and Appendix B, presents the analytical framework for the one-dimensional thermal resistance network and geometric optimization algorithm, and numerical methodology for resolving three-dimensional radiation view factors within a thermoelectric device cavity, respectively. Part II, which consists of Chaps. 4 and 5, presents the experimental studies on single-stage and multi-stage pin-fin integrated thermoelectric devices and their performance characteristics, respectively. Part III, which consists of Chap. 6, presents the experimental methods of uniaxial compression and sintering parameters and subsequent effect on material performance characterized by the figure of merit.

Chapter 2 provides an in-depth description of thermal resistance modeling related to thermoelectric devices coupled with the geometric optimization of thermoelectric geometry (cross-sectional area and leg length) algorithm developed within and the determination of system components that reduce device performance. The thermal resistance network is all-inclusive in that the thermal resistance of heat exchangers, interface materials, ceramic support structures, interconnectors and thermoelectric materials, as well as convective and radiative resistances within the cavity, are considered. The effect of operating conditions, in particular heat exchanger effective area, heat transfer coefficients and cold- and hot-fluid

temperatures, as well as thermal and electrical contact resistances are investigated. Chapter 3 is a component of Chap. 2 in that is resolves the radiation view factor between the two primary participating surfaces for a three-dimensional unit cell thermoelectric junction, providing more accurate predictions of conventional and optimized thermoelectric device performance as determined by analytical modeling. The presented work within this chapter details the effect of packing density, thermoelectric element height and width and interconnector thickness on radiation view factors between hot and cold ceramic plates taking into account the shadow effect.

The results of Chaps. 2 and 3 preceded the introduction and development of the novel integrated thermoelectric device. Chapter 4 introduces the single-stage integrated thermoelectric device and presents the performance characteristics (produced voltage and current and subsequently calculated thermal conversion efficiency and power output) for various inlet fluid temperature and flow rates and load resistances, providing a basis of comparison between conventional and integrated thermoelectric devices. Chapter 5 presents the multi-stage pin-fin integrated thermoelectric device, an extension of the single-stage integrated thermoelectric device, and the effect of operating conditions on device performance.

Departing from device modeling, analysis and design which reflect device performance, Chap. 6 presents the methods of material processing of bulk bismuth telluride (Bi_2Te_3) for improving material efficiency. The presented parametric study quantifies the effects of compaction pressure and annealing time and temperature on the texture of bulk Bi_2Te_3. The texture, as analyzed via diffractograms and quantified by the Lotgering factor, indicates the degree of preferred orientation. Samples with the and highest degree of preferred orientation were then annealed at various temperatures and characterized in terms of thermoelectric performance (Seebeck coefficient, thermal conductivity, electrical resistivity and figure of merit). Within Chap. 7, the work presented within this dissertation is summarized highlighting primary contributions, conclusions are provided and future work is discussed.

It is noted each chapter has a suborganizational scheme. Any introductory information not provided in Chap. 1 that is necessary for the subsequently presented material is briefly introduced. If the chapter is analytical or numerical in nature, a section on the mathematics and methodology is introduced. If the chapter is experimental in nature, sections on materials

and methods are introduced. These introductory sections are proceeded by an in-depth results and discussion, followed by brief concluding marks within a separate conclusion.

2.0 ANALYTICAL STUDIES ON THE GEOMETRIC OPTIMIZATION OF CONVENTIONAL THERMOELECTRIC DEVICES

2.1 INTRODUCTION

The development of an analytical one-dimensional thermal resistance network model with the inclusion of geometric optimization of the thermoelectric material geometry is preluded by a review of specific works that to a degree attempted a similar goal.

Within the TED, heat sink [127, 128] and leg geometry optimization [129, 130, 131] have been pursued, and internal and external resistances have been minimized [127, 132]. Min and Rowe [133] evaluated the performance of TEDs in terms of power output for waste heat recovery applications taking into account the electrical and thermal contact resistances and TE element leg height, but did not optimize the cross-sectional areas to maximize either power output or thermal conversion efficiency. Freunek et al. [134] proposed an analytical model to optimize the geometry of a TED, taking into account the Peltier effect and Joule heat, Thomson effect, thermal and electrical contact resistances, source and sink conditions and load resistance. The model was oversimplified to assume the cross-sectional areas of the n- and p-type TE materials were the same and therefore only the TE material length was optimized. Liang et al. [45] used a parallel resistance network to analyze the performance of a TEG taking into account thermal and electrical contact resistances, but did not pursue optimization. Recently, Yazawa and Shakouri [132] studied cost-effective waste-heat recovery of TEDs by considering the co-optimization of TE leg shape, heat sink, load and contact resistances, and heat losses. Sahin and Yilabs [131] evaluated the efficiency and power output of a TED in terms of the shape parameter of the legs. Although the effect of cross-sectional area as a function of leg height was considered, optimizing the individual leg cross-sectional

areas and the effect of contact resistances were not included. Jang et al. [135] optimized the leg height and cross-sectional area of the thermoelectric material and substrate thickness to maximize the power output of micro-thermoelectric generators.

Reviewing the literature, it is evident there is a deficiency in analyzing and optimizing the TE element geometry in terms of length and cross-sectional area taking into account independent thermal and electrical contact resistances and the the cold- and hot-side convective conditions. Therefore, this chapter addresses the co-optimization of TE geometry and studies the effects if cold- and hot-side heat exchanger area and heat transfer coefficients using a one-dimensional thermal resistance network. The cross-sectional area and length of the p-type bismuth-telluride material are optimized based upon the geometry of the n-type and the temperature difference imposed across the device, as determined by the resolution of a one-dimensional thermal resistance network.

2.2 MATHEMATICS

2.2.1 Cross-sectional area optimization assuming constant length

The figure of merit $Z\bar{T}$ (eqn. 1.1) is expressed as the ratio of the square of the sum of the absolute value of the Seebeck coefficients for the n- and p-type TE materials, α_N and α_P respectively, over the product of the the electrical resistance and thermal conductance of the n- and p-type materials $R_{el}K$, times the average temperature $\bar{T}$ [48]. This is expressed as

$$Z\bar{T} = \frac{(|\alpha_N| + |\alpha_P|)^2}{R_{el}K}\bar{T}. \tag{2.1}$$

The electrical resistance R_{el} (Ω) is expressed as the summation of the electrical resistances of the n- and p-type materials $R_{el,N}$ and $R_{el,P}$. The electrical resistances are a function of the material electrical resistances, ρ_N or ρ_P (Ωm,) times the length of the n- or p-type pellet, L_N or L_P (m) over the cross-sectional area of the n- or p-type pellet, A_N or A_P (m^2), respectively. This is expressed as

$$R_{el,N,P} = \frac{\rho_{N,P}L_{N,P}}{A_{N,P}}. \tag{2.2}$$

Similarly, the thermal conductance K (WK^{-1}) is the summation of the thermal conductance of the n- and p-type materials K_N and K_P. The thermal conductance is the thermal conductivity λ ($Wm^{-1}K^{-1}$) of the respective material times the cross-sectional area over the length such that

$$K_{N,P} = \frac{\lambda_{N,P}A_{N,P}}{L_{N,P}}. \tag{2.3}$$

Additionally, the ratio of the cross-sectional area to length of material can be expressed as γ (m), such that

$$\gamma_{N,P} = \frac{A_{N,P}}{L_{N,P}}. \tag{2.4}$$

For most thermoelectric device applications, the length of the n- and p-type materials are the same and the length can be simply expressed as $L{=}L_N{=}L_P$. An illustrative schematic is

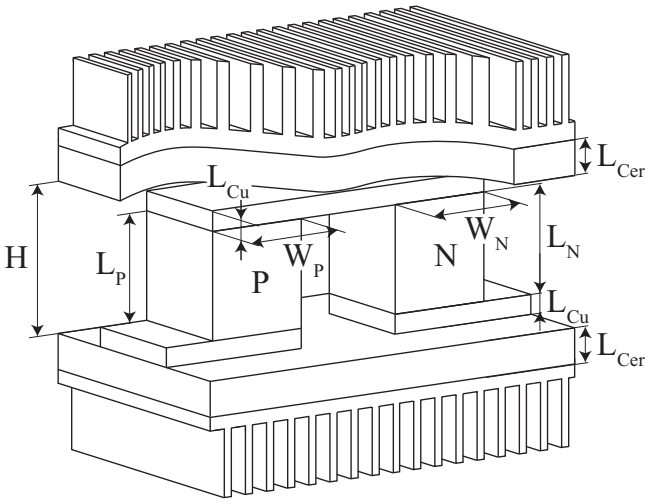

Figure 2: Schematic of thermoelectric generator.

provided (Fig. 2), which shows a thermoelectric module including the heat sinks. Following the optimization of the cross-sectional area of the TE pellets assuming equal leg heights, the geometry of the TE pellet will be optimized assuming $L_N \neq L_P$. During TED fabrication, the n- and p-type materials are attached to the interconnectors by methods of soldering, brazing, epoxying or diffusion bonding; the interface material is represented by Π. The aforementioned methods of attachment introduce thermal and electrical contact resistances which diminish device performance. The electrical contact resistance $R_{el,c}$ is similar to the electrical resistance of the TE material such that

$$R_{el,c} = \frac{\rho_c L_c}{A_c} \tag{2.5}$$

where ρ_c is the electrical resistivity (Ωm), L_c is the thickness and A_c is the cross-sectional area of the bonding material Π. For the case of the n-type pellet, A_c=A_N and for the p-type pellet, A_c=A_P. Typically, $L_c \ll L$, i.e. on the order of nanometers to microns depending on bonding material and method. Expressing the electrical contact resistance including the minuscule thickness of the contact resistance L_c, the modified electrical resistance of the contact is ρ_{c^+}=$\rho_c L_c$ (Ωm^2) yielding $R_{el,c}$=ρ_{c^+}/A_c, which is per surface area per pellet. By

multiplying $R_{el,N}$ and $R_{el,P}$ by L_N/L_N and L_P/L_P,respectively, and using the identity of γ (eqn. 2.4), the electrical resistance of the contacts of a single p-n junction can be stated as

$$R_{el,c} = 2\left(\frac{\rho_{c,N^+}}{\gamma_N L_N} + \frac{\rho_{c,P^+}}{\gamma_P L_P}\right). \tag{2.6}$$

Additionally, the total thermal contact conductance K_c is expressed as the summation of the thermal conductances of Π between the surfaces of the n- and p-type pellets and interconnectors. The thermal contact conductance on the surface of a TE pellet is expressed as

$$K_c = \frac{\lambda_c A_c}{L_c} \tag{2.7}$$

where λ_c is the thermal conductivity ($\mathrm{Wm^{-1}K^{-1}}$), A_c is the cross-sectional area and L_c is the thickness of the interface material. It is evident A_c=A_N and A_c=A_P for the n- and p-type pellets respectively. When $L_c \ll L$, the thermal conductivity of the interface material can be expressed as λ_{c^+}=λ_c/L_c, ($\mathrm{Wm^{-2}K^{-1}}$), which includes the thickness. Multiplying K_N and K_P by L_N/L_N and L_P/L_P, respectively, and using the identity of eqn. 2.4, the thermal contact conductance of a single p-n junction is expressed as

$$K_c = 2(\lambda_{c,N^+} L_N \gamma_N + \lambda_{c,P^+} L_P \gamma_P). \tag{2.8}$$

The $R_{el}K$ expression excluding and including the thermal conductivity and electrical resistivity of the contact material is expressed as

$$R_{el}K = \begin{cases} \left(\dfrac{\rho_P}{\gamma_P} + \dfrac{\rho_N}{\gamma_N}\right)(\lambda_P\gamma_P + \lambda_N\gamma_N) & \nexists\Pi \quad (2.9a) \\ \left(\dfrac{\rho_P}{\gamma_P} + \dfrac{\rho_N}{\gamma_N} + R_{el,c}\right)(\lambda_P\gamma_P + \lambda_N\gamma_N + K_c) & \exists\Pi\ . \quad (2.9b) \end{cases}$$

The electrical resistance and thermal conductance (R_{el} (Ω) and K ($\mathrm{WK^{-1}}$), respectively), are expressed as functions of the surface area of the p- and n-type materials in terms of γ_N/γ_P.

By minimizing the $R_{el}K$ product (eqn. 2.1) with respect to γ_N/γ_P (eqn. 2.9a and 2.9b), Z is maximized and we are left with the following expressions

$$\left(\frac{\gamma_N}{\gamma_P}\right)_{\eta_{th,max}} \begin{cases} \left(\dfrac{\rho_N\lambda_P}{\rho_P\lambda_N}\right)^{\frac{1}{2}} & \nexists\Pi \qquad (2.10a) \\ \left(\dfrac{\frac{\lambda_P\rho_N}{2}+\frac{\lambda_P\rho_{c,N^+}}{L}+\lambda_{c,P^+}\rho_N L+2\lambda_{c,P^+}\rho_{c,N^+}}{\frac{\lambda_N\rho_P}{2}+\frac{\lambda_N\rho_{c,P^+}}{L}+\lambda_{c,N^+}\rho_P L+2\lambda_{c,N^+}\rho_{c,P^+}}\right)^{\frac{1}{2}} & \exists\Pi\ . \qquad (2.10b) \end{cases}$$

It is evident excluding the interface material (i.e. the thermal conductivity and electrical resistance are neglected), the minimized product of Eqn. 2.10b reduces to that of Angrist (eqn. 2.10a) [136]. Substituting eqn. 2.10a or 2.10b into the original expression for the $R_{el}K$ product in eqn. 2.1, we then have the minimized $R_{el}K$ product $(R_{el}K)_{min}$.

The maximum value of the figure of merit Z_{max} is expressed by using the $(R_{el}K)_{min}$ product such that

$$Z_{max} = \frac{(|\alpha_N| + |\alpha_P|)^2}{(R_{el}K)_{min}}. \qquad (2.11)$$

The thermal efficiency of a thermoelectric generator can now be expressed in terms of the maximum figure of merit such that

$$\eta_{th} = \frac{m'(\frac{\Delta T}{T_h})}{\frac{(1+m')^2}{Z_{max}T_h} + (1+m') - \frac{\Delta T}{2T_h}} \qquad (2.12)$$

where m' is the ratio of the load resistance to internal resistance expressed as

$$m' = \frac{R_L}{R_{el}}. \qquad (2.13)$$

By taking a value of m' that maximizes the thermal efficiency, the derivative of eqn. 2.12 is taken with respect to m' such that

$$m'_{opt} = (1 + Z_{max}T_{avg})^{\frac{1}{2}}. \qquad (2.14)$$

Using this optimized ratio of load to internal resistances, the maximum thermal efficiency $\eta_{th,max}$ and maximum power output $P_{o,max}$ are expressed as

$$\eta_{th,max} = \frac{(m'_{opt} - 1)(\frac{\Delta T}{T_h})}{m'_{opt} + \frac{T_c}{T_h}} \tag{2.15}$$

and

$$P_{o,max} = \frac{(\alpha \Delta T)^2 m'}{(1 + m')^2 R_{el}}. \tag{2.16}$$

It is evident that $P_{o,max}$ occurs when $R_L = R_{el}$ such that

$$P_{o,max} = \frac{(\alpha \Delta T)^2}{4R_{el}} \tag{2.17}$$

The ratio of γ_N/γ_P that maximizes the power output can be determined by dividing $P_{o,max}$ by the total area (summation of n- and p-type cross-sectional areas) and then differentiating with respect to A_N/A_P such that

$$\frac{P_{o,max}}{(A_N + A_P)} = \frac{(\alpha \Delta T)^2}{4R_{el}(A_N + A_P)}. \tag{2.18}$$

The result of differentiating eqn. 2.18 with respect to the $R_{ek}K$ product (eqn. 2.9a and 2.9b) yields

$$\left(\frac{\gamma_N}{\gamma_P}\right)_{P_{o,max}} = \begin{cases} \left(\dfrac{\rho_N}{\rho_P}\right)^{\frac{1}{2}} & \nexists \Pi \qquad (2.19a) \\ \left(\dfrac{\rho_N L_N + 2\rho_{c,N^+}}{\rho_P L_P + 2\rho_{c,P^+}}\right)^{\frac{1}{2}} & \exists \Pi \ . \qquad (2.19b) \end{cases}$$

By imposing a value of either A_N or A_P and using Eqn. 2.19a or 2.19b, $P_{o,max}$ can be evaluated based upon optimum ratio of cross-sectional areas.

2.2.2 Cross-sectional area optimization assuming non-constant length

When the length of the n- and p-type elements are not the same, multivariable optimization can be employed to maximize the power out and thermal efficiency. Recalling the expression for the $R_{el}K$ product (eqn. 2.9a and 2.9b), but including the length of the n- and p-type elements as well as the cross-sectional areas, the modified $(R_{el}K)'$ product is expressed as

$$(R_{el}K)' = \begin{cases} \left(\frac{A_N}{A_P}\right)\left(\frac{L_P}{L_N}\lambda_N\rho_P\right) + \left(\frac{A_P}{A_N}\right)\left(\frac{L_N}{L_P}\lambda_P\rho_N\right) + remainder & \nexists\Pi \quad (2.20a) \\ \left(\frac{A_N}{A_P}\right)\left[4\lambda_{c,N}\rho_{c,P} + 2\lambda_{c,N}L_P\rho_P + \frac{2\lambda_N\rho_{c,P}}{L_N} + \left(\frac{L_P}{L_N}\right)\lambda_N\rho_P\right] + \\ \left(\frac{A_P}{A_N}\right)\left[4\lambda_{c,P}\rho_{c,N} + 2\lambda_{c,P}L_N\rho_N + \frac{2\lambda_P\rho_{c,N}}{L_P} + \left(\frac{L_N}{L_P}\right)\lambda_P\rho_N\right] + \\ remainder. & \exists\Pi \quad (2.20b) \end{cases}$$

Taking the derivative of $(R_{el}K)'$ (eqn. 2.20a and 2.20b) with respect to A_N/A_P and L_N/L_P separately, setting said derivatives equal to zero and solving for A_N/A_P and L_N/L_P yields the products that minimizes the $(R_{el}K)'$. These values are expressed as:

$$\left(\frac{A_N}{A_P}\right)_{\eta_{th,max}} = \begin{cases} \left(\frac{\left(\frac{L_N}{L_P}\right)\lambda_P\rho_N}{\left(\frac{L_P}{L_N}\right)\lambda_N\rho_P}\right)^{\frac{1}{2}} & \nexists\Pi \quad (2.21a) \\ \left(\frac{\lambda_P\rho_N\left(\frac{L_N}{2L_P}\right) + \frac{\lambda_P\rho_{c,N^+}}{L_P} + \lambda_{c,P^+}\rho_N L_N + 2\lambda_{c,P^+}\rho_{c,N^+}}{\lambda_N\rho_P\left(\frac{L_P}{2L_N}\right) + \frac{\lambda_N\rho_{c,P^+}}{L_N} + \lambda_{c,N^+}\rho_P L_P + 2\lambda_{c,N^+}\rho_{c,P^+}}\right)^{\frac{1}{2}} & \exists\Pi \quad (2.21b) \end{cases}$$

and

$$\left(\frac{L_N}{L_P}\right)_{\eta_{th,max}} = \left(\frac{\lambda_N\rho_P\left(\frac{A_N}{A_P}\right)}{\lambda_P\rho_N\left(\frac{A_P}{A_N}\right)}\right)^{\frac{1}{2}}. \quad (2.22)$$

The expression for L_N/L_P is the same result for eqn. 2.20a and 2.20b. To resolve this system of equations, eqn. 2.22 can be inserted into eqn. 2.21a or 2.21b to solve for A_N/A_P and then this solution can be inserted into Eqn. 2.22 to solve for L_N/L_P. Using this iterative process, for a given temperature difference across the elements ΔT, with or without the inclusion of an interface material Π with electrical contact resistance ρ_{c,N^+,P^+} and thermal

contact conductivity λ_{c,N^+,P^+}, the optimized ratio of cross-sectional areas and lengths can be determined.

Furthermore, the original expression for maximizing the power output (eqn. 2.18) can be expressed in terms of γ_N and γ_P, as opposed to simply A_N and A_P, to allow the co-optimization of A_N/A_P and L_N/L_P. The solutions to the derivative of the denominator of the power output equation, as expressed in terms of γ_N and γ_P, set equal to zero, with respect to A_N/A_P and L_N/L_P individually are

$$\left(\frac{A_N}{A_P}\right)_{P_{o,max}} = \begin{cases} \left(\dfrac{\rho_N\left(\frac{L_N}{L_P}\right)}{\rho_P\left(\frac{L_P}{L_N}\right)}\right)^{\frac{1}{2}} & \nexists\Pi \qquad (2.23a) \\ \left(\dfrac{\rho_N\left(\frac{L_N}{L_P}\right) + \frac{2\rho_{c,N^+}}{L_P}}{\rho_P\left(\frac{L_P}{L_N}\right) + \frac{2\rho_{c,P^+}}{L_N}}\right)^{\frac{1}{2}} & \exists\Pi \qquad (2.23b) \end{cases}$$

and

$$\left(\frac{L_N}{L_P}\right)_{P_{o,max}} = \left(\frac{\rho_P\left(\frac{A_N}{A_P}\right)}{\rho_N\left(\frac{A_P}{A_N}\right)}\right)^{\frac{1}{2}}. \qquad (2.24)$$

The expression for L_N/L_P is the same for both cases. Just like the system of equations describing the maximized thermal conversion efficiency, eqn. 2.24 can be inserted into eqn. 2.23a and 2.23b to solve for A_N/A_P and this solution can then be inserted into eqn. 2.24 to solve for L_N/L_P.

2.2.3 Thermal resistance modeling

To build upon what has been proposed, it is necessary to optimize not only the geometry of the thermoelectric elements but to also determine the effect of the cold- and hot-side heat exchanger effective areas for given cold- and hot-side conditions (i.e. temperature and heat transfer coefficient). To achieve this goal, a complete one-dimensional thermal resistance network is introduced, as illustrated in Fig. 3.

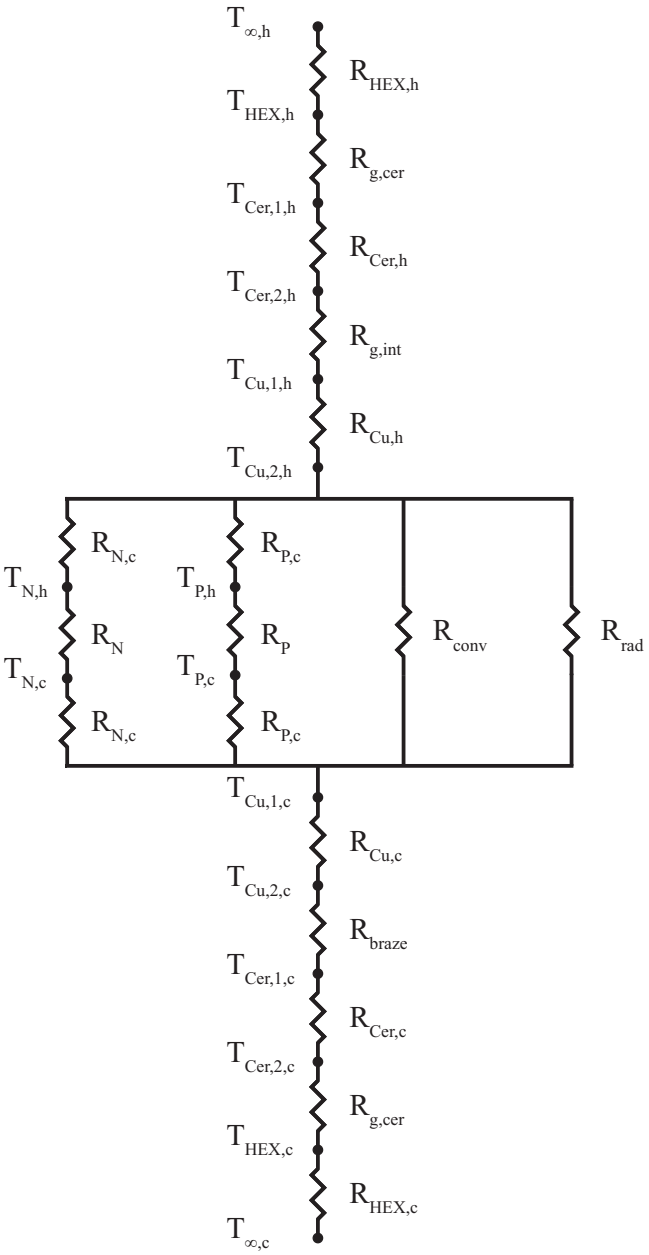

Figure 3: Thermal resistance network of a TEG.

The total thermal resistance is the summation of all the resistance components such that

$$R_{tot} = \sum_{i}^{N} R_i = R_{hex_{c,h}} + 2R_{g,cer} + R_{g,int} + R_{braze} + R_{cer_{c,h}} + R_{Cu_{c,h}} + \frac{\frac{(2 \cdot R_{N,c} + R_N) \cdot (2 \cdot R_{P,c} + R_P)}{(2 \cdot R_{N,c} + R_N) + (2 \cdot R_{P,c} + R_P)} \cdot \frac{R_{conv} \cdot R_{rad}}{R_{conv} + R_{rad}}}{\frac{(2 \cdot R_{N,c} + R_N) \cdot (2 \cdot R_{P,c} + R_P)}{(2 \cdot R_{N,c} + R_N) + (2 \cdot R_{P,c} + R_P)} + \frac{R_{conv} \cdot R_{rad}}{R_{conv} + R_{rad}}}. \tag{2.25}$$

The thermal resistance variables in order of appearances from the right hand side of the second equals sign of eqn. 2.25 are; the cold- and hot-side heat exchangers $R_{hex_{c,h}}$, the greases between the cold- and hot-side heat exchangers and respective cold- and hot-side ceramic plates $R_{g,cer}$ and the hot-side ceramic plate and hot-side interconnector $R_{g,int}$, the braze between the cold-side interconnector and cold-side ceramic plate R_{braze}, the cold- and hot-side ceramic plates $R_{cer_{c,h}}$, the cold- and hot-side copper interconnector $R_{Cu_{c,h}}$ and the parallel contribution of the n-type leg R_N, p-type leg R_P, the contact resistances associated with each leg ($R_{N,c}$ and $R_{P,c}$, respectively), and those associated with convection and radiation within the cavity (R_{conv} and R_{rad}, respectively).

The thermal resistance of a heat exchangers is expressed as unity divided by the convective heat transfer coefficient h times the effective area A_{eff}. In practical operations, the cold- and hot-side convective heat transfer coefficients seldomly equal, and the area of the cold- and hot-side heat exchangers differ as to ensure the proper temperature difference across the device. Therefore, the cold- and hot-side heat exchanger thermal resistances are independently expressed as

$$R_{hex_{c,h}} = \frac{1}{h_{c,h} A_{eff_{c,h}}}. \tag{2.26}$$

The cold- and hot-side convective heat transfer coefficients were varied between values of 1 and 500 $Wm^{-2}K^{-1}$ and 10^2 and 10^5 $Wm^{-2}K^{-1}$, respectively, to simulate typical free and forced convection values on cold-side heat exchanger and those imparted on the hot-side heat exchanger operating in high-flow waste heat recovery applications. The cold- and hot-side effective heat exchanger areas were varied between 0.1 cm^2 to 10 cm^2, respectively.

For construction of commonly available thermoelectric modules, the cold- and hot-side heat exchangers are affixed to the cold- and hot-side ceramics using a thermal grease, sheet or epoxy. The same grease is typically used to reduce the thermal contact resistance between the free-floating hot-side ceramic and hot-side interconnector. The thermal conductivity (λ_g) of commonly available thermal greases, sheets and epoxies vary between 4.0-8.89, 0.9-10.0 and 1.55-7.5 $\mathrm{Wm^{-1}K^{-1}}$, respectively. The maximum value is used for modeling, and the maximum and minimum values are used in the determination of restrictive resistances. The resulting thermal resistances are a function of the thickness of the applied grease or epoxy and the surface area $A_{g,cer}$. The thickness is assumed to be 25.4 μm (0.001") as per manufacturer specifications. The $A_{g,cer}$ for the cold- and hot-side heat exchangers within a unit cell is a function of the cross-sectional areas of the n- and p-type thermoelectric legs. The length of the unit cell is two times the maximum of the n- or p-type leg widths plus two times the gap width W_{gap}, which is expressed as half of the maximum of the n- or p-type leg widths. The width of the unit cell is the maximum of the n- or p-type leg plus W_{gap}. Thus, $A_{g,cer}$ is expressed as cell is

$$A_{g,cer} = 4.5\big(\max\big(\sqrt{A_N}, \sqrt{A_P}\big)\big)^2. \tag{2.27}$$

Thus, the thermal resistance associated with the grease is

$$R_{g,cer} = \frac{L_g}{\lambda_g A_{g,cer}}. \tag{2.28}$$

Additionally, the thermal resistances associated with the grease for the hot-side ceramic plate and hot-side interconnector $A_{g,int}$ is a function of the surface area said interconnector top surface area such that

$$A_{g,int} = 2.5\big(\max\big(\sqrt{A_N}, \sqrt{A_P}\big)\big)^2. \tag{2.29}$$

Therefore, the thermal resistance associate with the grease between the hot-side ceramic and interconnector is

$$R_{g,int} = \frac{L_g}{\lambda_g A_{g,int}}. \tag{2.30}$$

The cold-side interconnector is brazed onto the cold-side ceramic plate during manufacturing. The thermal resistance R_{braze} associated with a brazed surface is $0.025 \cdot 10^{-4}$ Km^2W^{-1} per $A_{g,int}$ [137] such that

$$R_{braze} = \frac{(0.025 \cdot 10^{-4})}{A_{g,int}}. \tag{2.31}$$

The thermal resistance associated with the ceramic, which is typically alumina, is simply the length of the ceramic, assumed to be a fixed value of 0.889 mm (or 0.035") over the thermal conductivity times the area such that

$$R_{Cer_{c,h}} = \frac{L_{Cer}}{\lambda_{cer_{c,h}} A_{g,cer}}. \tag{2.32}$$

The thermal resistances of the n- and p-type materials (R_N and R_P, respectively) are the inverse of the thermal conductances such that

$$R_{N,P} = \frac{L_{N,P}}{\lambda_{N,P} A_{N,P}}. \tag{2.33}$$

The thermal resistances associated with interface materials in contact with the top and bottom interconnectors, $R_{N,c}$ and $R_{P,c}$, are functions of the contact conductance λ_{c,N^+} and λ_{c,P^+}, respectively. For this study, it is desirable to have the thermal conductivity of the contact vary between 1 and 400 $Wm^{-2}K^{-1}$ to reflect possible material properties. The thermal resistance of the contact resistance is then evaluated based upon the contact thermal conductivity such that

$$R_{N,c} = \frac{1}{\lambda_{c,N^+} A_N}, \tag{2.34}$$

and

$$R_{P,c} = \frac{1}{\lambda_{c,P^+} A_P}, . \tag{2.35}$$

The thermal resistance associated with convection with the gap is based upon the Rayleigh number Ra, which determines the action of buoyancy driven flow. If the value associated with Ra is less than the critical value of 1,708, the buoyancy forces of the fluid cannot overcome the viscous forces and there is no advection within the cavity, resulting in

the primary mode of heat transfer being conduction. For cases where there is a horizontal cavity with heating from the top surface and the absence participating material in terms of radiation within the cavity, heat transfer is exclusively through conduction. Thus, the convective heat transfer coefficient within the gap is expressed as

$$h_{gap} = \frac{\lambda_{air}}{H}, \tag{2.36}$$

where λ_{air} is the temperature dependent thermal conductivity, as listed in table 1, and H is the height of the cavity. The cavity height H is calculated as the maximum height of the optimized n- or p-type material plus two times the thickness of the copper interconnector, which has a fixed height of 0.5 mm. For cases where the length of the n- or p-type element changed based upon co-optimization, the respective interconnector thickness is increased or decreased such that H reflects 1.0 mm plus the maximum height. The associated thermal resistance is then expressed as

$$R_{conv} = \frac{1}{h_{gap} A_{gap}}, \tag{2.37}$$

where A_{gap} is the exposed cross-sectional area between the top and bottom ceramic plates. Thus, A_{gap} is expressed as

$$A_{gap} = A_{g,cer} - A_{g,int} \tag{2.38}$$

The thermal resistance associated with radiation can be expressed as the inverse of the radiation heat transfer coefficient h_{rad} times A_{gap},

$$R_{rad} = \frac{1}{h_{rad} A_{gap}} \tag{2.39}$$

The radiation heat transfer coefficient is expressed as

$$h_{rad} \equiv \epsilon\sigma(T_{sur} + T_{sur})(T_{sur}^2 + T_{sur}^2). \tag{2.40}$$

The geometry within a thermoelectric device cavity is complicated in terms of multiple temperature-dependent emissivities for participating materials, three-dimensional view factor calculations to determine the extent of participation of each component and resolving the three-dimensional temperature profile within each thermoelectric element as to determine the surface temperature. Therefore, values for h_{rad} have been varied between 0.1, 5, 10 and 15 and 20 $Wm^{-2}K^{-1}$ [88]. In the following chapter (Chap. 3, the resolution of the radiation view factor will be introduced and the proper determination of h_{rad} will be presented.

The total heat transfer is then a function of the temperature at each junction of the thermal resistance network over the respective thermal resistance and is equal for each particular element in series of the thermal resistance network. For the variables of interest, $\eta_{th,max}$ and $P_{o,max}$, it is of particular importance to know the temperature differential across the thermoelectric elements. Therefore, the total heat transfer through the device is expressed as

$$\begin{aligned} Q_h = \frac{T_{\infty,h} - T_{\infty,c}}{R_{tot}} = \frac{T_{\infty,h} - T_{hex,h}}{R_{hex,h}} = \frac{T_{hex,h} - T_{cer,1,h}}{R_{g,cer}} = \\ \frac{T_{cer,1,h} - T_{cer,2,h}}{R_{cer,h}} = \frac{T_{cer,2,h} - T_{Cu,1,h}}{R_{g,int}} = \frac{T_{Cu,1,h} - T_{Cu,2,h}}{R_{Cu,h}} = \\ \frac{T_{Cu,2,h} - T_{Cu,1,c}}{R_{||}} = \frac{T_{Cu,1,c} - T_{Cu,2,c}}{R_{Cu,c}} = \frac{T_{Cu,2,c} - T_{cer,1,c}}{R_{braze}} = \\ \frac{T_{cer,1,c} - T_{cer,2,c}}{R_{cer,c}} = \frac{T_{cer,2,c} - T_{hex,c}}{R_{g,cer}} = \frac{T_{hex,c} - T_{\infty,c}}{R_{hex,c}}. \end{aligned} \tag{2.41}$$

It is noted that the three-dimensional steady-state general energy equation taking into account conduction, Joule heating and the Peltier and Thomson effects for the semiconductors is expressed as

$$0 = \nabla(\kappa \nabla T) + \rho \mathbf{J}^2 - T\mathbf{J} \cdot \left[(\nabla \alpha)_T + \left(\frac{\delta \alpha}{\delta T} \right) \nabla T \right] \tag{2.42}$$

where $\mathbf{J}$ is the current density. For simplicity, the one-dimensional effects of conduction, Peltier effect and Joule heat will be treated; the Thomson effect, although unique, does not contribute substantially to the heat input. Thus, describing the heat input into the p- and n-type materials such that Q_N and Q_P can be expressed as a sum such that

$$Q_h = K\Delta T + (|\alpha_N| + |\alpha_P|)T_h I - \frac{1}{2} I^2 R_{el}. \tag{2.43}$$

The temperature difference is defined as $\Delta T = T_h - T_c$ across the respective pellet. This results in the expression for Q_N and Q_P as

$$Q_N = K_N \Delta T_N + \alpha_N T_{N,h} I - \frac{1}{2} I^2 R_{el,N}. \tag{2.44}$$

Similarly, the heat flow through the p-type leg is expressed as

$$Q_P = K_P \Delta T_P + \alpha_P T_{P,h} I - \frac{1}{2} I^2 R_{el,P}. \tag{2.45}$$

The current I is defined as

$$I = \left(\frac{(|\alpha_N| + |\alpha_P|)\Delta T}{R(m'_{opt} + 1)} \right). \tag{2.46}$$

2.3 METHODOLOGY

The properties of the thermoelectric materials ($\rho_{N,P}, \lambda_{N,P}, \alpha_{N,P}$), interconnectors and ceramic ($\lambda_{Cu_{c,h}}$, $\lambda_{cer_{c,h}}$) and air (λ_{air}) were evaluated as the integral of said property over the temperature range ΔT the material is experiencing divided by ΔT. For instance

$$\rho(T) = \frac{1}{\Delta T} \int_{T_c}^{T_h} \rho(T) dT. \tag{2.47}$$

For the optimization of the leg geometry, varying the n-type material, the cross-sectional area A_N and length L_N were varied between 1 mm^2 and 10 cm^2 and 0.5 mm and 10 mm, respectively. The cold-side temperature $T_{\infty,c}$ was kept fixed at 25 °C and the hot-side temperature was varied from 50 °C to 450 °C. The thermal conductivity and electrical resistivity of the interface material Π were varied between 1-400 Wm^{-2}K^{-1} and 10^{-10}-10^{-1} Ωm, respectively. The systems of equations used to solve the cross-sectional areas A_N and A_P and lengths L_N and L_P (Eqn. 2.21a- 2.24) used a convergence criteria of 10^{-15} for the residuals between successive iterations. A convergence criteria of 10^{-10} was used for resolving the temperature at each location within the device.

To study the effect of the heat exchanger effective surface area A_{eff} and cold- and hot-side convective heat transfer coefficients h_c and h_h, respectively, as well as the cross-sectional areas and the lengths of the n- and p-type materials (A_N/A_P and L_N/L_P, respectively), an iterative approach was taken to solve a system of equations. The steps are listed below:

1. Guess the initial temperatures at each locations, excluding the given cold- and hot-side fluids flows ($T_{hex,h}$, $T_{cer,1,h}$, $T_{cer,2,h}$, $T_{Cu,1,h}$, $T_{Cu,2,h}$, $T_{N,h}$, $T_{P,h}$, $T_{N,c}$, $T_{P,c}$, $T_{Cu,1,c}$, $T_{Cu,2,c}$, $T_{cer,1,c}$, $T_{cer,2,c}$, $T_{hex,c}$) as well as the geometry of the thermoelectric elements (A_N, A_P, L_N, L_P). The area and length of the n-type material will remain invariant.
2. Solve the thermal resistances for each of the components within the system based upon the temperatures and geometry in Step 1 using eqns. 2.25-2.40.
3. Solve the system of eqns. 2.21a-2.24 based upon the temperatures provided in Step 1. The temperature difference across the thermoelectric elements must be used as the ΔT to evaluate the temperature dependent properties.

4. Re-solve the temperatures for each location (as provided in Step 1) based upon eqn. 2.41. Note that for the parallel portion of the thermal resistance, as illustrated in Fig. 3, that the temperature at the thermoelectric element interfaces is reduced by the presence of thermal and electrical contact resistances. Equations 2.44 and 2.45 are to be used to solve for the heat input and temperature difference across the p-n junction based on the result of eqn. 2.46.

5. Use the temperatures solved for in Step 4 to initialize the system of equations and repeat Steps 2-4 until the desired convergence criteria is achieved.

Tables 1 and 2 provide the polynomial fit to published data [136] for each material's temperature dependent thermoelectric properties, as well as the temperature dependent thermal conductivity of air, copper and alumina. Note the high number of significant digits for the high-order polynomial fits. This was done as to provide a continuous curve and integral thereof; piece-wise fits led to jump in material properties when the integral is evaluated.

2.4 RESULTS AND DISCUSSION

The results of the proposed analytical model are presented in the following sections. The individual effects of thermoelectric material leg length and cross-sectional area on thermal conversion efficiency and power output are presented in Sec. 2.4.1, those of thermal and electrical contact resistances in Sec. 2.4.2, those of cold- and hot-side heat transfer coefficients in Sec. 2.4.3, those of cold- and hot-side heat exchanger effective area in Sec. 2.4.4, those of radiation heat transfer coefficient in Sec. 2.4.5 and lastly, the contribution of the hot-side ceramic and greases to the the total device thermal resistance in Sec. 2.4.6. The presented analytical model is validated against published numerical and analytical models, as discussed in Secs. 2.4.7.1 and 2.4.7.2, respectively.

Table 1: Polynomial expressions for temperature dependent properites air of and copper and temperature dependent thermoelectric properties of n-type (75% Bi_2Te-25% Bi_2Se_3).

Air Temperature Dependent Properties	
λ_{air}	$= (-1.15764 \cdot 10^{-19})T^6 + (4.20706 \cdot 10^{-16})T^5 + (-5.65964 \cdot 10^{-13})T^4 + (3.58854 \cdot 10^{-10})T^3 + (-1.43582 \cdot 10^{-7})T^2 + (1.13316 \cdot 10^{-4})T + -8.83200 \cdot 10^{-4}$
Copper Temperature Dependent Properties	
λ_{Cu}	$= (1.5625 \cdot 10^{-5})T^2 - (8.5625 \cdot 10^{-2})T + 405.5458$
Alumina Temperature Dependent Properties	
$\lambda_{Al_2O_3}$	$= (1.59094 \cdot 10^{-21})T^8 + (-8.88821 \cdot 10^{-18})T^7 + (1.982762 \cdot 10^{-14})T^6 + (-2.27443 \cdot 10^{-11})T^5 + (1.43569 \cdot 10^{-8})T^4 + (-4.96184 \cdot 10^{-6})T^3 + (9.35539 \cdot 10^{-4})T^2 + (-1.45821 \cdot 10^{-1})T + 3.69232$
N-type Temperature Dependent Properties	
α_N	$= -10^{-6}((-1.6143 \cdot 10^{-11})T^5 + (2.5402 \cdot 10^{-8})T^4 + (-1.3005 \cdot 10^{-5})T^3 + (1.5740 \cdot 10^{-3})T^2 + (2.2600 \cdot 10^{-1})T + 151.7414)$
λ_N	$= (2.450582 \cdot 10^{-24})T^{10} + (5.109899 \cdot 10^{-21})T^9 + (-4.510135 \cdot 10^{-18})T^8 + (2.178044 \cdot 10^{-15})T^7 + (-6.115171 \cdot 10^{-13})T^6 + (9.228872 \cdot 10^{-11})T^5 + (-3.314373 \cdot 10^{-9})T^4 + (-1.201894 \cdot 10^{-6})T^3 + (1.835354 \cdot 10^{-4})T^2 + (-8.158729 \cdot 10^{-3})T + 1.44964$
ρ_N	$= 10^{-6}((-2.4900 \cdot 10^{-14})T^6 + (4.3202 \cdot 10^{-11})T^5 + (-2.7176 \cdot 10^{-8})T^4 + (7.2921 \cdot 10^{-6})T^3 + (-7.6043 \cdot 10^{-4})T^2 + (4.3210 \cdot 10^{-2})T + 9.3562)$

Table 2: Polynomial expressions for temperature dependent thermoelectric properites for p-type (25% Bi_2Te_3-75% Sb_2Te_3 (1.75% excess Se))

P-type Temperature Dependent Properties	
α_P	$= 10{\cdot}10^{-6}$ ((-9.9217017368$\cdot 10^{-32}$)T^{15} + (3.4315860737$\cdot 10^{-28}$)T^{14} + (-5.345201892$\cdot 10^{-25}$)T^{13} + (4.9519818014$\cdot 10^{-22}$)T^{12} + (-3.0351760507$\cdot 10^{-19}$)T^{11} + (1.2952100724$\cdot 10^{-16}$)T^{10} + (-3.9434353361$\cdot 10^{-14}$)T^{9} + (8.6358110935$\cdot 10^{-12}$)T^{8} + (-1.3542345669$\cdot 10^{-9}$)T^{7} + (1.4960998003$\cdot 10^{-7}$)T^{6} + (-1.1294984997$\cdot 10^{-5}$)T^{5} + (5.5279337202$\cdot 10^{-4}$)T^{4} + (-1.5833319782$\cdot 10^{-2}$)T^{3} + (2.0081335874$\cdot 10^{-1}$)T^{2} + (6.2555051292$\cdot 10^{-1}$)T + 1.7127199231$\cdot 10^{2}$)
λ_P	$=$ (2.635446577727367$\cdot 10^{56}$)T^{25} + (-1.178219342120757$\cdot 10^{-52}$)T^{24} + (2.376614174944398$\cdot 10^{-49}$)T^{23} + (-2.835773329774781$\cdot 10^{-46}$)T^{22} + (2.195032606710057 $\cdot 10^{-43}$)T^{21} + (-1.126139199959475$\cdot 10^{-40}$)T^{20} + (3.657386143019148$\cdot 10^{-38}$)T^{19} + (-6.031174933589776$\cdot 10^{-36}$)T^{18} + (-1.164006750359995$\cdot 10^{-34}$)T^{17} + (7.248128052130643$\cdot 10^{-32}$)T^{16} + (1.308544300658960$\cdot 10^{-28}$)T^{15} + (-6.084211862875450$\cdot 10^{-26}$)T^{14} + (2.248277280547425$\cdot 10^{-24}$)T^{13} + (7.306162726233390$\cdot 10^{-21}$)T^{12} + (-3.525558711111976$\cdot 10^{-18}$)T^{11} + (9.451992092943977$\cdot 10^{-16}$)T^{10} + (-1.734827677456562$\cdot 10^{-13}$)T^{9} + (2.319378705499120$\cdot 10^{-11}$)T^{8} + (-2.309408508575470$\cdot 10^{-09}$)T^{7} + (1.719566017728193$\cdot 10^{-07}$)T^{6} + (-9.499553414570762 $\cdot 10^{-06}$)T^{5} + (3.819584975471945$\cdot 10^{-04}$)T^{4} + (-1.080477383045247$\cdot 10^{-02}$)T^{3} + (2.026712996426282$\cdot 10^{-01}$)T^{2} + (-2.246210315616978)T + 11.99592062227707
ρ_P	$= 10{\cdot}10^{-6}$((-8.9007$\cdot 10^{-12}$)T^{5} + (1.3390$\cdot 10^{-8}$)T^{4} + (-7.5260$\cdot 10^{-6}$)T^{3} + (1.6908$\cdot 10^{-3}$)T^{2} + (-7.9785$\cdot 10^{-2}$)T + 11.4586)

2.4.1 Effect of Leg Length Cross-sectional Area

The effect of leg length L_N and cold-side convective heat transfer coefficient h_c on $\eta_{th,max}$ and $P_{o,max}$ for optimized (eqn 2.21a, 2.22, 2.23a and 2.24) and non-optimized geometries (A_N=A_P, L_N=L_P) excluding Π for a given $T_{\infty,h}$=450 °C, h_h=100 and h_{rad}=0.01 $Wm^{-2}K^{-1}$, $A_{eff_{c,h}}$=10^{-3} m^2 and A_N=10^{-7} m^2 are presented in Fig. 4a and b. The efficiency of the uni-couple exhibits an increase with an increment in L_N for all h_c values, however, the increases is less than 5% of the maximum when L_N exceeds 2.5 mm for h_c values above 5 $Wm^{-2}K^{-1}$; the percent increase diminishes with an increase in L_N. The most substantial increase in $\eta_{th,max}$ occurs when h_c increases from 1 to 5 $Wm^{-2}K^{-1}$, with a 83.2% and 10.8% increase when L_N equals 0.5 and 10 mm, respectively.

The maximum thermal conversion efficiency for the optimized geometry exhibits an increase in comparison to the non-optimized geometry cases when h_c is greater than 10 $Wm^{-2}K^{-1}$; below this value $\eta_{th,max}$ experiences a slight decrease in performance for lesser L_N values, as seen in Fig 4a. For instance, when h_c=10 and 500 $Wm^{-2}K^{-1}$, the percent increase in $\eta_{th,max}$ is 0.58% and 1.51%, respectively. Similarly, the optimized geometry cases yields an increase in $P_{o,max}$ for all h_c value in comparison to the non-optimized geometry cases. For a given h_c value of 1, 5, 10 and 500 $Wm^{-2}K^{-1}$, $P_{o,max}$ increases by 0.98%, 8.06%, 8.93% and 9.71% for the optimized geometry cases in comparison the to non-optimized geometry cases, as seen in Fig. 4b.

It is evident increasing L_N yields a logarithmic decrease in $P_{o,max}$ as seen in Fig. 4b. Increasing h_c per given $T_{\infty,h}$ and h_h values substantially increases $P_{o,max}$ for lesser L_N values. The effect of increasing h_c on $P_{o,max}$ diminishes when h_c exceeds 5 $Wm^{-2}K^{-1}$. Additionally, for L_N values above 2.5 mm, $P_{o,max}$ increases less than 10% of the maximum when h_c values increase from 5 to 500 $Wm^{-2}K^{-1}$.

Increasing L_N increases the electrical resistance associated with the p- and n-type legs for the prescribe cross-sectional area and decreases the temperature difference ΔT across the junction per prescribed operating conditions. This subsequently reduces the produced current (eqn. 2.46). With an increase in electrical resistance and reduced current, $P_{o,max}$ (I^2R) diminishes due to the dependence on current squared. The reduced $P_{o,max}$ combined

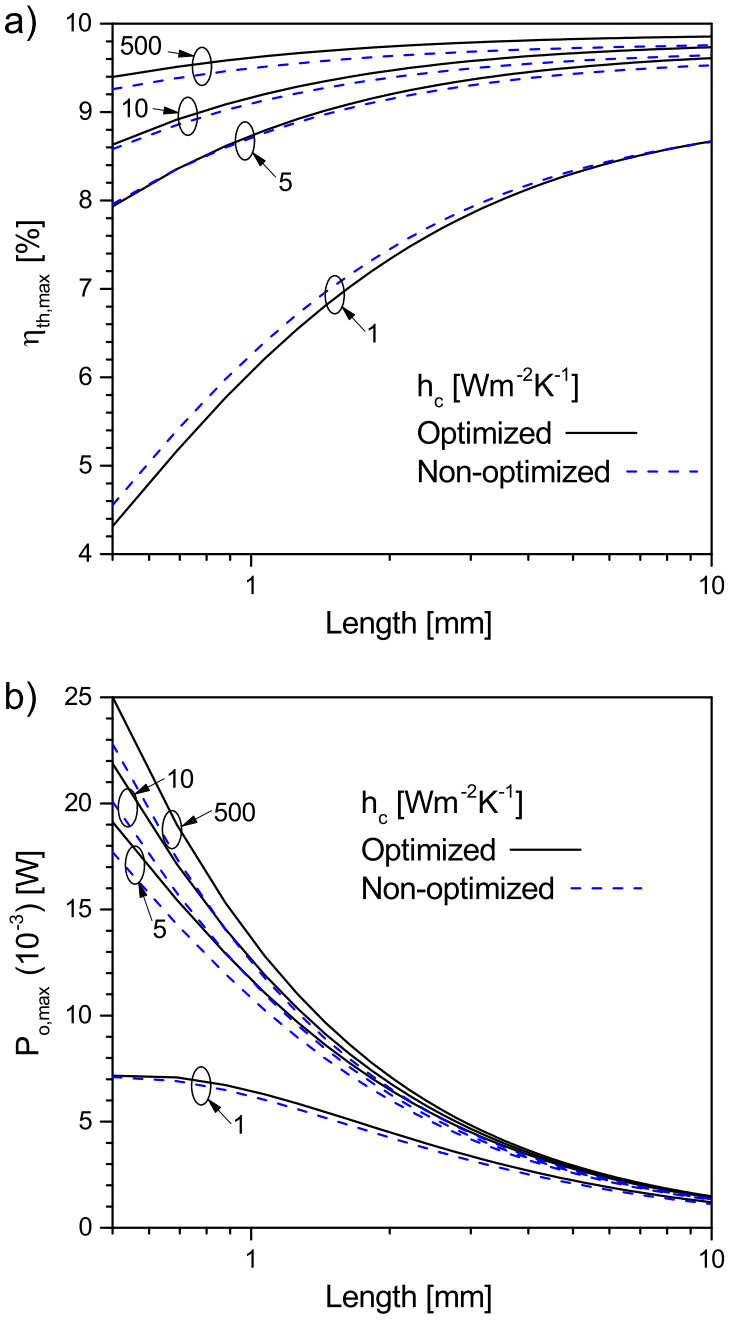

Figure 4: Effect of thermoelectric length length L_N and h_c on $\eta_{th,max}$ and $P_{o,max}$ for optimized and non-optimized geometry cases when $T_{\infty,h}$=450 °C, h_h=100 and h_{rad}=0.01 Wm^{-2}K^{-1}, $A_{eff_{c,h}}$=10^{-3} m^2, A_N=10^{-7} m^2 and ∄Π.

with a reduced heat input into the p-n junction yields an increase in $\eta_{th,max}$ (equivalently expressed as P_o/Q_h). Although the power output decreases substantially with an increase in L_N, the decrease in heat input with an increase in L_N outweighs the decrement in P_o and results in an increasing trend in $\eta_{th,max}$ with L_N.

Increasing the cross-sectional area of the n-type material has non-linear effects on $\eta_{th,max}$ and $P_{o,max}$ for both the optimized and non-optimized cases. Fixing the cold- and hot-side heat exchanger areas at 10^{-3} m^2, the hot-side heat transfer coefficient at 100 $Wm^{-2}K^{-1}$, the cold- and hot-side fluid temperatures at 25 °C and 450 °C, respectively, and the length of the n-type material at 0.5 mm, the effect of increasing n-type cross-sectional area and cold-side convective heat transfer coefficient on $\eta_{th,max}$ and $P_{o,max}$ are illustrated in Fig. 5a and b, respectively. For a set h_c value, increasing A_N non-linearly decreases $\eta_{th,max}$ from a maximum value when A_N=10^{-7} m^2 to a minimum when A_N=10^{-3} m^2. With an increase in cross-sectional area, the temperature difference across the p-n junction diminishes due to increased conduction through the thermoelectric element leg, or alternatively, due a decrease in thermal resistance of the legs (eqn. 2.33). Without the development of a temperature difference across the junction, the device will have diminished Seebeck voltage production, which in turns diminishes the produced current and Ohmic voltage potential, thereby decreasing power output. Additionally, the diminished power output is coupled with an increased heat input, due to lesser thermal resistance of the module, and thus efficiency decreases.

Increasing h_c for a fixed h_h allows a larger temperature difference to be established across the thermoelectric element junction for the same cross-sectional area and operating parameters. Increasing h_c reduces the thermal resistance associated with the heat exchanger, increases heat input, thereby establishing a greater ΔT and increasing the power output of the unicouple. As h_c increases, the operational envelope of higher efficiency is extended for increasing A_N values, as seen by the continuation of high $\eta_{th,max}$ with an increase in A_N values, as represented in Fig. 5a. The performance of the optimized in comparison to non-optimized cases is dependent upon A_N and h_c values. For large h_c values above 10^2 $Wm^{-2}K^{-1}$ and A_N values below 10^{-5} m^2, the optimized geometry exhibits an increase in $\eta_{th,max}$ of 1.6%. As h_c decreases below 10^2 $Wm^{-2}K^{-1}$, the non-optimized geometry exhibits a slight increase in $\eta_{th,max}$ values.

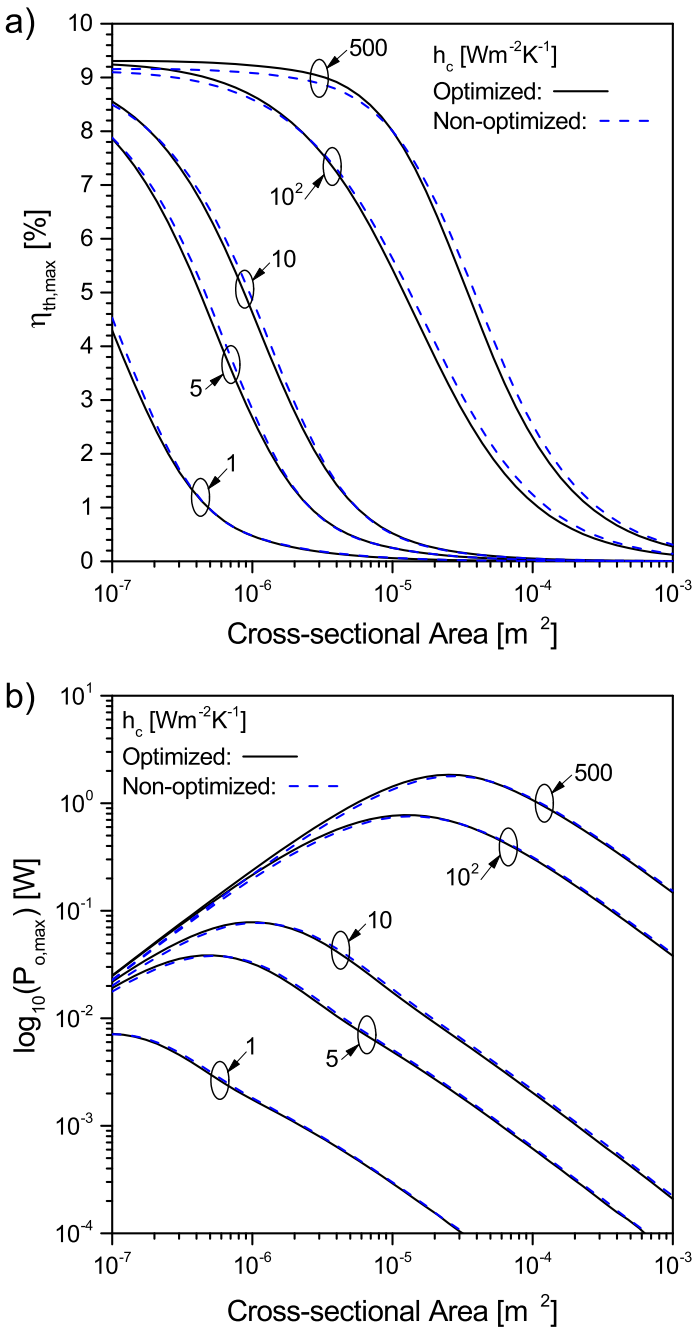

Figure 5: Effect of thermoelectric cross-sectional area A_N on and h_c on $\eta_{th,max}$ and $P_{o,max}$ for optimized and non-optimized geometry cases when $T_{\infty,h}$=450 °C, h_h=100 and h_{rad}=0.01 Wm^{-2}K^{-1}, $A_{eff_{c,h}}$=10^{-3} m^2, L_N=0.5 mm and ♯Π.

Similarly, cross-sectional area has an effect on $P_{o,max}$ for various h_c values, as illustrated in Fig. 5b. For a given h_c value, increasing A_N leads to an increase and then decrease in $P_{o,max}$ value. The reasons are similar to those presented for the effect of A_N on $\eta_{th,max}$, although the trend is not non-linearly decreasing for increasing A_N values. It is evident from Fig. 5b that there exists an A_N value that maximizes $P_{o,max}$. The optimized geometry yields an improvement in $P_{o,max}$ with increasing A_N values until the maximum value is reached, then the non-optimized geometry exhibits a marginal increase in $P_{o,max}$ with further increasing A_N values. Likewise, for a fixed A_N value, increasing h_c non-linearly increases $P_{o,max}$. With an increase of h_c, there is greater heat input and a larger temperature difference imposed across the unicouple junction, thus a greater power output.

2.4.2 Effect of Contact Resistances

The inclusion of thermal and electrical contact resistances diminishes the performance of a thermoelectric device. The introduction of a thermal contact resistance diminishes the temperature difference across the n-type and p-type material, as graphically illustrated in Fig. 3, per given operating conditions, thus decreasing the generated Seebeck voltage $\alpha\Delta T$, which in turns decreases the generated current and Ohmic voltage potential. Additionally, with the introduction of a thermal contact resistance, the heat input into the p-n junction is reduced due an increase in the total device thermal resistance. Thus, the thermal contact resistance is responsible for decreasing both efficiency and power output. The introduction of an electrical contact resistance has a similar effect on efficiency and power output as does thermal resistance. An increase in electrical resistance associated with the contact material increases the amount of Joule heating within said material, thereby decreasing the temperature difference across the n- and p-type materials.

The effect of increasing thermal and electrical contact resistances on the power output of optimized and non-optimized geometries considering the existence of a contact material ($\exists\Pi$) by resolving eqns. 2.23b and 2.24 is presented in Figs. 6a and b. It is evident for fixed h_h values of 500 $Wm^{-2}K^{-1}$ that a h_c value below 5 $Wm^{-2}K^{-1}$ results in a slight decrease in $P_{o,max}$ values as predicted by the optimized case in comparison to the non-optimized case.

Values greater than 5 $Wm^{-2}K^{-1}$ result in the optimized geometry producing greater $P_{o,max}$ values than non-optimized cases when the thermal resistance exists between 10^{-6} and $4{\cdot}10^{-4}$ $Wm^{-2}K^{-1}$; above $4{\cdot}10^{-4}$ $Wm^{-2}K^{-1}$ the non-optimized geometry yields greater $P_{o,max}$ values. Increasing R_{th} results in a non-linear decrease decrease in $P_{o,max}$ value predicted by both the optimized and non-optimized cases.

Although Figs. 6a b indicate that the power produced by the optimized case is less than that of the non-optimized case for lower h_c values and higher R_{th} values, this comparison does not portray the true benefit of the geometric optimization process. The geometry, in particular length and cross-sectional area, of the p-type thermoelectric element is optimized, while the geometry of the n-type thermoelectric material is held invariant, to maximize the power output of the unicouple. In doing so, there is lesser material volume. Comparing the power density, or power produced per volume of thermoelectric material, of the optimized and non-optimized geometries indicates that for all R_{th}, R_{el} and h_c values the optimized case outperforms the non-optimized case, as seen in Figs. 7a and b. For instance, with R_{el}=10^{-10} Ωm^2 and for a h_c value of 500 $Wm^{-2}K^{-1}$, the optimized geometry cases predicts an increase in $P_{o,max}$ values of 28.9% in comparison to the non-optimized geometry cases.

Similarly, the effect of thermal contact resistance R_{th} on the thermal conversion efficiency for optimized and non-optimized cases are presented in Figs. 8a and b. The hot-side fluid temperature was held at 450 °C while the cold-side fluid temperature was held invariant at 25 °C. The cold- and hot-side convective heat transfer coefficients were varied between $2{\cdot}10^2$ and 10^4 $Wm^{-2}K^{-1}$ while h_{rad} was held invariant at 0.01 $Wm^{-2}K^{-1}$. The n-type leg length and cross-sectional area were held invariant at 5 mm and 10^{-4} m^2, while the cold- and hot-side heat exchanger effective areas we held constant at 10^{-3} m^2. The electrical resistance was held invariant at 10^{-10} Ωm^2. As seen in Fig. 8a, with an increase in R_{th}, $\eta_{th,max}$ non-linearly decreases due to a decrease in hot-side junction temperature and an increase in cold-side junction temperature, due to an increase in total system thermal resistance. As h_c and h_h increases, a larger temperature difference is able to maintained across the thermoelectric element legs, leading to larger $\eta_{th,max}$ values.

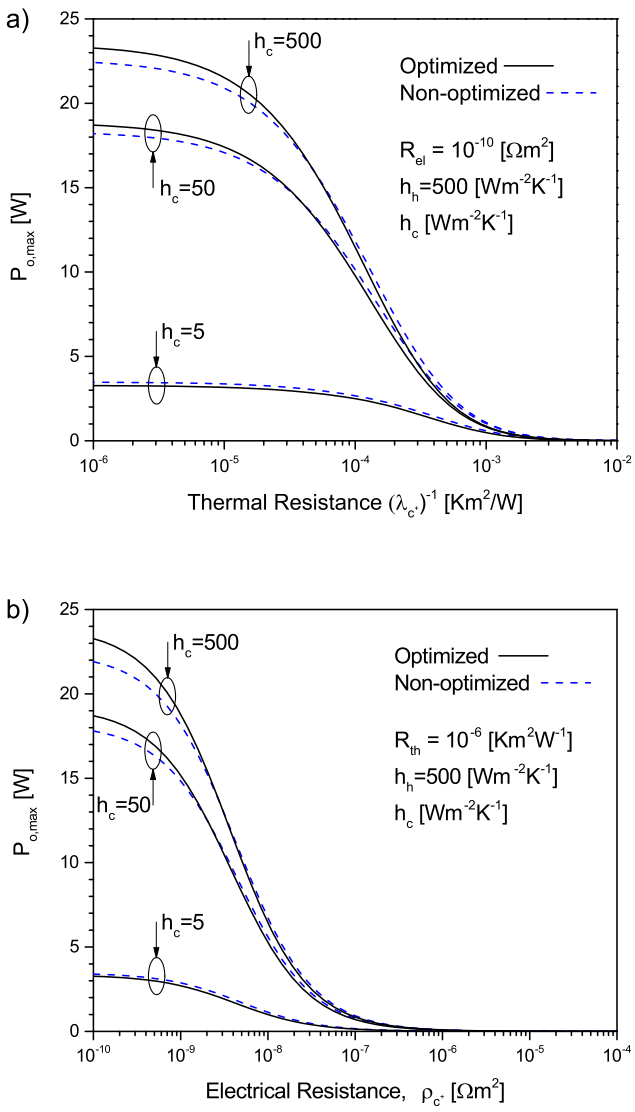

Figure 6: Effect of a) thermal contact resistance R_{th}=$1/\lambda_{c^+}$ on $P_{o,max}$ with ρ_{c^+}=10^{-10} Ωm^2, h_{rad} and h_h equaling 0.01 and 500 Wm^{-2}K^{-1}, respectively, for various h_c values. The geometry is prescribed as $A_{eff_{c,h}}$=10^{-1} m^2, A_N=10^{-4} m^2, L_N=$5{\cdot}10^{-4}$ m and a hot-side fluid temperature of 450 °C and b) electrical contact resistance R_{el}=ρ_{c^+} with R_{th}=10^{-6} Km^{2}W^{-1} for the same operating and geometrical conditions.

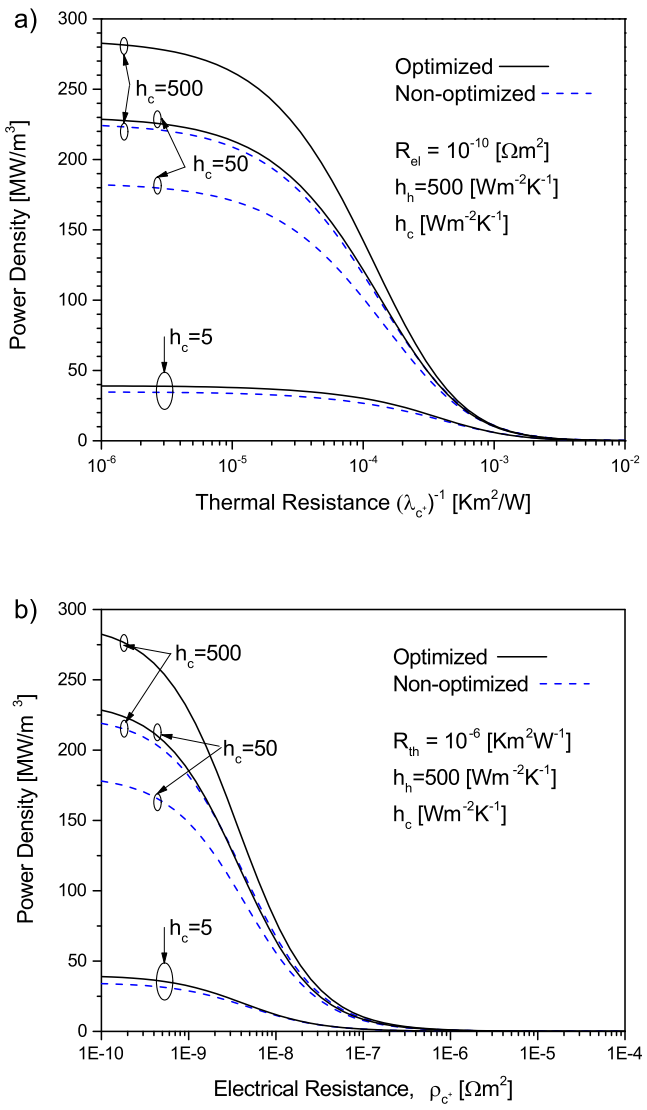

Figure 7: Effect of a) thermal contact resistance R_{th}=$(\lambda_{c^+})^{-1}$ on power density with ρ_{c^+}=10^{-10} Ωm^2, h_{rad} and h_h equaling 0.01 and 500 Wm^{-2}K^{-1}, respectively, for various h_c values. The geometry is prescribed as $A_{eff_{c,h}}$=10^{-1} m^2, A_N=10^{-4} m^2, L_N=$5{\cdot}10^{-4}$ m and a hot-side fluid temperature of 450 °C and b) electrical contact resistance R_{el}=$(\rho_{c^+})^{-1}$ with R_{th}=10^{-6} Km^{2}W^{-1} for the same operating and geometrical conditions.

As was seen with $P_{o,max}$ versus R_{th} in Fig. 6a, the optimized geometry exhibits marginal gains in $\eta_{th,max}$ as compared to the non-optimized geometry for larger h_c and h_h values with a maximum improvement of 1.15% for minimum R_{th} values; for h_c and h_h values less than 10^3, the optimized geometry underperforms the non-optimized geometry.

Increasing the electrical resistance ρ_{c^+} non-linearly decrease $\eta_{th,max}$ as seen in Fig. 8b. An increase in ρ_{c^+} increases the Joule heating of the interface material, decreasing and increasing the hot- and cold-side junction temperatures of each thermoelectric material element, respectively. Increasing the convective heat transfer coefficients allows the establishment of a greater temeperature difference across the thermoelectric element legs resulting in greater $\eta_{th,max}$ values. Although $\eta_{th,max}$ increases with increasing h_c and h_h values, the values of ρ_{c^+} that cause a decline in $\eta_{th,max}$ are lesser for higher convective heat transfer coefficient values. With the established of a greater temperature difference across the thermoelectric element leg, there is greater Seebeck voltage generated and consequently a larger Ohmic voltage potential and current. With an increase in current, the junction temperature is more sensitive to the electrical resistivity of the junctions, ρ_{c^+}, proportional to current squared and ρ_{c^+}. Thus, a decrease $\eta_{th,max}$ occurs sooner for lesser ρ_{c^+} values when evaluated at higher convective heat transfer coefficient values. The optimize geometry exhibits marginal gains in $\eta_{th,max}$, on the order of one percent, in comparison to non-optimized geometries for lesser ρ_{c^+} and h_c and h_h values.

Although Figs. 8a and b illustrate the $\eta_{th,max}$ values produced by the optimized geometry as often less than those produced by the non-optimized case for lesser h_c and h_h values and larger R_{th} values, it is most insightful to compare the volumetric efficiency of the optimized and non-optimized geometries as presented in Fig. 9a and b. The optimization process adjusts the cross-sectional area and length of p-type material with respect to the fixed geometry of the n-type material. By evaluating the volumetric efficiency, or efficiency per volume of material used, it is evident the optimized geometry exhibits substantial gains in performance for increasing R_{th} and R_{el} values for presented convective heat transfer coefficients in comparison to non-optimized geometries. When studying the effect of R_{th}, the optimized geometry yields an increase in volumetric efficiency of 10.2%, 21.6% and 8.3% in comparison to the non-optimized geometries when the convective heat transfer coefficients

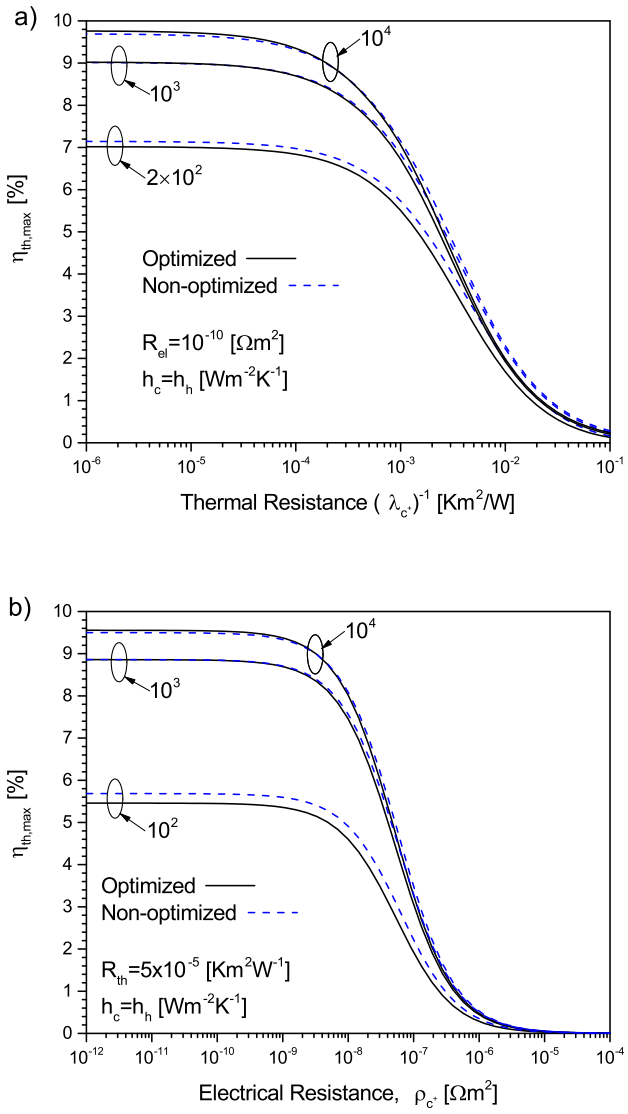

Figure 8: Effect of a) thermal contact resistance $R_{th}=(\lambda_{c^+})^{-1}$ on maximum thermal conversion efficiency $\eta_{th,max}$ with $\rho_{c^+}=10^{-10}$ Ωm^2, h_{rad} equaling 0.01 for various $h_c=h_h$ values. The geometry is prescribed as $A_{eff_{c,h}}=10^{-3}$ m^2, $A_N=10^{-4}$ m^2, $L_N=5$ mm and a hot-side fluid temperature of 450 °C and b) electrical contact resistance $R_{el}=(\rho_{c^+})^{-1}$ with $R_{th}=5\cdot10^{-5}$ Km^2W^{-1} for the same operating and geometrical conditions.

were 10^2, 10^3 and 10^4 $Wm^{-2}K^{-1}$, respectively, when R_{th} was evaluated at a minimum. For all R_{th} and convective heat transfer coefficient values, the optimized geometry exhibits higher volumetric efficiency values than the non-optimized geometry. When studying the effect of R_{el}, the optimized geometry exhibits an increase in volumetric efficiency of 11.8%, 5.1% and 6.0% for cases when the convective heat transfer coefficients were 10^2, 10^3 and 10^4 $Wm^{-2}K^{-1}$, respectively, and when R_{el} was evaluated at a minimum. As R_{el} increased, the optimized geometry achieved a higher volumetric efficiency than the non-optimized geometry for all convective heat transfer coefficients.

2.4.3 Effect of Heat Transfer Coefficient and Fluid Temperature

By varying the cold- and hot-side convective heat transfer coefficients $1 \leq h_c$ ($Wm^{-2}K^{-1}$)≤ 500 and $10^2 \leq h_h$ ($Wm^{-2}K^{-1}$)$\leq 10^4$ while keeping the remaining parameters constant ($A_{eff_{c,h}}$=10^{-3} m^2, h_{rad}=0.01 $Wm^{-2}K^{-1}$, L_N=0.5 mm, A_N=10^{-7} m^2 and hot fluid temperature $T_{\inf,h}$=450 °C), the effect of h_c and h_h on $\eta_{th,max}$ and $P_{o,max}$ are able to be determined.

The effects of h_c and h_h on $\eta_{th,max}$ are presented in Fig. 10. Increasing h_c with h_h ranging from 10^2 to 10^4 $Wm^{-2}K^{-1}$ yields an asymptotically increasing trend in $\eta_{th,max}$, with $\eta_{th,max}$ approaching a value of 9.30% and 9.32% for the h_h of 10^2 and 10^4 $Wm^{-2}K^{-1}$, respectively. Maximizing $\eta_{th,max}$ based on operating conditions yields the same trend and values in efficiency for h_h between 10^2 and 10^4 $Wm^{-2}K^{-1}$. Contrarily, keeping h_c invariant at 500 $Wm^{-2}K^{-1}$ while increasing h_h from 10^2 to 10^4 $Wm^{-2}K^{-1}$ yields an insignificant change in values. Efficiency remains invariant due to optimization of the material geometry per given operating conditions.

The effect of h_c on $P_{o,max}$ and $\eta_{th,max}$ for optimized and non-optimized geometries (A_N=A_P, L_N=L_P), with h_h fixed at 10^4 $Wm^{-2}K^{-1}$ and aforementioned heat exchanger and geometry values, are presented in Fig. 10. As h_c increases, $P_{o,max}$ asymptotically increases, plateauing to a maximum after h_c ≈50-100 $Wm^{-2}K^{-1}$. The optimized geometry yields an increases in $P_{o,max}$ values in comparison to the non-optimized geometry for the entire range of h_c values, with $P_{o,max}$ increasing by 0.98% to 8.88% when h_c equals 1 and 500 $Wm^{-2}K^{-1}$, respectively. The thermal conversion efficiency $\eta_{th,max}$ exhibits an asymptotic increase with

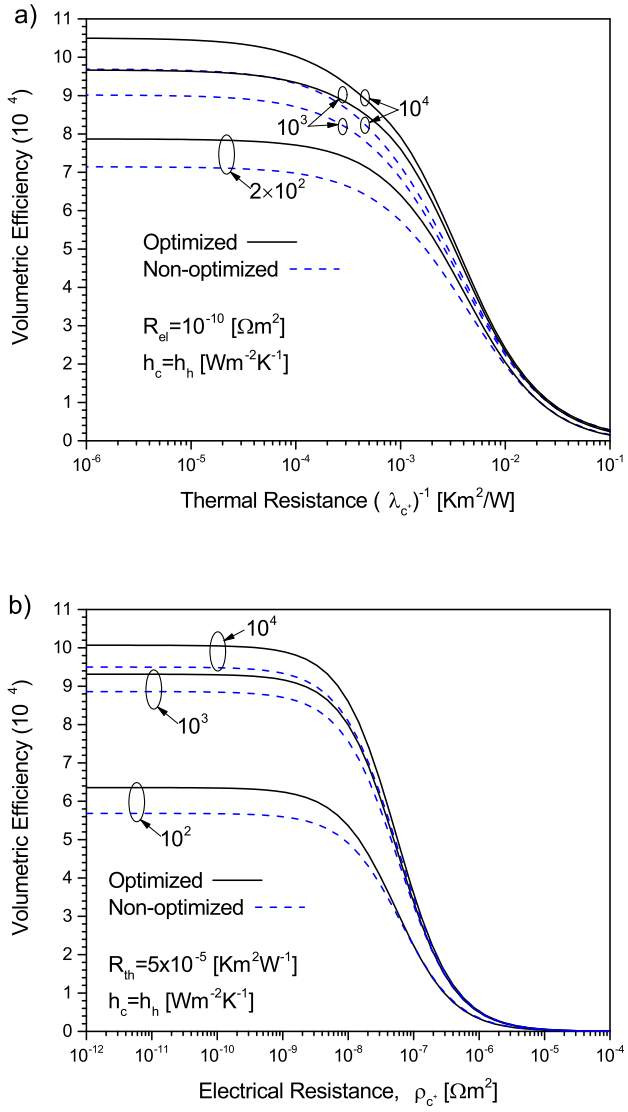

Figure 9: Effect of a) thermal contact resistance R_{th}=$(\lambda_{c^+})^{-1}$ on volumetric efficiency with ρ_{c^+}=10^{-10} Ωm^2, h_{rad} equaling 0.01 for various h_c=h_h values. The geometry is prescribed as $A_{eff_{c,h}}$=10^{-3} m^2, A_N=10^{-4} m^2, L_N=5 mm and a hot-side fluid temperature of 450 °C and b) electrical contact resistance R_{el}=ρ_{c^+} with R_{th}=$5{\cdot}10^{-5}$ Km^{2}W^{-1} for the same operating and geometrical conditions.

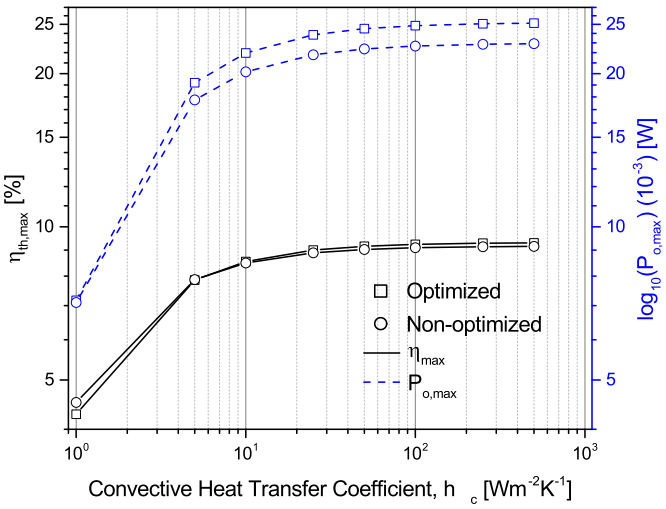

Figure 10: Effect of h_c on η_{max} and $P_{o,max}$ for the case when $A_{eff_{c,h}}$=10^{-3} m^2, h_{rad}=0.01 $Wm^{-2}K^{-1}$, ∄Π, L_N=0.5 mm, A_N=10^{-7} m^2, hot fluid temperature $T_{\inf,h}$=450 °C

an increase in h_c. For h_c=1 and 5 $Wm^{-2}K^{-1}$, the non-optimized geometry system exhibits a larger $\eta_{th,max}$ value in comparison to the optimized geometry system by 5.5% and 0.2%, respectively. Above h_c=5 $Wm^{-2}K^{-1}$, the optimized geometry system exhibits an improvement in $\eta_{th,max}$ over the non-optimized geometry system with an increase of h_c, with η_{max} achieving an average increase of 1.3%.

The effects of h_c and h_h on $P_{o,max}$ are presented in Fig. 11. For a fixed h_c value, increasing h_h yields an asymptotically increasing $P_{o,max}$ value; however, for a given h_c, increasing h_h by two orders of magnitude results in half of a percentage increase in $P_{o,max}$. For a fixed h_h value, increasing h_c results in a substantial increase in $P_{o,max}$. For all h_h values, a two order of magnitude increase in h_c results in a 30.9% increase in $P_{o,max}$, with $P_{o,max}$ following an asymptotically increasing trend with respect to h_c. The trends of $P_{o,max}$ with respect to h_c and h_h are dependent upon the temperature difference imposed across the p-n junction. Increasing h_c and h_h reduces the thermal resistance associated with the respective heat exchanger and increases heat input into the device, thereby increasing the temperature

bounds of the system ($T_{hex,h}$ and $T_{hex,c}$) and subsequent temperature difference across the p-n junction.

The effect of hot-side fluid temperature $T_{\infty,h}$ on $\eta_{th,max}$ and $P_{o,max}$ for the optimized and non-optimized cases is presented Fig. 12. For the represented case, A_N=10^{-7} m^2, L_N=0.5 mm, h_c=5, h_h=100 and h_{rad}=0.01 $Wm^{-2}K^{-1}$, $A_{eff_{c,h}}$=10^{-1} m^2. The $\eta_{th,max}$ values increase with an increasing $T_{\infty,h}$ up to a maxima at 378 °C for the optimized case and 386 °C for the non-optimized case, thereafter decreasing marginally. The maximum percent improvement of optimized compared to non-optimized geometry is 3.24% at a hot-side fluid temperature of 282 °C. The $P_{o,max}$ increases with increasing $T_{\infty,h}$ and the optimized geometry exhibits a marked improvement as compared to the non-optimized geometry when $T_{\infty,h}$ ≥100 °C. The optimized geometry exhibits continuing improvement in $P_{o,max}$ as compared to the non-optimized geometry until reaching a maximum of 10.36% at $T_{\infty,h}$=298 °C whereas it then decreases slightly.

2.4.4 Effect of Heat Exchanger Effective Area

Varying the heat exchanger effective area of the cold-side ($A_{eff,c}$) and hot-side ($A_{eff,h}$) heat exchangers, as seen in Fig. 13a and b, yields varying trends for $\eta_{th,max}$ and $P_{o,max}$, respectively. The cold- and hot-side convective and radiation heat transfer coefficients were kept invariant at h_c=5, h_h=100 and h_{rad}=0.01 $Wm^{-2}K^{-1}$, $T_{\infty,h}$ was invariant at 450 °C and A_N=10^{-7} m^2 and L_N=0.5 mm. Whether the $A_{eff,h}$ equals 10^{-3} or 10^{-1} m^2, for a given $A_{eff,c}$, $\eta_{th,max}$ remains invariant. Increasing $A_{eff,c}$ for a given $A_{eff,h}$ yields an asymptotically increasing trend in $\eta_{th,max}$ with values increasing by 15.5% for a two order of magnitude increase in $A_{eff,c}$ from 10^{-3} to 10^{-1} m^2. In comparison to the non-optimized geometry cases, once $A_{eff,c}$ exceeds $5{\cdot}10^{-3}$ m^2 there are marginal gains in $\eta_{th,max}$. For instance, $\eta_{th,max}$ increases by 1.64% and 3.05% for cases when $A_{eff,c}$=10^{-1} m^2 and $A_{eff,h}$=10^{-3} and 10^{-1} m^2, respectively.

The maximum power output exhibits a similar asymptotically increasing trend in $A_{eff,c}$ for a given $A_{eff,h}$ value with a two order of magnitude increase in $A_{eff,c}$ yielding a 23.6% increase in $P_{o,max}$ when $A_{eff,h}$=10^{-1} m^2 in comparison to 10^{-3} m^2. Increasing $A_{eff,h}$ two orders of magnitude has a minimal effect on $P_{o,max}$, with values increasing less than half a percentage

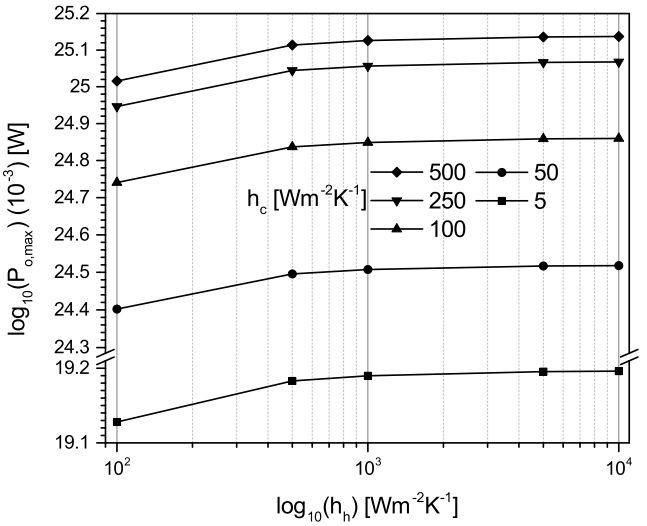

Figure 11: Effect of h_c on η_{max} and $P_{o,max}$ for optimized and non-optimized thermoelectric material geometries for the case when $A_{eff,c}$=$A_{eff,h}$=1E-3 m^2, h_{rad}=0.01 $Wm^{-2}K^{-1}$, ∄Π, L_N=0.5 mm, A_N=10^{-7} m^2, hot fluid temperature $T_{\inf,h}$=450 °C.

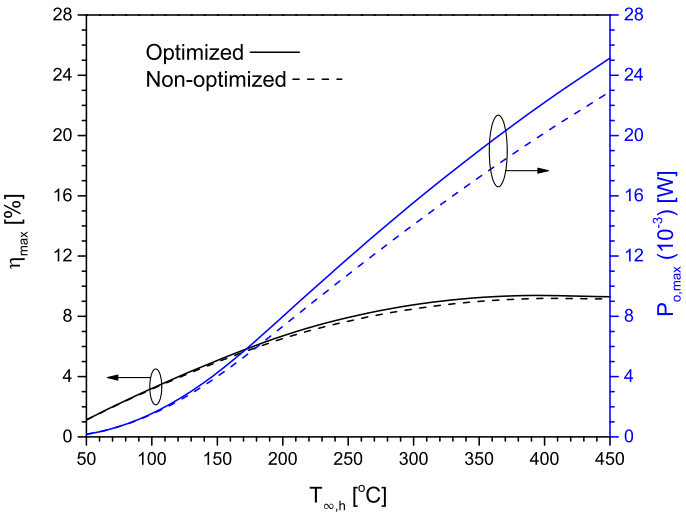

Figure 12: Effect of $T_{\infty,h}$ on $\eta_{th,max}$ and $P_{o,max}$ for the case when A_N=10^{-7} m^2, L_N=0.5 mm, h_c=5, h_h=10^2 and h_{rad}=0.01 Wm^{-2}K^{-1}, $A_{eff_{c,h}}$=10^{-1} m^2 and $\nexists\Pi$ for optimized and non-optimized geometries.

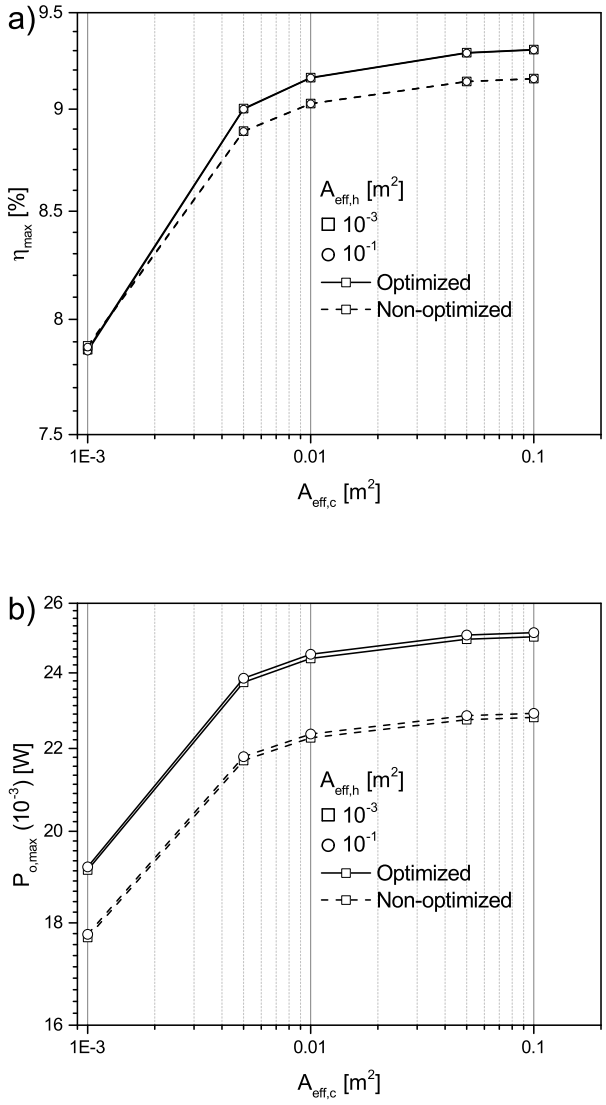

Figure 13: Effect of $A_{eff,c}$ and $A_{eff,h}$ on a) η_{max} and b) $P_{o,max}$ for the case when h_c=5, h_h=100 and h_{rad}=0.01 $Wm^{-2}K^{-1}$, $T_{\infty,h}$=450 °C, A_N=10^{-7} m^2, L_N=0.5 mm and ∄Π for optimized and non-optimized cases.

as $A_{eff,h}$ increase from 10^{-3} to 10^{-1} m^2. Comparing the optimized to non-optimized geometry, the gain in $P_{o,max}$ is more substantial than that of $\eta_{th,max}$. When $A_{eff,c}$ increase from 10^{-3} to 10^{-1} m^2, $P_{o,max}$ increases by 8.06% and 9.71% when $A_{eff,h}$=10^{-3} m^2 and 8.07% and 12.88% when $A_{eff,h}$=10^{-1} m^2. As compared to non-optimized geometry modeling [83, 136], $\eta_{th,max}$ and $P_{o,max}$ resolved via optimizing the geometry of the thermoelectric material are increased with higher-area heat exchangers.

2.4.5 Effect of Radiation Coefficient

Resolving radiation interaction within a three-dimensional thermoelectric device cavity is a computationally intensive process. For the purpose of analytical one-dimensional modeling, it is often more convenient to vary the radiation heat transfer coefficient h_{rad} (eqn. 2.40) over a range of values and determine its effect on performance. To see the effect of h_{rad}, the most extreme cases were considered; the cold- and hot-side heat transfer coefficients and heat exchanger effective areas were set at maximum values; 500 and 10^4 Wm^{-2}K^{-1} and 0.1 m^2, respectively. The hot-side fluid temperature was taken at the maximum of 450 °C and the interface material Π was omitted to maximize the temperature difference across the p-n junction and between the ceramic plates. To minimize conduction through the semiconductor, the thermoelectric leg length was selected such that L_N=10 cm and the smallest cross-sectional area was chosen such that A_N=10^{-7} m^2. The values of h_{rad} was varied between 0.01 and 20 Wm^{-2}K^{-1} and the effect of maximum thermal conversion efficiency η_{max} and maximum power output $P_{o,max}$ were determined.

Figure 14 illustrates the effect of h_{rad} on η_{max} and $P_{o,max}$. The results indicate a near-linear decrease in η_{max} and a slight exponential decay of $P_{o,max}$ with an increase in h_{rad}, respectively. As h_{rad} increase from 0.01 to 20 Wm^{-2}K^{-1}, $\eta_{th,max}$ decreases by 5.9% whereas $P_{o,max}$ decrease 16.9%. The decrease in $\eta_{th,max}$ and $P_{o,max}$ correspond to a decrease in temperature difference across and heat into the p-n junction due to an increase in heat being transferred via radiation. For instance, the temperature difference across the p-n junction for the case of maximizing $P_{o,max}$ decrease from a value of 235.90 °C for h_{rad}=0.01 Wm^{-2}K^{-1} to 226.72°C for h_{rad}=20 Wm^{-2}K^{-1}, corresponding to a 3.9% reduction in realized

temperature difference. Power output is proportional to the temperature difference across the p-n junction squared, thus a small reduction in ΔT results in an quadratic decrement in $P_{o,max}$. The efficiency, or power out per given heat input, does not decrease as substantially as does $P_{o,max}$. As the power output decreases exponentially with an increase in h_{rad}, the heat input decreases near-linearly. The competing effect of diminished power output per reduced heat input yields a near-linear decrease in $\eta_{th,max}$ per given h_{rad} values.

2.4.6 Thermal Resistance

It is evident that the thermal resistances associated with the hot-side ceramic plate and the greases between said ceramic and the hot-side heat exchanger and hot-side interconnector reduce the heat flow into the thermoelectric device. Additionally, the realizable temperature difference across the thermoelectric material is reduced by the presence of these materials, thereby decreasing device performance. Therefore, quantifying the amount of thermal resistance the hot-side ceramic and related greases contributing to the total thermal resistance of the thermoelectric device provides insight into potential gains in performance if device restructuring is pursued.

Assuming there are no interface materials ($\nexists\Pi$) thereby eliminating any thermal and electrical contact resistances, the effects of convective conditions, leg length and thermoelectric material cross-sectional area on the thermal resistances associated with the hot-side ceramic per total device thermal resistance can be studied. In reference to Fig. 3, we can denote the restrictive thermal resistance of the hot-side ceramic and associated greases as R_{res}=$R_{g,cer}$+$R_{Cer,h}$+$R_{g,int}$. Keeping the cold- and hot-fluid temperatures invariant at 25 °C and 450 °C, respectively, h_{rad}=0.01 Wm^2K^{-1}, the effects of thermoelectric element leg length, cross-sectional area and cold- and hot-side convective heat transfer coefficients and heat exchanger effective areas on the ratio of restrictive thermal resistance to total thermal resistance for non-optimized geometry cases are illustrated in Fig. 15a and b.

To study the effect of convective heat transfer coefficients and heat exchanger effective area, h=h_c=h_h was varied between 1 and 10^3 $Wm^{-2}K^{-1}$ and $A_{eff_{c,h}}$ between 10^{-5} and 10^{-1} m^2. For fixed values of A=A_N=A_P=10^{-7} m^2, h=100 $Wm^{-2}K^{-1}$ and L=0.5 mm, the ra-

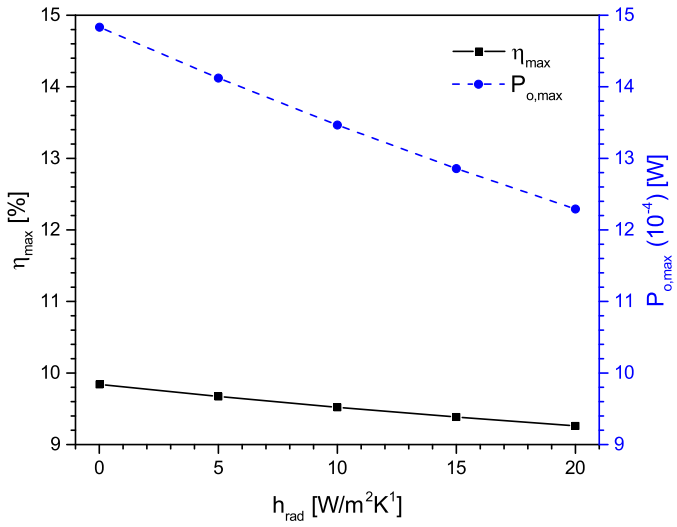

Figure 14: The effect h_{rad} on maximum thermal conversion efficiency η_{max} and maximum power output $P_{o,max}$ for a given cold- and hot-side convective heat transfer coefficients h_c=500 and h_h=10^4 $Wm^{-2}K^{-1}$, respectively, cold- and hot-side heat exchanger effective areas $A_{eff_{c,h}}$=10^{-1} m^2, thermoelectric element length L_N=10 mm and cross-sectional area A_N=10^{-7} m^2 and $\nexists\Pi$.

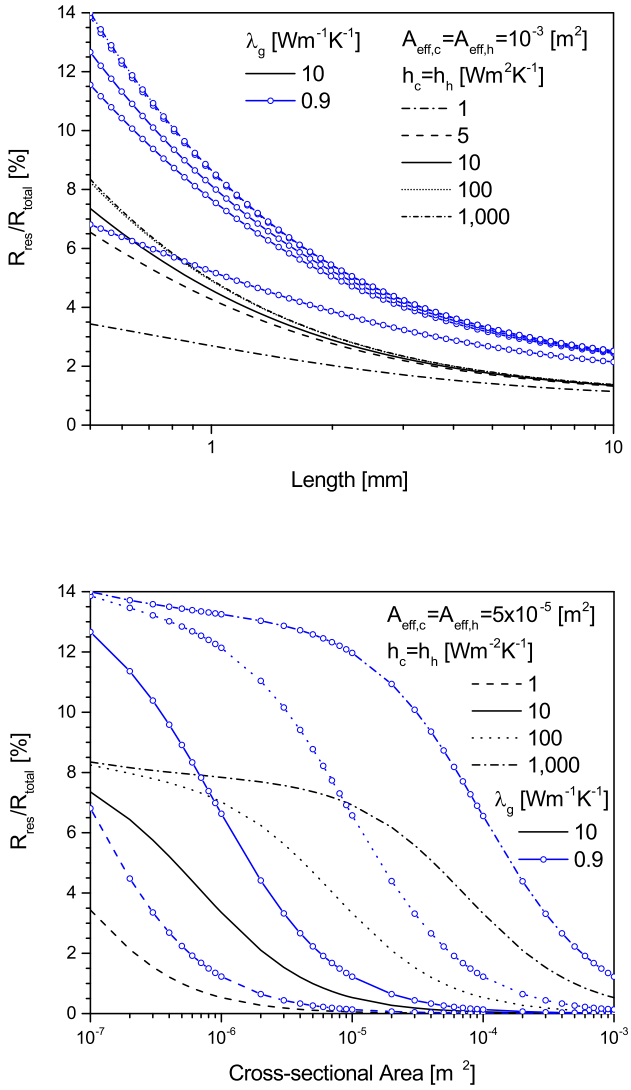

Figure 15: Effect of a) thermoelectric leg length and convective heat transfer coefficients on R_{res}/R_{total} and b) thermoelectirc material cross-sectional area and convective heat transfer coefficients on R_{res}/R_{total}.

tio of R_{res}/R_{total} increases from 3.43% to 8.34% as $A_{eff_{c,h}}$ increases from 10^{-5} to 10^{-1} m^2, respectively. The resistance associated with the heat exchangers, $R_{hex_{c,h}}$ (eqn.2.26) is proportional to inverse of the convective heat transfer coefficient times the effective area of the heat exchanger. Although $R_{hex_{c,h}}$ decreases with increasing $A_{eff_{c,h}}$, the increase in hot-side temperature and temperature difference across the ceramic decreases the materials thermal conductivity, increasing the thermal resistance associated with said material, thereby offsetting the decrease in R_{total}.

At higher h values above 100 $Wm^{-2}K^{-1}$, R_{res}/R_{total} increases only a tenth of a percent with increasing $A_{eff_{c,h}}$ values and remains around 8.36% when L=0.5 mm and exponentially decays to a value of 1.38% as L approaches 10 mm. As L increase, the ratio of R_{res}/R_{total} exponentially decreases due to an increase in R_N and R_P values. Keeping $A_{eff_{c,h}}$ invariant at 10^{-3} m^2, R_{res}/R_{total} increases with increasing h values and decreases with decreasing L. For maximizing power output of a thermoelectric generator, it is desirable to have short leg lengths (in reference to Fig. 4b), and the presence of R_{res} accounts for approximately 8% of the systems resistance under this set of applications.

Additionally, the effect of thermoelectric element cross-sectional area on R_{res}/R_{total} is able to be determined. The length L is kept invariant at 0.5 mm, the effective area of the heat exchangers are kept invariant at $A_{eff_{c,h}}$=10^{-3} m^2 while the convective heat transfer coefficients are varied between 1 and 10^3 $Wm^{-2}K^{-1}$, A is varied between 10^{-7} and 10^{-3} m^2 and λ_g is evaluated at 0.9 and 10 $Wm^{-1}K^{-1}$. Results as illustrated in Fig. 15b indicate that increasing the cross-sectional are of the thermoelectric elements non-linearly decreases R_{res}/R_{total}. With increasing cross-sectional area of the thermoelectric material, the thermal resistance associated with the material decreases (in reference to eqn. 2.33) thereby decreasing the total thermal resistance of the device. Due to the dependence of R_{res} on eqns. 2.28, 2.30 and 2.32, which in themselves have dependence on A as expressed in eqns. 2.27 and 2.29, increasing the thermoelectric material cross-sectional area also decreases R_{res}. Thus, R_{res}/R_{total} exhibits a non-linear decreasing trend with increasing thermoelectric material cross-sectional area. As seen in Fig. 15a, increasing h increases R_{res}/R_{total} due to the decrease in the ceramic's thermal conductivity with an increase in average temperature. Decreasing the thermal conductivity of the grease increases the R_{res}/R_{total} in a non-linear fashion. An order

of magnitude decreases in λ_g increases R_{res}/R_{total} between 67-99% for cases when A is taken as a minimum and h varies between 10^3 and 1 $Wm^{-2}K^{-1}$, respectively.

2.4.7 Validation

2.4.7.1 Numerical The results of the proposed analytical model have been compared to those obtained numerically and of other analytical models. The numerical modeling is described in detail [82] but will be described briefly in the following section. The system of partial differential equations governing thermoelectric phenomena under steady-state conditions for current flow continuity is expressed as

$$\nabla \cdot \mathbf{J} = 0. \tag{2.48}$$

The heat transport equation is expressed in eqn. 2.42. The electric potential is expressed by the non-Ohmic current-voltage relationship such that

$$\nabla V = \nabla V_{Ohm} + \nabla V_{Oc} = -\rho \mathbf{J} - \alpha \nabla T. \tag{2.49}$$

This expression, which is the summation of the Ohmic and Seebeck voltages produced from electric current and Seebeck effect via temperature gradient, accounts from the three-dimensionality of the phonemona. The boundary conditions associated with eqns. 2.42, 2.48 and 2.49 with respect to the geometry of a conventional thermoelectric device as depicted in Fig. 16 are described in the following.

The electric current density at the inlet terminal is expressed as

$$J|_{inlet} = \frac{1}{A_\xi} = \frac{V_{Oc}}{A_\xi (R_{in} + R_L)} \tag{2.50}$$

The temperature differential with respect to the unit normal direction at the inlet terminal is expressed as

$$\left.\frac{\delta T}{\delta \xi}\right|_{inlet} = 0. \tag{2.51}$$

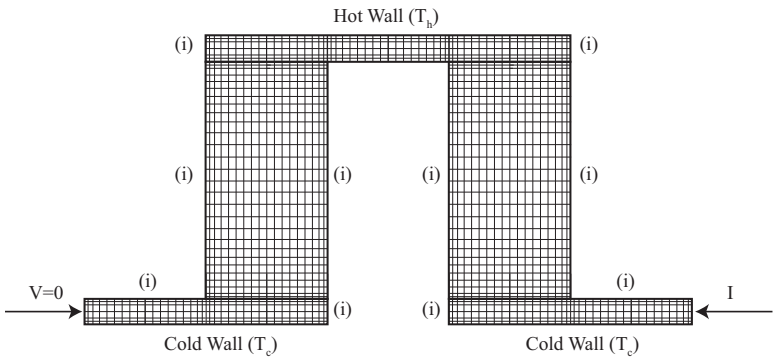

Figure 16: Schematic of mesh for numerical modeling of a conventional thermoelectric device

Within eqn. 2.50, the Seebeck voltage is a result of a temperature difference imposed across the p-n junction, evaluated at the cold-side interface of the semiconductor and interconnetor with reference to the hot-side interface, without any associated load resistance. Therefore, the second term in the second expression of eqn. 2.49 can be expressed as

$$V_{Oc} = \sum_{j=n,p} \sum_{i=1}^{2} \frac{L_j i}{A_{S_{ji}}} \int_{A_{S_{ji}}} |\alpha_{ji}| \frac{dT}{d\xi} dA_{S_{ji}}. \tag{2.52}$$

The term R_L in eqn. 2.50 represents the load resistance which matches the internal electrical resistance on the unicouple. The internal electrical resistance, which is the summation of all electrical resistances of the n- and p-type and interconnectors, is expressed as

$$R_{in} = \sum_{i=n,p,Cu} \frac{L_i}{A_i} \left[\frac{1}{V_i} \int_{V_i} \rho_i dV_i \right]. \tag{2.53}$$

The electric current density at the exit terminal is expressed as

$$V|_{exit} = 0. \tag{2.54}$$

The temperature differential with respect to the unit normal direction at the exit terminal is expressed as

$$\left. \frac{\delta T}{\delta \xi} \right|_{exit} = 0. \tag{2.55}$$

The temperature at the top and bottom interconnector surfaces is express as

$$T|_{Cu,h} = T_h, \quad T|_{Cu,c} = T_c. \tag{2.56}$$

The voltage at the top and bottom interconnector surfaces is expressed as

$$\left.\frac{\delta V}{\delta \xi}\right|_{Cu,h} = \left.\frac{\delta V}{\delta \xi}\right|_{Cu,h} = 0. \tag{2.57}$$

The remaining surfaces are exposed to convective and radiate heat transfer such that

$$q'' = h(T - T_\infty) + \epsilon\sigma(T^4 - T_\infty^4) \tag{2.58}$$

where copper has an emissivity of 0.03 and the bismuth telluride elements have an emissivity of 0.45. Continuity of temperature, current density and heat flux are imposed at the interface between interconnectors and thermoelectric elements such that

$$T_{Cu} = T_N = T_P, \mathbf{J}_{Cu} = \mathbf{J}_N = \mathbf{J}_P, -\frac{dT_{Cu}}{d\xi} = -\frac{\lambda_{N,P}}{d\xi}\frac{dT_{N,P}}{d\xi}. \tag{2.59}$$

The power output, heat input into the hot-side interconnector and efficiency of the unicouple are expressed as

$$P_o = I^2 R_L, \tag{2.60}$$

$$Q_h = -\int \lambda_{Cu}\frac{\Delta T}{\delta \xi} dA_S \tag{2.61}$$

and

$$\eta = \frac{P_o}{Q_h}. \tag{2.62}$$

Numerical modeling was done using ANSYS Fluent with the User-Defined Scalar environment allowing for thermo-fluid-electric coupling. Within Fluent, finite volume formulations of eqns. 2.48 and 2.49, constitutive relation of eqn. 2.50 and boundary conditions described by eqns. 2.50, 2.51, 2.54 and 2.55 were employed. The Ohmic heating, Peltier and Thomson effects were modeled as source terms in the energy equation (eqn. 2.42). The Seebeck

Table 3: Grid independence study for a conventional thermoelectric device with T_h=550 K, T_c=T_∞=300 K, L_N=L_P=10 mm, h=20 Wm^{-2} and R_L=1.15x10^{-2} Ω.

Cells	P_o [W]	Res.	Q_h [W]	Res.	η [%]	Res.
102,076	0.2007		3.4341		5.8443	
204,732	0.2008	0.0486	3.4371	0.0890	5.8420	0.5426
393,600	0.2007	0.0429	3.4360	0.0318	5.8413	0.0800
528,640	0.2007	0.0082	3.4362	0.0033	5.8407	0.0326

potential distributions as described by eqn. 2.49 were calculated by UDS fields. The spatial discretization of the diffusion term was done by a power law scheme. The electric current as provided by eqn. 2.50 is evaluated based upon the generated Seebeck voltage, as described by eqn. 2.52, generated by the temperature difference across the p-n junction for a given load resistance R_L.

The mesh was generated using Gambit 2.4, and various mesh sized models were created for a grid independence study. For the grid independence study, convergence criteria for the Ohmic and Seebeck potentials and energy were set to 10^{-10}, 10^{-10} and 10^{-12}, respectively. The grid sizes and residuals of select variables are presented in Table 3; the residual is defined as the absolute value of difference between new and previously calculated values, per previously calculated value, expressed in percentage. A grid size of 204,732 cells was chosen for simulations.

To compare the two models, operational parameters of the analytical model were chosen to match those prescribed across the p-n junction of the numerical mode. The thermal resistances associated with the heat exchangers, ceramic plate, greases and brazes were set to zero. The cross-sectional area of the n- and p-type materials was set to $2.5 \cdot 10^{-5}$ m^2 and the length of each element was fixed at 10 mm. The hot-side fluid temperature was varied between 350 K and 550 K (76.85 to 276.85 °C) while the cold-side fluid temperate was maintained at 300 K (26.85 °C). The geometry of the interconnectors were set at 5 mm

wide by 35 mm long by 1 mm thick. This was done to compare the values obtained by the analytical and numerical solutions. Then, the inclusion of the thermal resistance network was considered to show performance trends.

Comparing the effect of R_L on the produced current I and Ohmic voltage V_{Ohm} between the two models yields good agreement as seen in Fig. 17a and b. With an increase in $T_{\infty,h}$ there is a non-linear increase in I and V_{Ohm} due to an increase in the generation of V_{Oc}. Increasing R_L non-linearly diminishes I and V_{Ohm}. The proposed analytical model agrees well with the presented numerical data for both I and V_{Ohm} predictions as a function of R_L for various $T_{\infty,h}$ values.

Comparing the effect of R_L on $P_{o,max}$, Q_h and η_{max} between the two models yields good agreement as seen in Fig. 18a-c. The hot-side fluid temperature was held invariant at $T_{\infty,h}$=450 K. As seen with the numerical and analtyical cases, η_{max} and $P_{o,max}$ increase with an increase in R_L until the maxima when R_L=R_{in} and then decrease once R_L exceeds R_{in}.

2.4.7.2 Analtyical A comparison to another analytical model [85] is presented in Fig. 19. Within the comparing model, the hot-surface temperature was varied between 310 and 550 K while the cold-surface temperature was kept invariant at 300 K. The element geometries were kept invariant at W_N=W_P=5 mm and L_N=L_P=20 mm with the load resistance equaling the internal resistance. To mimic the same operating conditions but yet including the thermal resistance network, the geometries of the thermoelectric legs were kept as stated but the cold- and hot-side operating conditions were set to h_c=500, h_h=10^4 and h_{rad}=0.01 $\mathrm{Wm^{-2}K^{-1}}$, respectively, $A_{eff_{c,h}}$=10^{-1} $\mathrm{m^2}$ and R_{el}=R_{th}=0. Results indicate that P_o and η follow the same trends with an increase in $T_{\infty,h}$ with good agreement between values. The optimized and non-optimized models show a decrease in $P_{o,max}$ and η_{max} with an increase in $T_{\infty,h}$ due to the inclusion of the thermal resistance network and diminished ΔT across the p-n junction.

Additionally, the effect of contact resistances, in particular thermal and electrical, on the performance of a conventional thermoelectric device, have previously been studied [83] and serve as a basis of comparison. The previous work studied the effect of hot- and cold-side convective heat transfer coefficients, thermal and electrical contacts on the power output of a conventional thermoelectric device with geometry of L=3 mm and W= 5 mm. The

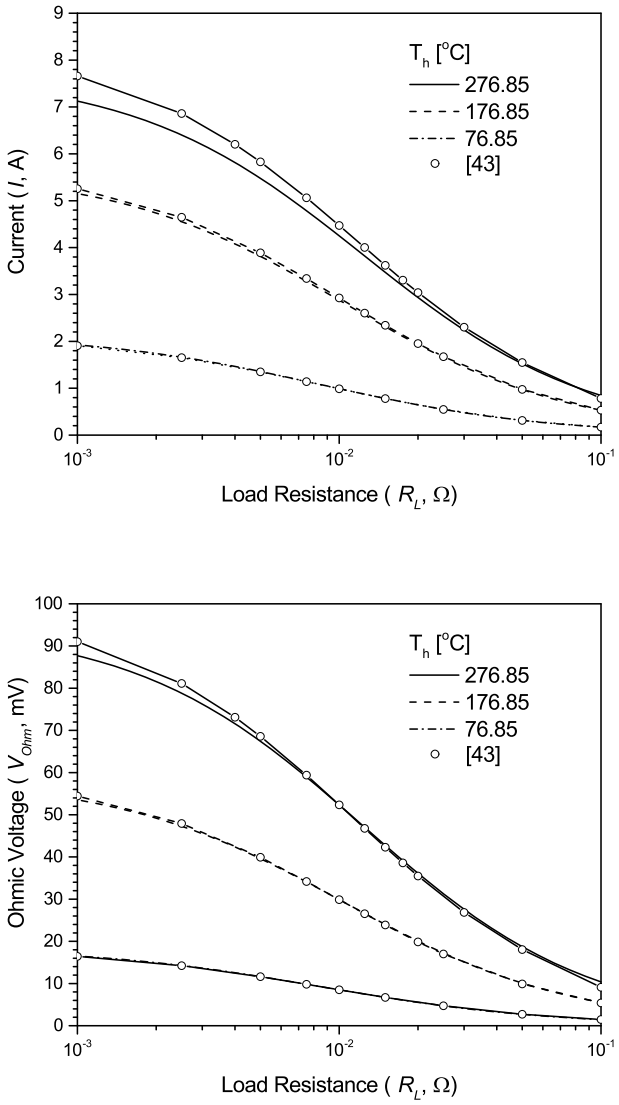

Figure 17: Comparison between published numerical data [82] and proposed analytical model for various $T_{\infty,h}$ for a) produced current and b) Ohmic voltage.

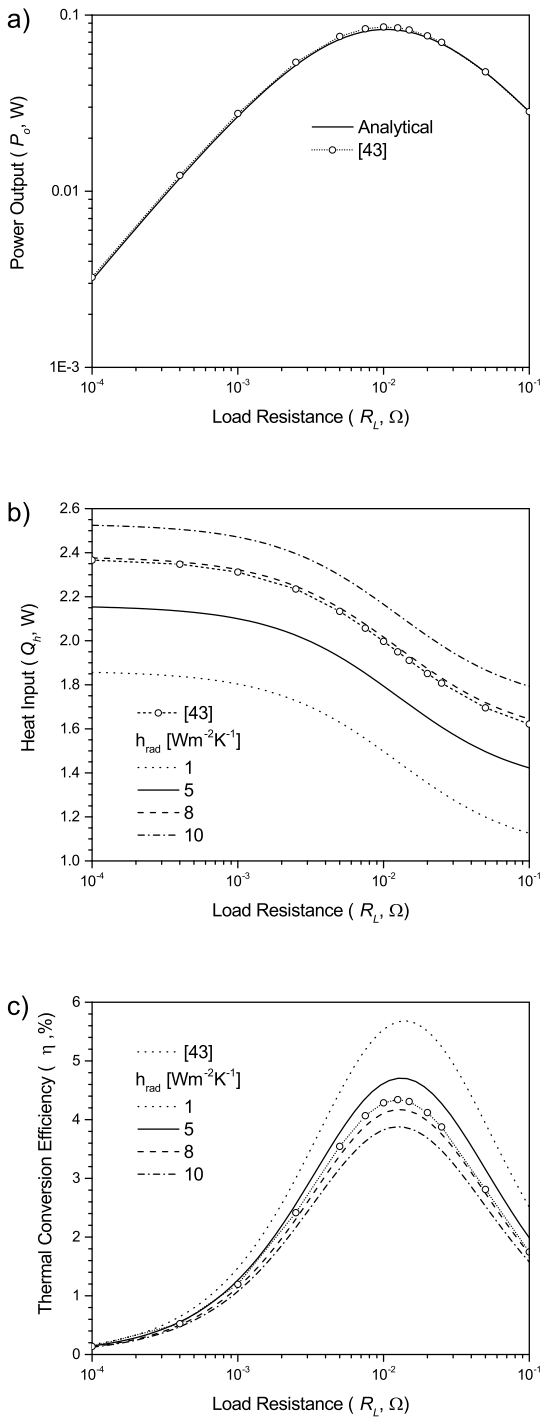

Figure 18: Comparison between published numerical data [82] and proposed analytical model for a) power output, b) heat input and c) thermal conversion efficiency.

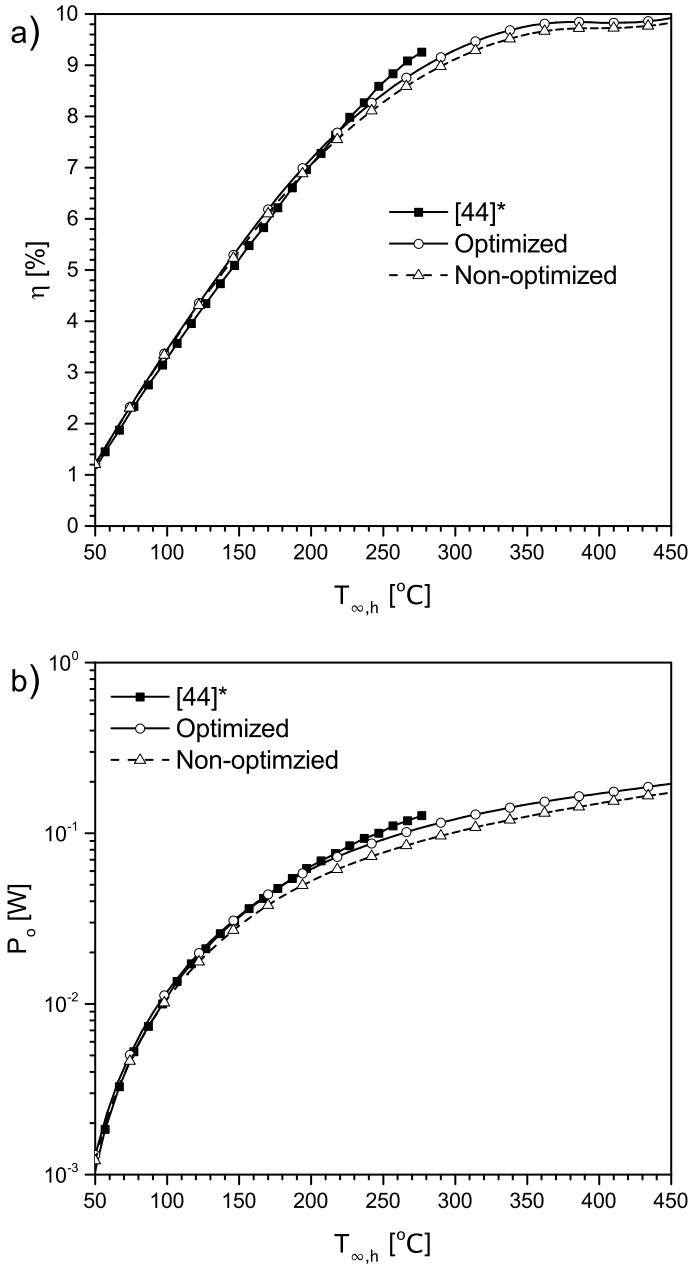

Figure 19: Comparison of η and P_o between presented and published data [85]

aforementioned model also includes the effect of Joule heating within the interconenctor; the present model neglects the effects of Joule heating within the interconnector due to the three-order of magnitude lesser difference in electrical resistivity of a copper interconnector in comparison to the bismuth-telluride semiconductors. To mimic operating conditions, the hot- and cold-side convective heat transfer coefficients were varied between 10^3 and 10^5 $Wm^{-2}K^{-1}$, the geometry was assumed to be non-optimized (L_N=L_P= 3 mm and A_N=A_P=25 mm^2), the radiation heat transfer coefficient was set to a minimum (0.01 $Wm^{-2}K^{-1}$), the effective areas of the hot- and cold-side heat exchangers were kept constant at $6.85{\cdot}10^{-5}$ m^2 and the hot and cold fluid temperatures were kept invariant at 450 K and 300 K, respectively.

Comparing the effect of thermal contact resistance on the power output of a unicouple in comparison to previously published date [83], we obtain similar trends in $P_{o,max}$ with increasing R_{th} and h values for a fixed R_{el} value of 10^{-8} Ωm^2 as illustrated in Fig. 20a. The maximum power output decreases non-linearly with an increase in R_{th} due to a decrease in temperature difference across the n- and p-type thermoelectric materials, results in lesser generated Seebeck voltage and subsequently produced current. The presented model is in good agreement with previously published data, even considering the differences in model assumptions. As the heat transfer coefficients increase, the P_{max} values evaluated at the lowest R_{th} value nonlinearly increase. As see within the published model, an increase in h from 10^3 to 10^4 and 10^4 to 10^5 results in an increase in $P_{o,max}$ of 131.1% and 11.2%, respectively. Similary, in the presented model, the same increases in h results in an increase in $P_{o,max}$ by 124.0% and 10.5%, yielding good agreement between the two models with difference in predicted $P_{o,max}$ values evaluated at the lowest R_{th} values of 1.7%, 7.1% and 8.4% for h values of 10^3, 10^4 and 10^5 $Wm^2K^{-1}K$, respectively. Comparing the effect of electrical contact resistance on the power output of a unicouple with the same geometry and fluid operating conditions as stated previously [83], we obtain similar trends in $P_{o,max}$ with increasing R_{el} and h values for a fixed R_{th} value of $5{\cdot}10^{-6}$ Km^2W^{-1} as illustrated in Fig. 20b. The value of $P_{o,max}$ decreases non-linearly with an increase in R_{el}. As R_{el} increases, the amount of Joule heat at the contacts increases, thereby reducing the temperature difference across the p- and n-type material and subsequently reducing the produced Seebeck voltage and current. The power output, which is proportional to the current generated squared

times the unicouple electrical resistance, then exhibits a non-linear decrease with an increase in R_{el}. As the heat transfer coefficients increase, a larger temperature difference is able to be maintained across the thermoelectric elements for a constant R_{el}, thereby increasing the Seebeck voltage, produced current and subsequent power output. Comparing the present data to published, increasing h from 10^3 to 10^4 and 10^4 to 10^5 results in a 119.3% and 10.1%, and 131.1% and 11.2% increase in $P_{o,max}$ for a R_{el} value of 10^{-12} Ωm^2, respectively. This indicates good agreement in predicted $P_{o,max}$ values for given R_{el} and h values, with the percent difference in $P_{o,max}$ predictions being 4.5%, 0.83% and 1.6% for h values of 10^3, 10^4 and 10^5 $Wm^{-2}K^{-1}$, respectively.

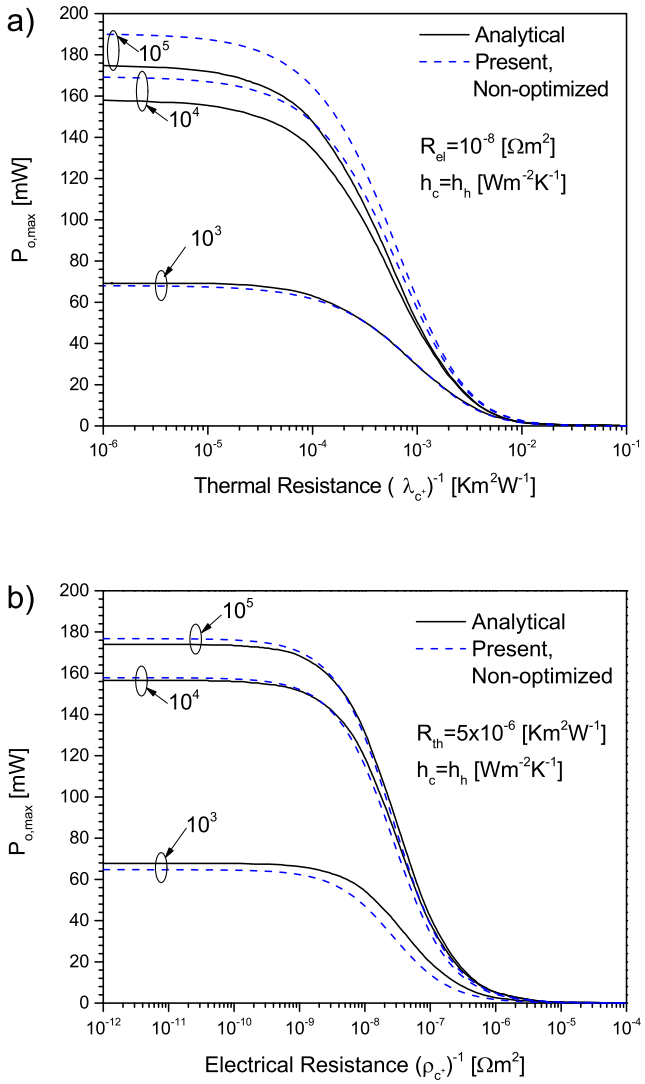

Figure 20: Comparison between published analytical data [83] and proposed analytical model for a) power output versus thermal contact resistance and convective heat transfer coefficients and b) power output versus electrical contact resistance and convective heat transfer coefficients.

2.5 CONCLUSIONS

Within Chap. 2, a complete one dimensional thermal resistance network coupled with a co-optimization algorithm that simultaneously optimized thermoelectric leg length and cross-sectional area to maximize thermal conversion efficiency $\eta_{th,max}$ and maximum power output $P_{o,max}$ was introduced. The co-optimization algorithm included provisions to incorporate thermal and electrical contact resistances associated with interface material Π between the thermoelectric materials and interconnectors. The key findings are summarized as follows:

1. It is shown that the effect of geometry, i.e. leg length and cross-sectional area, play an important role in $\eta_{th,max}$ and $P_{o,max}$ predictions; $P_{o,max}$ non-linearly diminishes with an increase in leg length whereas $\eta_{th,max}$ asymptotically increase in leg length. Increasing the cold-side heat transfer coefficients h_c non-linearly and asymptotically increases both $\eta_{th,max}$ and $P_{o,max}$ values for a given leg length. The optimized geometry, excluding Π, yielded an increase in $\eta_{th,max}$ and $P_{o,max}$ of 1.51% and 9.7% in comparison to non-optimized geometries. It is also shown there exists an optimum cross-sectional area that maximizes $\eta_{th,max}$ and $P_{o,max}$ for given h_c, hot-side convective heat transfer coefficient h_h, hot-side fluid temperature $T_{\infty,h}$ and leg length. To maximize $\eta_{th,max}$, a smaller cross-sectional area is desired; as h_c increases, the cross-sectional area is able to be increased to maintain a maximum $\eta_{th,max}$ value. To maximize $P_{o,max}$, there exists a cross-sectional area that is not a minimum of area, but rather a function of h_c and h_h.
2. The inclusion of thermal and electrical contact resistances, $\lambda_{c^+}^{-1}$ and ρ_{c^+}, respectively, allowed for more accurate modeling of the thermoelectric unicouple. The optimized geometry case indicated substantial gains in $P_{o,max}$ and $\eta_{th,max}$ in comparison to the non-optimized geometry case. Although both modeling techniques indicate that $P_{o,max}$ non-linearly and drastically decreases with increasing $\lambda_{c^+}^{-1}$ and ρ_{c^+} values, the optimized geometry case achieved 28.9% greater $P_{o,max}$ values in comparison to non-optimized geometry cases for high h values and low λ_{c^+}. Additionally, the optimized geometry exhibited consistently higher power density values for all $\lambda_{c^+}^{-1}$ and ρ_{c^+} values in comparison to non-optimized cases. The optimize geometry achieved a marginal increase in $\eta_{th,max}$ on the order of one percent in comparison to the non-optimized geometry but exhibited

increases in volumetric efficiency on the order of 10-20% in comparison to the non-optimized geometries for all convective heat transfer coefficient and resistance values.

3. Operational parameters such as h_c and h_h values and $T_{\infty,h}$ were studied and their effect on $P_{o,max}$ and $\eta_{th,max}$ were presented. Predictions of $\eta_{th,max}$ indicate asymptotically increasing values with increasing h_c and h_h values with no substantial change in value when h_c and h_h both exceed 100 $Wm^{-2}K^{-1}$; geometric optimization yields no more than 1.3% improvement over non-optimized geometries. Predictions of $P_{o,max}$ indicate similary asymptotically increasing values with increase h_c and h_h values, however $P_{o,max}$ begins to plateau when h_c exceeds 250 $Wm^{-2}K^{-1}$ and h_h exceeds 500 $Wm^{-2}K^{-1}$. Likewise, geometric optimization indicates an increase in $P_{o,max}$ of 9.7% in comparison to non-optimized cases for large h_c and h_h values. Lastly, increasing $T_{\infty,h}$ for fixed $A_{eff_{c,h}}$, h_c and h_c values with a fixed cold side temperature $T_{\infty,c}$ yields a non-linear increase in $\eta_{th,max}$ that plateaus at 378 °C and 378 °C for the optimized and non-optimized cases, with the optimized geometry achieving a maximum 3.24% increase in comparison to the non-optimized cases at $T_{\infty,h}$=282 °C. With increasing $T_{\infty,h}$, $P_{o,max}$ increases near linearly, with the optimized geometry achieving a maximum improvement of 10.36% over the non-optimized geometry at 298 °C.

4. Geometric parameters such as cold- and hot-side heat exchanger effective areas $A_{eff,c}$ and $A_{eff,h}$, respectively, were studied and their effect on $P_{o,max}$ and $\eta_{th,max}$ were quantified. Increasing $A_{eff,c}$ for a fixed $A_{eff,h}$ value asymptotically increases $\eta_{th,max}$, whereas for a fixed $A_{eff,c}$, increasing $A_{eff,h}$ yielded no significant gains in $\eta_{th,max}$. Additionally, geometric optimization yielded an improvement of 3.05% in $\eta_{th,max}$ in comparison to non-optimized geometries for studied conditions. Predictions of $P_{o,max}$ followed similar asymptotically increasing trends with increasing $A_{eff,c}$ for a fixed $A_{eff,h}$, however increasing $A_{eff,h}$ for a fixed $A_{eff,c}$ did yield a slight increase in values. Furthermore, the optimized geometry exhibited greater $P_{o,max}$ in comparison to non-optimized geometries for studied conditions, with a maximum improvement of 12.88% when $A_{eff,c}$ and $A_{eff,h}$ were taken at maximum values.

5. By varying the radiation heat transfer coefficient h_{rad} from 0.01 to 20 $Wm^{-2}K^{-1}$ while keeping all geometric and operational parameters constant, the effect on $P_{o,max}$ and

$\eta_{th,max}$ was then investigated. Increasing values of h_{rad} from minimum to maximum values near-linearly decreased $eta_{th,max}$ values by 5.9% and non-linearly decreased $P_{o,max}$ values by 16.9%, indicating substantial sensitivity to performance predictions. This key point is the basis of Chap. 3, in which the radiation view factor is resolved and radiation heat transfer is properly modeled within the thermoelectric device cavity.

6. The contribution of the restrictive hot-side ceramic and grease that affixes the hot-side heat exchanger and hot-side interconnector to said ceramic, denoted as R_{res}, to the total system thermal resistance, denoted as R_{total}, per geometric prescriptions and operational parameters was investigated. With decreasing thermoelectric leg length and increasing h_c and h_h values, the ratio of R_{res} to R_{total} exponentially and asymptotically increases, respectively, reaching a maximum value of 14%. With a decrease in cross-sectional area and increasing h_c and h_h values, R_{res} to R_{total} non-linearly increases, plateauing to a maximum of 14%. Although R_{res} accounts for only a small percentage of the total system thermal resistance, the elimination of of these components and the associated thermal resistance would allow for the establishment of a larger temperature difference across the unicouple junction and for a greater heat input. This concept is the premise of Chaps. 4 and 5, which experimentally investigate the performance of two integrated thermoelectric devices.

7. Lastly, the proposed analytical model was compared to published numerical and analytical models. For specified geometry and operational parameters, predictions of current, Ohmic voltage, power output, heat input and thermal conversion efficiency as a function of load resistance R_L agree with published the literature [82], with the only deviation of results being a function of h_{rad}. Per operating conditions and prescribed geometry, the proposed model was compared to two similar analytical models. The thermal conversion efficiency and power output as functions of $T_{\infty,h}$ were found to be in good agreement [85] with a maximum difference in predicted values of 8.4%. Comparing power output versus R_{th} and R_{el} yielded good agreement [83] with a maximum difference in predicted values of 8.3%.

3.0 ON THE NUMERICAL COMPUTATION OF RADIATION VIEW FACTORS WITHIN CONVENTIONAL THERMOELECTRIC DEVICES

Device design and analysis is an important aspect in achieving high thermal conversion efficiency or power output; in particular, maximizing the temperature difference across the hot and cold junctions per given operating conditions. To properly analyze TEGs, analytical and numerical modeling must account for radiation heat transfer between participating surfaces within the TEG cavity, as illustrated in Chap. 2, Sec. 2.4.5. Before the method of resolving the radiation view factors within thermoelectric device cavity is introduced, a brief review of literature directly related to this chapter, of which was not included in Chap. 1, will be provided.

Analytical and numerical modeling methods have been proposed to study the effects of radiation heat transfer within a TEG. Analytical modeling requires the resolution of radiation view factors within complex three-dimensional TEG cavities. Meng et al. [138] studied the performance of TEG using a one-dimensional thermal resistance network, including the effects of convection and radiation within the gap cavity. However, their radiation formulation was over-simplified in assuming that radiation heat transfer with a TEG is analogous to infinitely long parallel plates. Crane et al. [65] used an average emissivity to predict the radiation heat transfer with a TEG and simplified the view factor calculations due to the complexity of the geometry. Kraemer et al. [139] used an equivalent area of thermoelectric material, and assumed the heat transfer between elements is negligible due to similar surface temperatures and high packing densities and relied on the net radiation method proposed by Modest [140].

Numerical modeling can be used to resolve radiation view factors. Zhu et al. [141] used Fluent to parametrically study the effect of rod shape, geometry and spacing on the radia-

tive and convective heat transfer within a cavity, without taking into account actual TEG geometry, the effects of interconnectors and non-linear surface temperature distributions of the TE legs. Chen at al. [142] proposed an numerical model for TEGs validated with Ansys and experiments, although the model excluded convection or radiation from the legs and ceramics or interconenctor geometry.

Of the numerical models proposed, a common solution is to either impose a numerical value on the radiation heat transfer coefficient h_r, or lump the convective and radiative heat transfer coefficients together as h_s and them impose a value. These approach lack physical significance of the effects of geometry on convection and radiation within the TEG cavity. Reddy et al. [88] varied h_s between 0 and 20 $\mathrm{Wm^{-2}K^{-1}}$ to reflect varying conditions. Chen et al. [143] used Fluent's user defined function/scalar package to investigate three-dimensional effects of conduction, convection and radiation of a TEG; their assumptions simplified the convective and radiative heat transfer into one lumped value. Wang et al. [144] developed a three-dimensional numerical model of a TEG, but also lumped the convective and radiative heat transfer coefficients into one term varying h from 0 to 200 $\mathrm{Wm^{-2}K^{-1}}$. Völklein et al. [145] assumed a small difference in temperature between the legs and ambient, and imposed h_s=100 $\mathrm{Wm^{-2}K^{-1}}$. Huang et al. [146] proposed a one-dimensional analysis on a TEC which linearized the radiation heat transfer rate due to a small realized temperature difference between surface of the thermoelectric materials and ambient gas, which resulted in h_r=50 $\mathrm{Wm^{-2}K^{-1}}$, which was assumed reasonable. Cheng et al. [147] also varied the lumped convective and radiative heat transfer coefficient of the p- and n-type legs from 5-15 $\mathrm{Wm^{-2}K^{-1}}$.

Two noteworthy studies resolved radiation heat transfer. Ziolkowski et al. [148] used a FEM method to model TEGs, including convection and radiation from interior surfaces (pellets and interconnectors, excluding ceramic plates), with the latter being resolved using the radiation matrix method (a built-in feature of Ansys). Their results indicate that increasing leg height reduced radiation heat flow but efficiency decreased as compared to shorter legs due to dissipative heat flow from increased thermal resistance. Suter et al. [149] experimentally and numerically investigated the performance of a TEG for solar applications, modeling conduction, convection and radiation within the device using a finite volume method. The

radiation heat transfer was modeled within the TEG cavity using enclosure theory, taking into account the surfaces of the ceramic and thermoelectric materials. Results indicated that radiation heat transfer is not dominant within the cavity for the given operating conditions.

It is evident from the limited literature, there exists a need to quantify the radiation view factor within TEG cavities. The proposed solution is to numerically solve for F_{ij} between the two primary participating surfaces based upon emissivity values; the cold- and hot-side ceramic plates. This study addresses the method and solution of resolving F_{ij} for various TEG geometries; various height to width ratios of thermoelectric legs, interconnector thicknesses and packing densities. The results provide data and trends which will facilitate in the development of more accurate and realistic analytical and numerical models.

3.1 METHODOLOGY

An in-house numerical code was developed to resolve the calculation of F_{ij} within a unit cell of a thermoelectric device using C++ and later implemented in Java with Aparapi to utilize hybrid CPU-GPU computing. The model resolved F_{ij} for various configurations, which reflected varying height to width ratio of the thermoelectric materials, interconnector thicknesses and packing densities of possible TEG designs. The packing density θ is defined as the ratio of the total cross-sectional area of the p- and n-type element legs (A_P and A_N, respectively) to the cross-sectional area of the thermoelectric (A_m) device [136] such that

$$\theta = \frac{N(A_P + A_N)}{A_m} \tag{3.1}$$

where N represents the total number of junctions; for a unit cell N=1. A higher packing density means the element legs are closer together, reducing the gap width W_g between legs. The gap width is expressed as

$$W_g = \sqrt{\frac{W^2}{\theta}} - W. \tag{3.2}$$

The term W in eqn. 3.2 is the width of the n-type and p-type materials and implies they are equal (W=W_N=W_P). Figure 21 depicts a unit cell of interest within the TED.

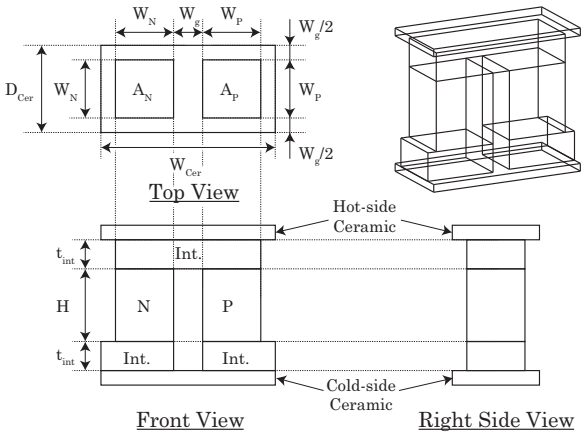

Figure 21: Configuration of a thermoelectric generator unicouple per unit cell.

The packing density for a unit cell can be expressed in terms of the p- and n-type element widths (W_P and W_N, respectively) and subsequent areas (A_P=W_P^2 and A_N=W_N^2) and the gap width such that

$$\theta = \begin{cases} \dfrac{A_N + A_P}{A_N + 2 \cdot W_g^2 + 3 \cdot W_g \cdot W_N + W_P \cdot (W_N + W_g)} & W_N > W_P \\ \dfrac{A_N + A_P}{A_P + 2 \cdot W_g^2 + 3 \cdot W_g \cdot W_P + W_N \cdot (W_P + W_g)} & W_P > W_N \\ \dfrac{2 \cdot W^2}{2 \cdot W^2 + 4 \cdot W_g \cdot W + 2 \cdot W_g^2} & W_N = W_P = W. \end{cases} \tag{3.3}$$

The area of the interconnector A_{int} in contact with a ceramic surface is expressed as

$$A_{int} = \begin{cases} W_N \cdot (W_N + W_g + W_P) & W_N > W_P \\ W_P \cdot (W_N + W_g + W_P) & W_P > W_N \\ W \cdot (2W + W_g) & W_N = W_P = W. \end{cases} \tag{3.4}$$

The top and bottom interconnectors are assumed to be the same thickness and width, which is based upon the maximum width of the n- or p-type material. Table 4 lists the emissivity of each material within a typical TEG and the temperature range for which these values are applicable. For this study, it is assumed W_N=W_P and the radiation view factor

between the primary participating surfaces, the top and bottom ceramic plates, which have high emissivity values and experience the largest temperature difference, are resolved.

Table 4: Emissivity of common materials within a TEG. Citations: *[150], †[151], ‡[152] and § [153]

Material	Emissivity	Temperature
Copper	0.03-0.04*	26-726°C
Alumina	0.58†	100°C
	0.69-0.41*	326-1,126°C
	0.56‡	900-1,400°C
N- and P-type Bi_2Te_3	0.66§	25°C

3.1.1 Numerical Solution

To compute the view factors, a unit cell within the TEG was considered. The view factor is defined as the radiation leaving an emitting surface i which is absorbed by another surface j, expressed as

$$F_{ij} = \frac{1}{A_i} \int_{A_i} \int_{A_j} \frac{cos\phi_i cos\phi_j}{\pi \overrightarrow{R}^2} dA_i dA_j \tag{3.5}$$

where A_i is the area of surface i, A_j that of j, $\overrightarrow{R}$ is the vector connecting the centroids of surfaces A_i and A_j and ϕ_i and ϕ_j the polar angles between the vector $\overrightarrow{R}$ and the unit normal vectors of surface i and j, respectively.

The polar angle ϕ is expressed as

$$cos\phi_i = \frac{\overrightarrow{n_i} \cdot \overrightarrow{R}}{\| \overrightarrow{n_i} \| \, \| \overrightarrow{R} \|} \tag{3.6}$$

where $\overrightarrow{n_i}$ is the unit normal vector from surface i. The same expression holds for surface j. The geometry of a simple interaction between two parallel plates is illustrated in Fig. 22.

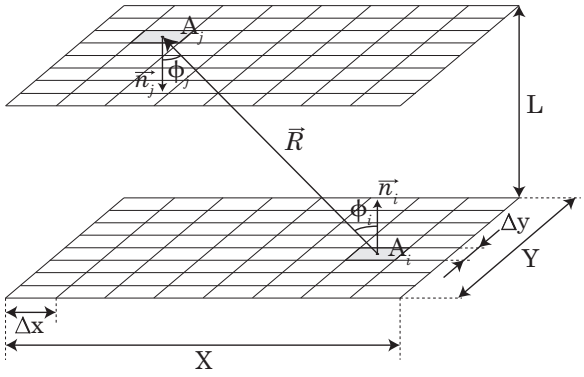

Figure 22: Schematic of differential areas of parallel and perpendicular plates used for view factor calculation.

The net radiation heat transfer rate between two interacting surfaces is expressed as

$$Q_i = \sum_{j=1}^{N} \epsilon \sigma A_i F_{ij} (T_i^4 - T_j^4) \tag{3.7}$$

where σ represents the Stefan-Boltzmann constant and ϵ is the emissivity of the material.

3.1.1.1 Shadow Effect The shadow effect is considered when the net radiation heat transfer between two participating surfaces is reduced due to interference by another surface. For example, the p- and n-type legs, as well as the top and bottom interconnectors, block certain instances of $\overrightarrow{R}$, reducing the net radiation heat transfer between the top and bottom ceramic plates.

The interior three-dimensional geometries were represented using a set of surface polygons. For each ray $\overrightarrow{R}$ between two differential areas, the avoidance or intersection of $\overrightarrow{R}$ with each of the polygons was determined via a point-in-polygon algorithm [154, 155]. If $\overrightarrow{R}$ intersects an even number of polygon edges, the point is outside the polygon and that instance of F_{ij} is summed; if the projected vector intersects an odd number of polygon edges, then the point is inside the polygon and that instance of F_{ij} equals zero.

To resolve a large number of $\overrightarrow{R}$ and the subsequent point-in-polygon algorithms, hybrid CPU-GPU computing was utilized. The benefit of hybridized computing is that graphics cards with thousands of cores are able to efficiently execute simple vector operations, such as ray tracing, on massively parallel data sets, speeding up computations orders of magnitude. Since each $\overrightarrow{R}$ for a given differential area of the emitting surface is independent of all other differential areas of the emitting surface, the problem is inherently massively parallelizable and thus a suitable candidate for CPU-GPU computing.

3.2 RESULTS AND DISCUSSION

3.2.1 Numerical Modeling

The numerically calculated view factors were compared to those determined by analytical expressions to confirm the solution methodology. The two participating surfaces were divided into rectangles with an x- and y-length of Δx and Δy, respectively, yielding areas A_i and A_j as represented in Fig. 22. The percent error was found by comparing the analytic solutions of the parallel plate view factor to those computed numerically. The analytic solution for the view factor F_{ij} for aligned parallel plates i and j is expressed as [156]

$$F_{ij} = \frac{2}{\pi \overline{X}\overline{Y}} \left(ln \left[\frac{(1+\overline{X}^2)(1+\overline{Y}^2)}{(1+\overline{X}^2+\overline{Y}^2)} \right]^{\frac{1}{2}} + \overline{X}(1+\overline{Y}^2)^{\frac{1}{2}} tan^{-1} \frac{\overline{X}}{(1+\overline{Y}^2)^{\frac{1}{2}}} + \overline{Y}(1+\overline{X}^2)^{\frac{1}{2}} tan^{-1} \frac{\overline{Y}}{(1+\overline{X}^2)^{\frac{1}{2}}} - \overline{X} tan^{-1} \overline{X} - \overline{Y} tan^{-1} \overline{Y} \right) \tag{3.8}$$

where $\overline{X}$ and $\overline{Y}$ are the length and width of the bottom plate divided by the distance between the plates L, respectively. The numerical results as computed in C++ are compared against the analytical in graphical form, as seen in Fig. 23 as provided by Incropera [150]. The percent error versus Δx for a select case is shown Fig. 24.

The results of the calculated view factor between the top and bottom ceramic plates of a unit cell TEG for various packing densities ($0.1 \leq \theta \leq 0.9$), height to width ratios ($0.5 \leq$

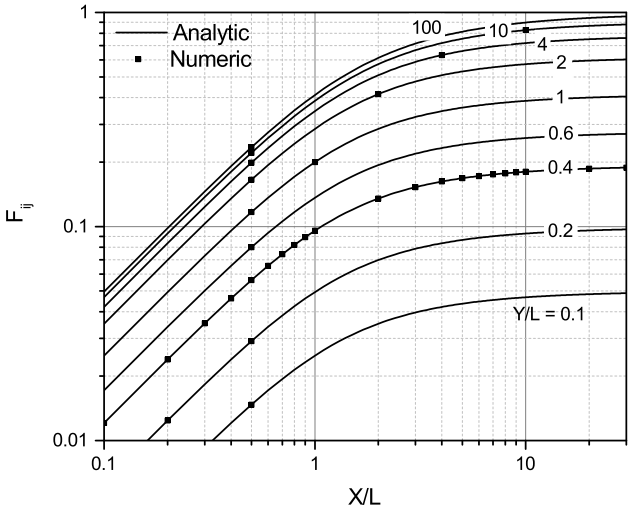

Figure 23: Comparison of numerical solution for various X/L and Y/L values compared to the analytical solutions of Howell [156] represented by Incropera [150].

H/W ≤1.75) and top and bottom interconnector thicknesses (0.125 ≤ t_{int} mm≤ 0.25) are presented in Tab. 5. It is noted W is held invariant at 1 mm while H is varied between 0.5 and 1.75 mm. Graphical representations of the trend of data is presented in Fig. 25a-e. A grid independence study was conducted for cases representing extrema of geometric conditions and is presented in Tab. 6. A grid size of 2,560x2,560 differential areas per top and bottom ceramic plate was chosen which resulted in residuals less than 1E-3.

The hybridized CPU-GPU code developed in Java with Aparapi was compared with the results calculated by the code using C++, that latter being validated with the analytical results of F_{ij} between two parallel plates, for select cases. The difference of values between languages is presented in Tab. 7, confirming no deviation of results. Additionally, performance gains using hybridized CPU-GPU computing were determined. To execute the code in C++ to analyze the case where θ=0.1, H/W=0.5 and t_{int}=0.125 mm on a 160x160 grid, four physical cores required 384.66 seconds to complete the calculation. Using a 1,028 core

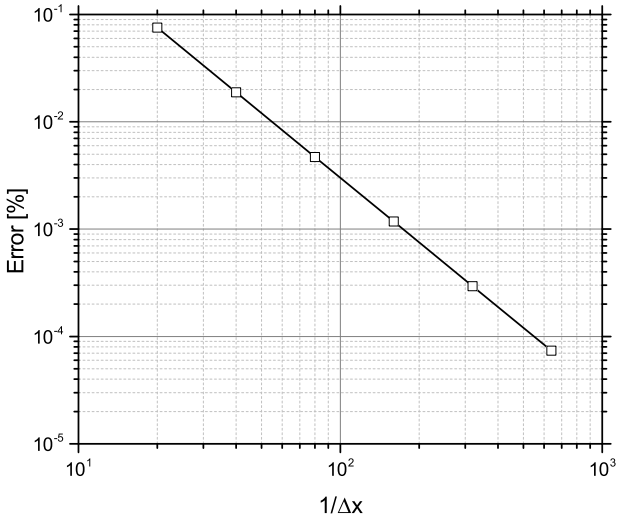

Figure 24: Percent error of discretized parallel plate view factor calculations with $\Delta x=\Delta y$ for a X/L=Y/L=1.

graphics card coupled with a four physical core CPU, the same case took 10.21 seconds to execute, indicating a factor of speed 37.6. With the doubling of the grid size per successive iteration, i.e. from 160x160 to 320x320, the computation time would increase by a factor of eight, i.e. from 384.66 to over 6,000 seconds, resulting in computation on the order of hundreds of days to successfully resolve large-grid solutions. As the grid sizes became larger, the hybridized CPU-GPU scheme yielded greater speed-up values, with values approaching 100x for the 2,560x2,560 cases. By employing the hybridized CPU-GPU scheme to CPU with eight physical cores and GPU with 5,632 processors, the computation time for the largest model tested was reduced to 3.85 days.

3.2.2 Effect of H and t_{int}

Figure 25a-e illustrates the effects of height to width H/W and interconnector thickness t_{int} on F_{ij} for all given packing densities. For a given H/W, increasing t_{int} monotonically decreases F_{ij} and the percent reduction in F_{ij} between given t_{int} values decreases with an increase in H/W. As H/W increases, F_{ij} decreases non-linearly. As H of the thermoelectric material or t_{int} increases, the total height H_{total} of the unicouple increases. This results in a decrease of the polar angle between the unit normal vector $\overrightarrow{n}$ and vector $\overrightarrow{R}$ connecting the two differential areas and an increase in the magnitude of $\overrightarrow{R}$. This concept is illustrated in Fig. 26.

As an example, taking the same packing density of θ=0.9 and the same t_{int}=0.25 mm, the dimension of the in-plane length Y of the unicouple is constant at 1.05 mm and the width X is constant at 2.1 mm. By varying the H of the elements from 0.5 to 1.75 mm while keeping W invariant at 1 mm, the most extreme polar angle in the 2D y-z plane decreases from 70.5 to 51.5 degrees, whereas the magnitude of $\overrightarrow{R}$ increases from 1.45 mm to 2.28 mm. For cases where the top and bottom plates are parallel, ϕ_i=ϕ_j=ϕ, resulting in the numerator in eqn. 3.4 being equivalent to $\cos^2(\phi)$. The quantity of $\cos^2(\phi)/\overrightarrow{R}^2$ decrease from 0.224 deg.^{2}/mm^2 to 0.133 deg.^{2}/mm^2, decreasing that particular F_{ij} value as expressed in eqn. 3.4 for given differential areas. Additionally, in reference to Fig. 23, increasing the distance L between two plates of the same X and Y lengths results in a decrease of F_{ij}. This example, as illustrative and insightful as it is, does not always portray the same relation between ϕ, $\overrightarrow{R}$ and F_{ij} and sometimes yields an increase in the F_{ij} value. However, the overall trend after summing all F_{ij} interactions is that increasing H and t_{int} decreases F_{ij}. The interplay of ϕ and $\overrightarrow{R}^2$ results in a non-linear trend of F_{ij} with respect to height and interconnector thickness.

3.2.3 Effect of Packing Density

Increasing the packing density decreases the view factor between the two participating ceramic plates. This is due to two competing factors: a decrease in exposed radiative and absorbing surface area of the ceramic plates and an increase in ray collisions. As θ increases and the subsequent spacing between thermoelectric elements W_{gap} decreases, the amount of exposed area of the participating ceramic plates decreases. By defining ψ as the ratio of the area of the interconnector A_{int} per area of ceramic A_m for the case were W_P=W_N=W, ψ exhibits a near-linear trend with respect to θ within the range of 0.1$\leq$ θ $\leq$0.9 such that ψ=0.5(θ+$\sqrt{\theta}$). Thus, increasing the packing density decreases available radiative and absorbing area and contributes to a decrease of F_{ij}. Furthermore, as the packing density increases, the length and depth of the ceramic plate are reduced, decreasing the maximum polar angle ϕ and reducing the magnitude of $\overrightarrow{R}$. For a case with the same H/W and t_{int} values, increasing θ causes a non-linear effect on F_{ij}. Additionally, at higher packing densities the number of interactions due to the shadow effect increases, decreasing the number of participating rays. These competing effects yield a non-linear, decreasing effect on F_{ij} as θ increases.

From the stated results, F_{ij} behaves non-linearly with respect θ. Current predictions of F_{ij} with respect to packing density assumes linearity [138], which grossly overpredicts radiation heat transfer within a TED cavity as evidenced by Fig. 27. The case compared in Fig. 27 represents the conditions that will yield the largest F_{ij} values per θ; H/W and t_{int} are kept invariant at 0.5 and 0.125 mm, respectively. It is evident there is an exponential decrease in F_{ij} with an increase in θ with values approaching zero as θ approaches unity. Although the values for F_{ij} are on the order of 10^{-4} for high-packing density cases (θ=0.9), their contribution to radiation heat transfer is still important for high-temperature applications as evidenced by the power the temperatures in eqn. 3.8.

3.2.4 Validation

The Grid Convergence Method [157] is employed to quantify error within the presented numerical results. The Grid Convergence Method is the standard for the American Society of Mechanical Engineers (ASME) to report and quantify discretization error estimates within numerical calculations. This method involves calculating the discretization error based on three solutions obtained from three different grid resolutions and reporting the results in the form of a fine-grid convergence index (GCI). The results of the calculations for each case are presented in Table. 5 within the parentheses. It is noted that highest numerical uncertainty of any solution is 0.93%. Additionally, using double-precision within the calculation reduces round-off errors associated with calculations.

3.3 CONCLUSIONS

Within Chap. 3, the radiation view factors F_{ij} between the two primary participating surfaces within a three-dimensional unit-cell thermoelectric device cavity were numerically resolved using a hybrid CPU-GPU code executed in Java with Aparapi. The need for developing a code to resolve F_{ij} between the two aforementioned participating surfaces arose from deficiencies addressed in Chap. 2, Sec. 2.4.5. It was shown in the previous chapter that the predictions of power output and thermal conversion efficiency were highly sensitive to the radiation heat transfer coefficient prescribed. The key findings are summarized as follows:

1. The code was developed in C++ and Java with Aparapi to take into account the shadow effect from all interior three dimensional geometries using a point-in-polygon algorithm. The development of the code in Java and Aparapi was done so to capitalize on the massively-parallel nature of the problem and utilize hybrid CPU-GPU computing, which decreased calculation time by over two orders of magnitude.
2. The code was compared against analytic solutions for F_{ij} between two parallels plates, yielding good agreement. The numerical solution to F_{ij} per particular case achieved residuals between successive iterations of less than 10^{-3}. Additionally, the results were

validated using the Grid Convergance Method with a maximum numerical error of less than one percent, which was based upon solutions to three successive iterations evaluated at 640x640, 1,280x1,280 and 2,560x2,560, respectively.

3. The effect of thermoelectric height H per width W ($0.5 \leq H/W \leq 1.75$), interconnector thickness ($0.125 \leq t_{int}$ mm≤ 0.25) and packing density ($0.1 \leq \theta \leq 0.9$) were considered. F_{ij} behaves non-linearly with respect to θ exhibiting exponential decay with an increase in θ due to decreased participating surface areas and an increase in ray collisions. Increasing the leg height to width ratio of the thermoelectric material and interconnector thickness non-linearly and monotonically decreases F_{ij}, respectively, due to interplay of the ratio of the polar angles squared per magnitude of ray squared.
4. By applying the value of F_{ij} and known emissivitiy values of alumina ceramic to the analytical model developed in Chap. 2, proper determination of radiation heat transfer within the thermoelectric device cavity is able to be determined.

Table 5: Radiation view factor F_{ij} values for various packing densities θ, height to width ratios H/W and interconnector thickness t_{int}. The percent numerical error is within the parentheses.

View Factor F_{ij}						
θ	H/W	t_{int}				
		0.125	*0.15625*	*0.1875*	*0.21875*	*0.25*
0.1	*0.50*	**0.389** (0.11)	**0.371** (9.1e-2)	**0.354** (7.7e-2)	**0.339** (8.6e-2)	**0.324** (5.6e-2)
	0.75	**0.334** (9.5e-2)	**0.320** (0.11)	**0.307** (0.18)	**0.294** (0.13)	**0.282** (0.13)
	1.00	**0.290** (0.12)	**0.279** (0.16)	**0.268** (0.17)	**0.258** (0.15)	**0.248** (0.24)
	1.25	**0.255** (0.21)	**0.245** (0.15)	**0.237** (0.21)	**0.228** (0.20)	**0.220** (0.12)
	1.5	**0.225** (0.19)	**0.217** (0.22)	**0.210** (0.18)	**0.203** (0.21)	**0.196** (0.18)
	1.75	**0.201** (0.28)	**0.194** (0.22)	**0.188** (0.23)	**0.182** (0.19)	**0.176** (0.35)
0.3	*0.50*	**0.126** (0.20)	**0.116** (0.21)	**0.107** (0.19)	**9.91e-2** (0.21)	**9.21e-2** (0.26)
	0.75	**9.70e-2** (0.20)	**9.03e-2** (0.19)	**8.43e-2** (0.19)	**7.88e-2** (0.18)	**7.38e-2** (0.20)
	1.00	**7.72e-2** (0.17)	**7.25e-2** (0.17)	**6.82e-2** (0.17)	**6.42e-2** (0.17)	**6.06e-2** (0.18)
	1.25	**6.30e-2** (0.16)	**5.95e-2** (0.17)	**5.63e-2** (0.17)	**5.33e-2** (0.17)	**5.06e-2** (0.17)
	1.5	**5.23e-2** (0.15)	**4.97e-2** (0.16)	**4.72e-2** (0.16)	**4.49e-2** (0.16)	**4.28e-2** (0.19)
	1.75	**4.41e-2** (0.15)	**4.20e-2** (0.15)	**4.01e-2** (0.16)	**3.83e-2** (0.16)	**3.06e-2** (0.15)
0.5	*0.50*	**3.94e-2** (0.28)	**3.56e-2** (0.30)	**3.23e-2** (0.30)	**2.95e-2** (0.32)	**2.70e-2** (0.36)
	0.75	**2.86e-2** (0.26)	**2.63e-2** (0.26)	**2.42e-2** (0.28)	**2.23e-2** (0.29)	**2.07e-2** (0.31)
	1.00	**2.19e-2** (0.23)	**2.03e-2** (0.24)	**1.89e-2** (0.26)	**1.76e-2** (0.27)	**1.64e-2** (0.28)
	1.25	**1.73e-2** (0.22)	**1.62e-2** (0.23)	**1.52e-2** (0.24)	**1.42e-2** (0.25)	**1.34e-2** (0.26)
	1.5	**1.40e-2** (0.21)	**1.32e-2** (0.22)	**1.24e-2** (0.24)	**1.17e-2** (0.24)	**1.11e-2** (0.26)
	1.75	**1.15e-2** (0.21)	**1.09e-2** (0.22)	**1.04e-2** (0.23)	**9.84e-3** (0.24)	**9.35e-3** (0.24)
0.7	*0.50*	**9.26e-3** (0.81)	**8.32e-3** (0.83)	**7.53e-3** (0.86)	**6.86e-3** (0.89)	**6.28e-3** (0.93)
	0.75	**6.50e-3** (0.80)	**5.94e-3** (0.82)	**5.46e-3** (0.85)	**5.05e-3** (0.87)	**4.68e-3** (0.89)
	1.00	**4.84e-3** (0.76)	**4.48e-3** (0.76)	**4.17e-3** (0.82)	**3.89e-3** (0.85)	**3.64e-3** (0.87)
	1.25	**3.77e-3** (0.75)	**3.51e-3** (0.78)	**3.29e-3** (0.80)	**3.09e-3** (0.83)	**2.91e-3** (0.85)
	1.5	**3.02e-3** (0.71)	**2.83e-3** (0.75)	**2.66e-3** (0.79)	**2.51e-3** (0.81)	**2.38e-3** (0.85)
	1.75	**2.47e-3** (0.70)	**2.33e-3** (0.74)	**2.20e-3** (0.77)	**2.08e-3** (0.80)	**1.98e-3** (0.81)
0.9	*0.50*	**7.38e-4** (1.6e-4)	**6.66e-4** (1.4e-4)	**6.05e-4** (1.3e-4)	**5.52e-4** (8.9e-5)	**5.06e-4** (6.5e-5)
	0.75	**5.08e-4** (2.3e-4)	**4.68e-4** (1.6e-4)	**4.32e-4** (1.1e-4)	**4.00e-4** (1.0e-4)	**3.72e-4** (8.9e-5)
	1.00	**3.74e-4** (2.1e-4)	**3.48e-4** (1.7e-4)	**3.25e-4** (1.4e-4)	**3.04e-4** (1.2e-4)	**2.85e-4** (8.9e-5)
	1.25	**2.86e-4** (2.4e-4)	**2.69e-4** (1.8e-4)	**2.53e-4** (1.6e-4)	**2.39e-4** (1.3e-4)	**2.25e-4** (1.1e-4)
	1.5	**2.26e-4** (3.3e-4)	**2.14e-4** (2.2e-4)	**2.03e-4** (1.6e-4)	**1.92e-4** (1.4e-4)	**1.82e-4** (1.3e-4)
	1.75	**1.83e-4** (3.1e-4)	**1.74e-4** (2.4e-4)	**1.66e-4** (1.9e-4)	**1.58e-4** (1.5e-4)	**1.50e-4** (1.2e-4)

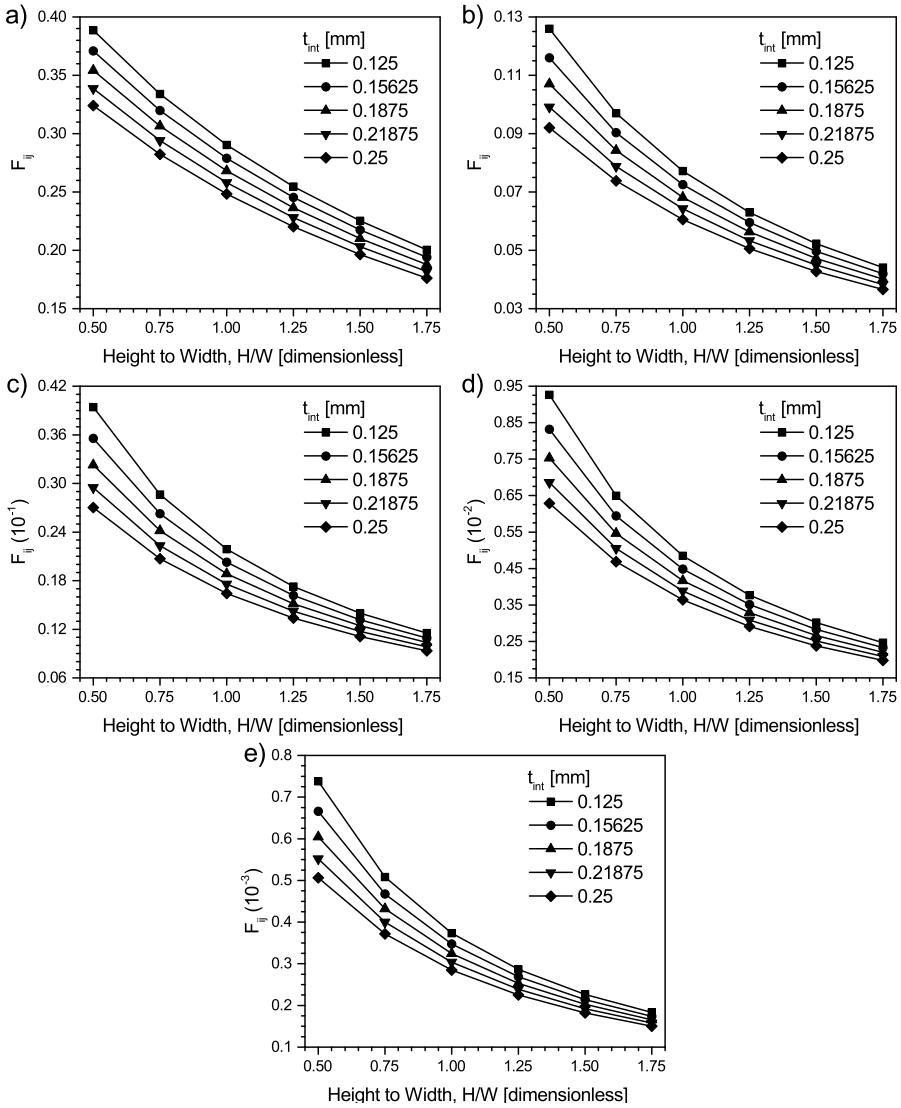

Figure 25: Effect of thermoelectric material height to width H/W and interconnector thickness t_{int} on F_{ij} for packing densities of a) θ=0.1. b) θ=0.3, c) θ=0.5, d) θ=0.7 and e) θ=0.9.

Table 6: Grid independence results for H/W=0.5, t_{int}=0.125 with a) θ=0.1 and b) θ=0.9.

	case a)		case b)	
Grid size	Value	Residual	Value	Residual
10x10	0.36033	–	0	–
20x20	0.39753	1.03e-1	2.75170e-3	–
40x40	0.39900	3.69e-3	7.06748e-4	7.43e-1
80x80	0.38555	3.37e-2	6.93650e-4	1.85e-2
160x160	0.39025	1.22e-2	6.94094e-4	6.40e-4
320x320	0.38758	6.83e-3	6.94863e-4	1.11e-3
640x640	0.38877	3.08e-3	6.95324e-4	6.64e-4
1,280x1,280	0.38895	4.26e-4	7.37877e-4	6.12e-2
2,560x2,560	0.38858	9.69e-4	7.38077e-4	2.71e-4

Table 7: Comparison of radiation view factor F_{ij} values for a packing densities θ=0.1, various height to width ratios H/W and interconnector thickness t_{int}=0.125 as calculated via C++ and Java with Aparapi for a 640x640 grid.

H/W	Percent Difference
0.50	2.96e-10
0.75	1.59e-6
1.00	1.62-9
1.25	4.75e-9
1.5	2.14e-8
1.75	2.54e-9

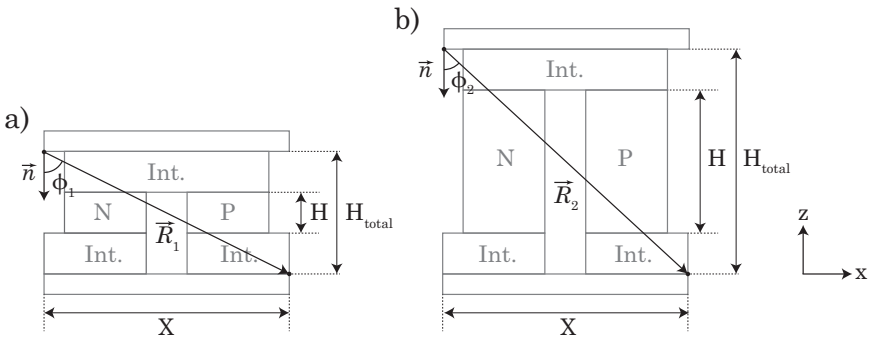

Figure 26: Illustration of the effect of thermoelectric material height H on the magnitude of a ray R and polar angle ϕ with a) reflecting H=0.5 mm and b) of H=1.75 mm for a given packing density and interconnector thickness.

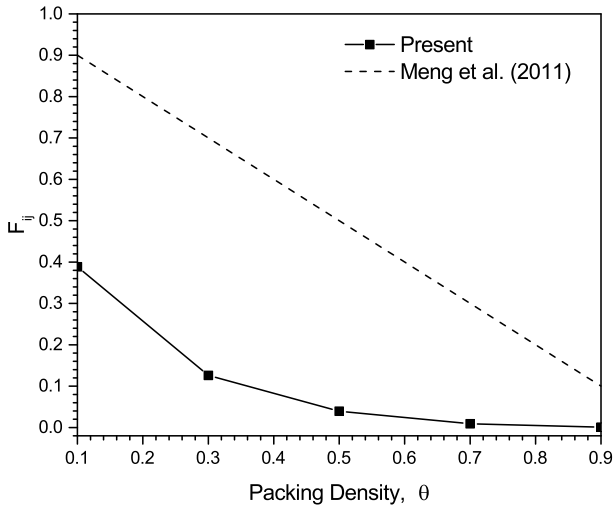

Figure 27: Comparison of present numerical results and those found within literature [138] for F_{ij} between participating hot- and cold-side ceramic plates within a TEG as a function of packing density θ. Present numerical results were based upon H/W=0.5 and t_{int}=0.125 mm.

4.0 EXPERIMENTAL STUDIES ON A SINGLE-STAGE INTEGRATED THERMOELECTRIC DEVICE

4.1 INTRODUCTION

From Chap. 2, Sec. 2.4.6, it was found that the hot-side ceramic and associated greases between the hot-side heat exchanger and hot-side interconnector contribute account for at a maximum of 8% of the total thermoelectric electric device thermal resistance. Decreasing the thermal resistance between heat source and sink has the potential for increasing the temperature difference across the thermoelectric unicouple junction, thus increasing device performance per given operating condition in comparison to a conventional device that includes the aforementioned resistive components. This chapter presents the single-stage integrated thermoelectric device based upon the experimental [158]. To address the current issue of a large thermal resistance between the source and sink when applying conventional TEDs to waste heat recovery applications, authors [87, 84, 86] [58, 88] [85, 89] have proposed and analytically and numerically investigated the integrated thermoelectric device (iTED).

An iTED is a reconfigured conventional TED where the hot-side heat exchanger is directly incorporated into the hot-side interconnector. The hot-side heat exchanger is not electrically insulated from the TE materials, allowing the device to operate electrically in series and thermally in parallel. The working fluid is then directed through the hot-side heat exchanger via flow channels, which prevent the working fluid from entering the cavity between the thermoelectric legs. This configuration eliminates the need for an electrically insulating and low thermal conductivity ceramic plate between the hot-side heat exchanger and interconnector. For a given set of operating conditions, the iTED has increased performance in terms of power output as compared to a conventional TED due to the decreased

thermal resistance between the heat source and sink; this reduction increases the temperature difference across the thermoelectric elements thereby increasing the power output. This study presents the experimental investigations on the performance of a single-stage iTED comprised of n- and p-type bismuth-telluride semiconductors applied to low-grade waste heat recovery under various inlet flow conditions. The influence of inlet flow rate and temperature and load resistance on the iTED's thermoelectric performance are investigated.

4.2 MATERIALS AND METHODS

An integrated thermoelectric device (iTED) was made with bulk n-type 75% Bi_2Te_3-25% Bi_2Se_3 and p-type 25% Bi_2Te_3-75% Sb_2Te_3 (1.75% excess Se) bismuth-telluride semiconductors. The n- and p-type bismuth-telluride square cuboids were chemically bonded onto the top and bottom surfaces of medium-phosphorus nickel-plated oxygen-free high thermal conductivity (OFHC) copper heat exchangers using a silver filled epoxy ($\rho \leq$0.4 mΩ-cm, κ=7.927 W-m^{-2}). The hot-side heat exchangers had internal rectangular flow channels and were also the hot-side interconnectors for the p-n junctions. This arrangement allowed the n- and p-type thermoelectric materials to be in direct contact, both thermally and electrically, to the hot-side heat exchanger, thereby eliminating the need for an electrical insulator, like ceramics, as seen in conventional TED designs. The iTED operates thermally in parallel and electrically in series like a conventional TED.

The p-n junctions not established via the internal heat exchangers were established through medium-phosphorus nickel-plated OFHC interconnectors, which were in contact with, but electrically isolated from, a cold reservoir of temperature T_c and acted as terminals when the device was connected to external loads of resistance R_L. Figure 28a depicts an iTED module. The geometry of a leg (single p-n junction) within an iTED module is as follows: the p- and n-type thermoelectric materials had a cross-sectional area of 25 mm^2 (5 mm by 5 mm) and a thickness of 1 mm; the heat exchanger had a cross-sectional area of 25 mm^2 (5 mm by 5 mm) and height of 10 mm; the interconnector had a width of 5 mm, length of 15 mm and height of 1 mm.

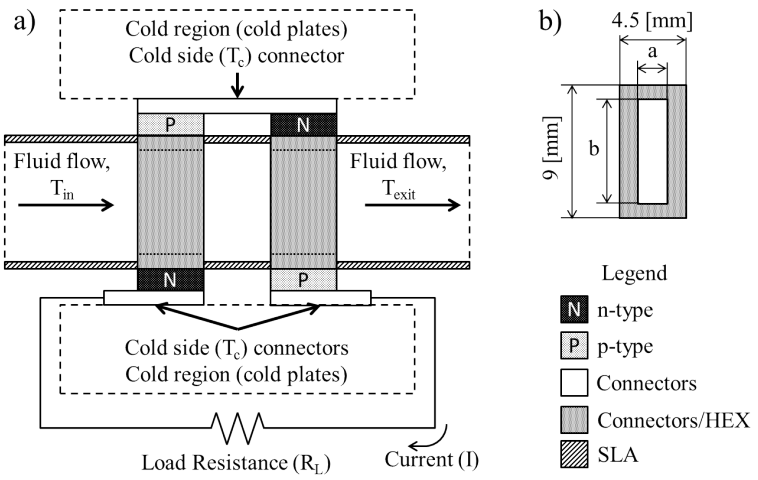

Figure 28: Schematics of a) an integrated thermoelectric device and b) cross-sectional view of the flow channel configuration; $a = 2mm$ and $b = 7.07mm$.

Inlet flow was directed from the source to the first heat exchanger, between the first and second heat exchangers and then away from the module through electrically insulated flow channels. The flow channels were constructed of Somos ® NanoTool resin and printed using stereolithography by Fineline^{TM}, Raleigh, NC, USA. The inlet and exit channels had sufficient length such that fully developed flow was established before entering the first heat exchanger and before exiting the iTED. The length of the intermediate channel was 5 mm. The internal width and height of the inlet, intermediate and exit channel was 4.5 by 9 mm. The flow cross-sectional area A_c of the hot-side heat exchanger was 14.14 mm^2 and the surface area A was 90.71 mm^2. The ratio of A to A_c of the hot-side heat exchanger was $\phi_{FA} = 6.415$. Figure 28b depicts the heat exchanger geometry that was exposed to the flow.

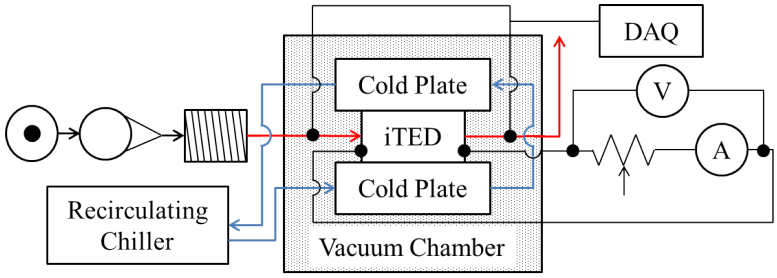

Figure 29: Schematic of test set-up. Compressed air is passed through a rotameter and coil heater before entering the iTED module. A voltmeter is used to measure the voltage drop across the ammeter and resistance simulator (potentiometer).

4.3 EXPERIMENTAL

Figure 29 illustrates the schematic of the experimental setup. The iTED was placed in a vacuum chamber with a working vacuum of 27.5 inHg to minimize convection from the external surfaces. Hot air was passed through the iTED via the inlet channel with flow rates ($\dot{\forall}$) varying from 100 to 200 L/min and temperatures between 50 and 150 °C. Compressed air was passed through a Dwyer VFB-55-SSV rotameter and a coil-wrapped heater before entering the iTED. The inlet and exit temperatures (T_{in} and T_{exit}) of the air were measured with high-temperature K-type thermocouples. All thermocouple voltages were measured using a National Instruments Data Acquisition system (NiDAQ) with a built-in reference temperature and analyzed using National Instruments VI-Logger software.

The heat Q_h added to the iTED is expressed by Eqn. 4.1. Q_h was calculated via the volumetric flow rate of the fluid $\dot{\forall}$, the temperature-dependent density ρ and specific heat C_p, which were evaluated at the average temperature of the fluid flow (i.e. the average of the inlet and exit temperatures, T_{in} and T_{exit}) and the temperature difference between the inlet and exit fluid flow, such that

$$Q_h = \dot{\forall}\rho C_p(T_{in} - T_{exit}). \tag{4.1}$$

To simulate a cold-side reservoir, the top and bottom surfaces of the iTED were placed in contact with electrically insulated cold plates. A 50/50 mixture of water and ethylene glycol was passed through the cold plates using a recirculating chiller. The temperatures of the cold plates were kept constant at T_c=0 °C.

The iTED was connected electrically in series to an Agilent U3606A ammeter and an IET Labs RS-RTD resistance simulator which represented load circuitry of resistance R_L. The U3606A was used to measure the produced current I. An Agilent U34401A multimeter was used to measure the voltage V produced by the iTED, which is the summation of the Ohmic (V_{ohm}) and Seebeck (V_{oc}) voltages. The uncertainties associated with the voltage and current measurements are 0.025%. The resistance simulator's load resistance R_L was adjusted between 0.01 and 5,000 ohms and the power output of the iTED was calculated via the second and third expressions of Eqn. 4.2, which is expressed as

$$P_o = IV = I^2 R_L = \frac{\alpha^2 R_L}{(R_L + R_{in})^2} \Delta T^2. \tag{4.2}$$

Evaluating the second and third expressions of Eqn. 4.2 yields the same result within error of the measurement system. The term α of the fourth expression is the summation of the absolute values of n- and p-type Seebeck coefficients, R_{in} is the internal resistance of the iTED and ΔT is the temperature difference across the p-n junctions. The fourth expression of Eqn. 4.2 is provided only to illustrate the effect of R_L and ΔT on P_o and was not evaluated to determine P_o. The efficiency of the iTED was calculated using the power output and heat input, expressed as

$$\eta = \frac{P_o}{Q_h}. \tag{4.3}$$

A FLIR® SC-325 thermal camera was used to image the surface of the iTED and determine the temperature difference ΔT across the thermoelectric elements. The iTED was painted matte black and the camera was calibrated to thermocouple measurements at 25 and 150 °C. The thermal images were evaluated using FLIR® ExaminIR™ software. Each test was conducted three times to determine the average temperatures of the working fluid and the thermoelectric characteristics V, I, P_o, Q_h and η, as well as ΔT.

4.4 RESULTS AND DISCUSSION

The thermoelectric performance of an integrated thermoelectric device with a rectangular flow channel in terms of produced electric current I and voltage V, calculated power output P_o and thermal conversion efficiency η under various flow conditions (2,200$\leq$ Re_{Dh} $\leq$9,900, 50$\leq$ T_{in} (°C)$\leq$150) and load resistances (0$\leq$ R_L (Ω) $\leq$5,000) has been experimentally investigated. The effect of inlet temperature, flow rate, as expressed by the Reynolds number, and load resistance are presented.

4.4.1 Effect of Inlet Temperature

Figure 30 illustrates the electrical characteristics for an integrated thermoelectric device under various fluid inlet temperatures and Reynolds numbers (50$\leq$ T_{in} (°C)$\leq$150, 2,200$\leq$ Re_{Dh} $\leq$3,300). The produced voltage V is the summation of the V_{ohm} and V_{oc} voltages. V obeys Ohm's law such that it is equal to the produced current I time the resistance R, which is the summation of the load R_L and internal R_{in} resistance. The increase in voltage scales linearly with an increase in fluid inlet temperature T_{in}. For instance, as T_{in} increases from 50 to 75 $°C$ and 125 to 150 $°C$ (1.5- and 1.2-fold increase), the maximum voltage increases from 12.52 to 18.66 mV and 33.00 to 39.72 mV (1.49- and 1.20-fold increase). Likewise, the I produced follows the same linear trend with an increase in T_{in}, such that as a 3-fold increase in T_{in} resulted in an increase in the maximum I value by 3.07-fold, as evidenced by Fig. 30 and Fig. 31. The P_o increases non-linearly with an increase in T_{in}; as T_{in} is increased 1.5-, 2-, 2.5- and 3-fold for the 3,300 to 2,200 Re_{Dh} cases (Fig. 30), the maximum power output increased 2.23-, 4.28-, 6.72- and 9.72-fold, respectively.

Figure 32 illustrates the effects of T_{in} on the maximum power output $P_{o,max}$ and maximum produced voltage V_{max}. Increasing T_{in} drastically increases $P_{o,max}$ and V_{max} values. For roughly the same Re_{Dh} values (3,300 and 2,200), a 3-fold increase in T_{in} (50 to 150 °C) results in a 9.72- and 3.17-fold increase in $P_{o,max}$ and V_{max} values, respectively. $P_{o,max}$ is proportional to ΔT^2 as seen by the fourth expression of Eqn. 4.2. By increasing T_{in} from 50 to 150 °C, the temperature difference across the thermoelectric legs ΔT, as measured by the

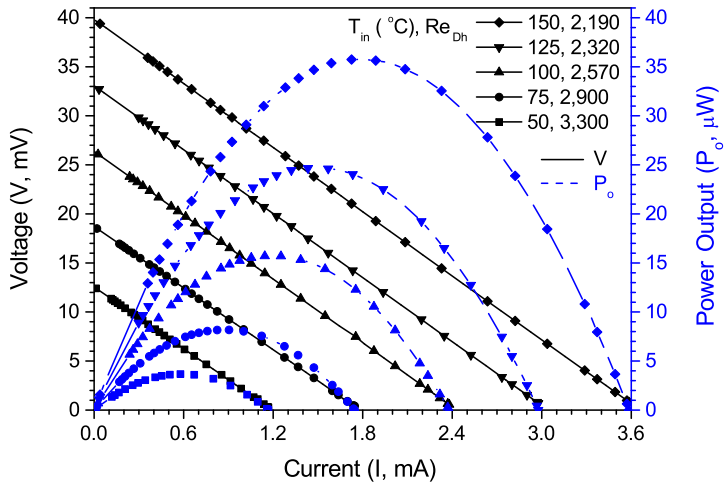

Figure 30: Voltage V, current I and power output P_o of an iTED with various inlet temperatures T_{in} and Reynolds numbers Re_{Dh} with a cold-side temperature of 0 °C.

thermal camera, increased from 19.0 to 58.4 °C, as illustrated in Fig. 33. The 3-fold increase in T_{in} resulted in a 3.07-fold increase in ΔT across the TE material, which corresponds very closely to the 9.72-fold increase in $P_{o,max}$ and is within error of the measurement system.

Figure 34 illustrates that increasing T_{in} increases Q_h and η. The heat input increases more with an increase in T_{in} than does η such that a 1.5-, 2-, 2.5 and 3-fold increase in T_{in} results in a 1.79-, 2.21-, 2.65- and 3.47-fold increase in Q_h and a 1.17-, 1.90-, 2.43- and 2.81-fold increase in η. As T_{in} increases from 50 to 150 °C, the density of the working fluid decreases from 1.097 to 0.8345 kg-m^3 and the dynamic viscosity increases from $1.760{\cdot}10^{-5}$ to $4.623{\cdot}10^{-5}$ kg-m^{-1}-s^{-1}, resulting in a decreasing Reynolds number for the same flow area (i.e. from 3,300 to 2,200). With a decreasing Reynolds number comes a decrease in the convective heat transfer coefficient h, which would decrease Q_h for a given T_{in}. Although Re_{Dh} decreases 33.8% with a 3-fold increase in T_{in}, these Re_{Dh} values lie within the transition region between laminar and turbulent flow and the effect of decreasing Re_{Dh} on h and subsequent Q_h values are unclear and non-linear. Despite the potential decrease in h with an increase in T_{in}, ΔT

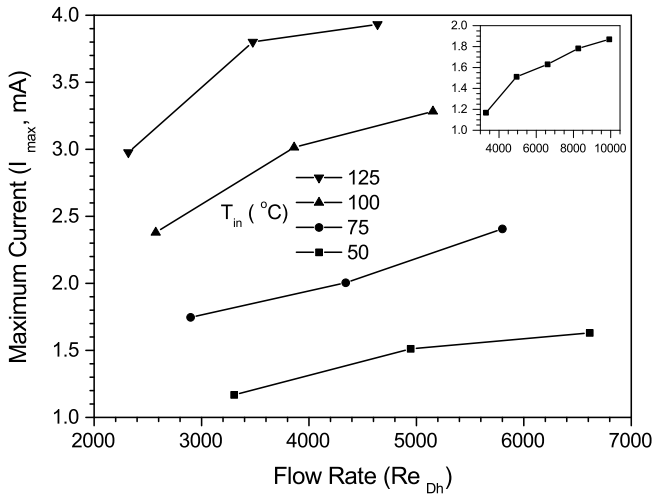

Figure 31: Effect on increasing flow rate Re_{Dh} and inlet temperature T_{in} on the maximum produced current I_{max} at R_L=0 Ω. Inset shows I_{max} versus Re_{Dh} for T_{in}=50 °C series with high Re_{Dh}.

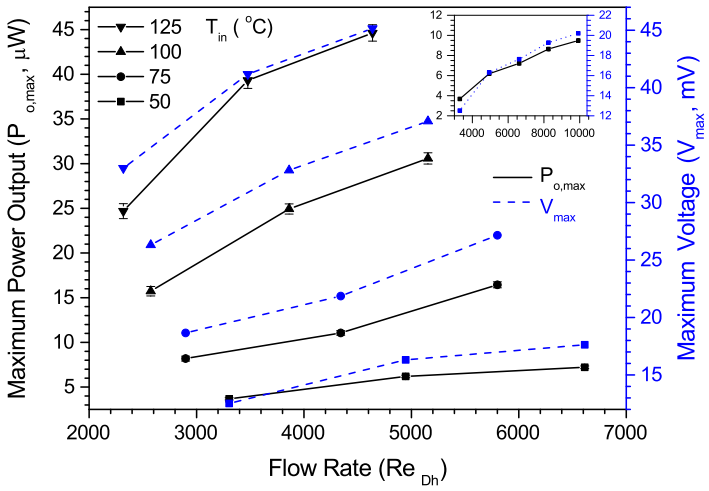

Figure 32: Effect on increasing flow rate Re_{Dh} and inlet temperature T_{in} on maximum power output $P_{o,max}$ and maximum voltage V_{max} predictions. Inset shows $P_{o,max}$ and V_{max} versus Re_{Dh} for T_{in}=50 °C series with high Re_{Dh}.

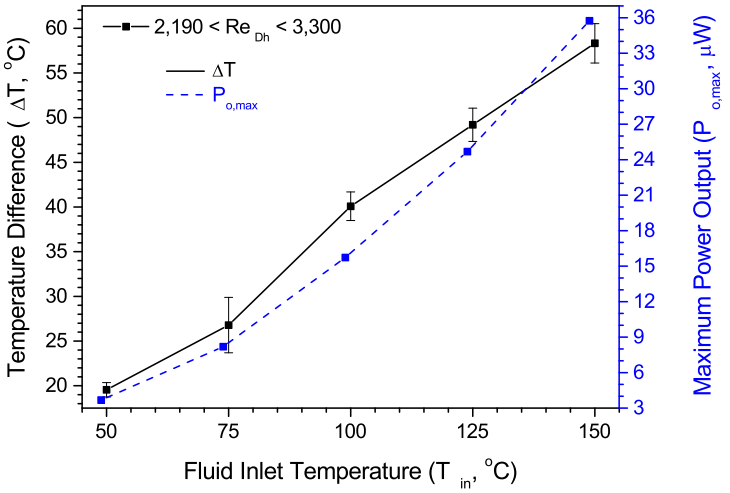

Figure 33: Effect on inlet temperature T_{in} on temperature difference ΔT across TE materials and maximum power output $P_{o,max}$ predictions.

increases linearly which results in a non-linear increase in P_o. Furthermore, Q_h increases with T_{in} and more substantially than the increase in P_o, resulting in a non-linear increase in η.

4.4.2 Effect of Reynolds Number Re_{Dh}

The effect of flow rate on I_{max} (evaluated at R_L=0 Ω) is illustrated in Fig. 31 with the high Re_{Dh} cases depicted in the inset. For T_{in}=50 °C, a 1.5-, 2-, 2.5- and 3-fold increase in Re_{Dh} results in a 1.29-, 1.40-, 1.53- and 1.60-fold increase in I_{max}. Figure 32 illustrates the effects of Re_{Dh} on the V_{max} and $P_{o,max}$ for various inlet temperatures. It is evident that an increase in Re_{Dh} marginally increases the maximum power output. With T_{in} invariant at 50 °C, a 2- and 3-fold increase in the Re_{Dh} values from 3,300 to 6,600 and 9,900 results in a 1.96- and 2.58-fold increase in $P_{o,max}$, a 1.40- and 1.61-fold increase in V_{max}, and a 1.40- and 1.60-fold increase in I_{max}. This trend is seen in all cases with different inlet temperatures.

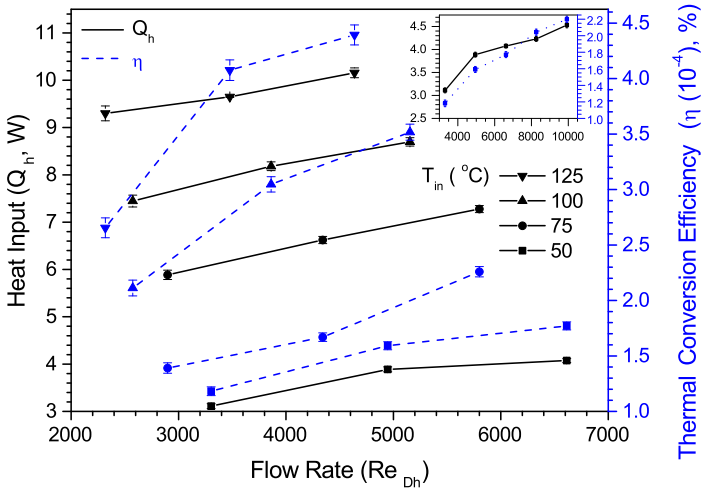

Figure 34: Effect on increasing flow rate Re_{Dh} and inlet temperature T_{in} on heat input Q_h and thermal conversion efficiency η predictions. Inset shows Q_h and η versus Re_{Dh} for T_{in}=50 °C series with high Re_{Dh}.

Figure 34 shows how an increase in Re_{Dh} causes an increase in Q_h and η. As the flow departs the transition region and becomes turbulent, i.e. an increase in Re_{Dh}, the convective heat transfer coefficient h increases. A rise in h increases Q_h and thus produces a larger ΔT across the TE elements and subsequently a larger P_o. For instance, given T_{in}=50 °C, a 2- and 3-fold increase in Re_{Dh} from 3,300 to 6,600 and 9,900 resulted in a 1.31- and 1.46-fold increase Q_h and a 1.96- and 2.58-fold increase in $P_{o,max}$, yielding a 1.50 and 1.86-fold increase in η.

However, increasing Re_{Dh} does not have as substantial an effect on the ΔT imposed upon the TE elements as does increasing T_{in}. As Re_{Dh} increased from 3,300 to 9,900 (3-fold) at a constant inlet temperature of 50 °C, ΔT across the TE elements increased marginally from 19.0 to 28.9 °C, yielding a 1.52-fold increase; in comparison, ΔT increased from 19.0 to 58.4 °C (3.07-fold) as T_{in} increased 3-fold from 50 to 150 °C.

4.4.3 Effect of Load Resistance

For an iTED with inlet fluid temperatures of 50 to 150 °C and corresponding Re_{Dh} varying from 3,300 to 2,200, Fig. 35a illustrates the effect of R_L on the P_o and Fig. 35b of R_L on I and V. From Fig. 35a, $P_{o,max}$ is produced when the R_L is equal to the R_{in}. The measured internal device resistance was 0.46 Ω at ambient, non-operating conditions, however, the system resistance including cables and connections resulted in a total system resistance of approximately 10 Ω during operating conditions. As T_{in} increases, there is a slight increase in R_{in} of the device as seen by a shift in the maxima of the curves in Fig. 35a, thus the optimum load resistance increases.

It is evident from Fig. 35b that the produced I decays while the produced V increases as R_L increases. As the total resistance increases (summation of R_{in} and R_L), V must increase and I must decrease as dictated by Ohm's law. The P_o as evaluated by the second expression of Eqn. 4.2 reaches the maximum $P_{o,max}$ when the load resistance is equal to the internal resistance, and is found where the curves depicting current and voltage intersect. These two methods, that of the maxima as illustrated in Fig. 35a (I^2R_L) and of the intersection of the I and V curves as in Fig. 35b (IV), yield concurrent optimum R_L and $P_{o,max}$ values.

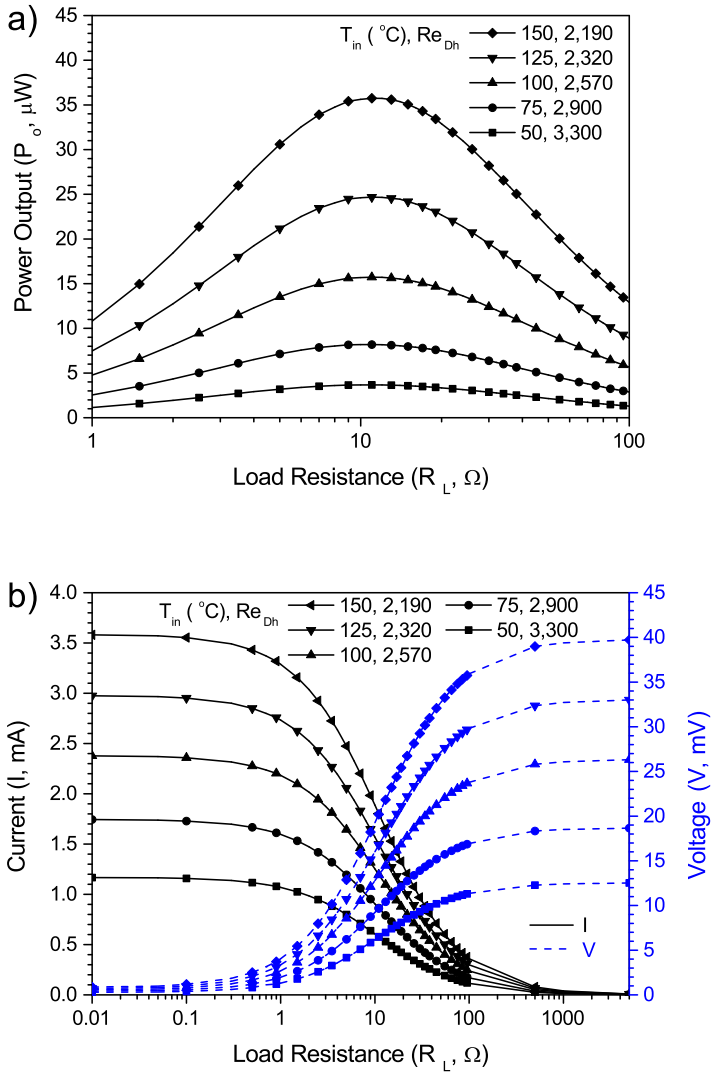

Figure 35: The effect of load resistance R_L on a) power output P_o and b) produced current I and voltage V for various inlet temperatures T_{in} and flow rates Re_{Dh}.

Irrespective of Re_{Dh} and T_{in}, the P_o and produced I and V trends follow the same behavior with a change in R_L.

4.4.4 Comparison to Conventional Thermoelectric Devices

The trend in power output per inlet temperature (Fig. 33) can be compared to that of a conventional thermoelectric device (Fig. 12). Comparing the normalized power output (power output at a given inlet temperature per maximum power output achieved) per normalized temperature difference ($T_{\infty,h}$-$T_{\infty,c}$) of the experimental iTED and conventional TED data, it is evident from Fig. 36 that the iTED has an exponentially increasing trend of $P_{o,max}$ with $T_{\infty,h}$ whereas the conventional device has a near linear trend. That is, for the same thermoelectric material and device geometry, and experienced operating conditions, the integrated thermoelectric device will yield a larger power output than the conventional thermoelectric device. This is because the hot-side junction temperature will more closely reflect the hot-side fluid temperature due to the reduction of thermal resistance between source and junction.

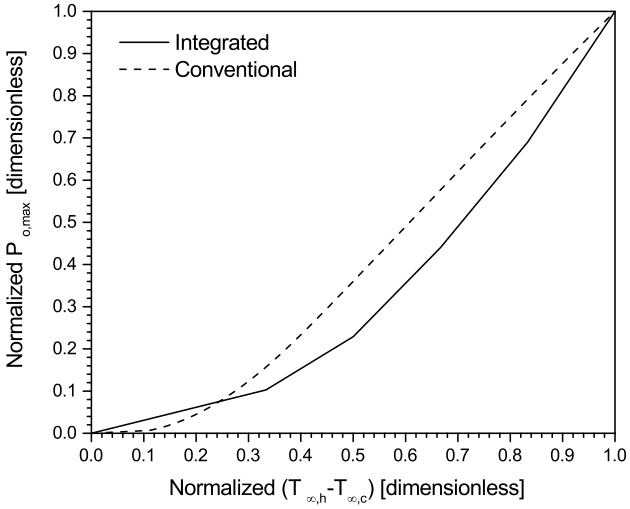

Figure 36: Normalized power output versus normalized hot minus cold fluid temperatures for a conventional and integrated thermoelectric device.

4.5 CONCLUSIONS

An integrated thermoelectric device (iTED) is a restructured TED in which the hot-side heat exchanger is integrated into the hot-side interconnector. The working fluid is then directed through the integrated heat exchanger via flow channels. This configuration reduces the thermal resistance between the waste heat source and sink, allowing for greater heat input and power output. The effects of inlet fluid temperature ($50 \leq T_{in}$ ($^{\circ}C$)≤ 150) and flow rate ($2{,}200 \leq Re_{Dh} \leq 9{,}900$) and load resistance ($0 \leq R_L$ (Ω)$\leq 5{,}000$) on the performance of an iTED in terms of produced current I and voltage V, power output P_o, heat input Q_h and conversion efficiency η have been studied. The following conclusions are summarized as follows.

1. It was found that T_{in} had a more substantial effect on the performance of an iTED than did Re_{Dh}. The P_o increases non-linearly with T_{in} whereas I, V, Q_h and η increase near-

linearly in T_{in}. A 3-fold increase in T_{in} resulted in a 3.07-fold increase in ΔT across the TE material, which resulted in a 9.72-fold increase in $P_{o,max}$. For the same increase in T_{in}, the values of I_{max}, V_{max}, Q_h and η increased 3.07-, 3.17-, 3.47- and 2.81-fold, which is attributed to the linear increase of ΔT across the TE material with T_{in}.

2. While increasing Re_{Dh} with T_{in} fixed, the V, I, $P_{o,max}$, Q_h and η values did not increase as drastically compared to an increase in T_{in}. For a constant T_{in}=50 °C, a 3-fold increase in Re_{Dh} resulted in 1.61-, 1.60-, 2.58-, 1.46- and a 1.86-fold increase in V_{max}, I_{max}, $P_{o,max}$ Q_h and η, respectively. Increasing Re_{Dh} increased the convective heat transfer coefficient h, which increases the amount of heat delivered to the heat exchangers. However, the non-linear increase in h and subsequent Q_h did not increase the ΔT across the thermoelectric elements as drastically as an increase in T_{in}, thus the performance did not increases as greatly as compared to an increase in T_{in}. For instance, with a constant T_{in}=50 °C, a 3-fold increase in Re_{Dh} resulted in a 1.52-fold increase in ΔT.
3. Increasing the load resistance R_L increases the produced V and decreases the produced I. Additionally, increasing R_L up to the value of the internal resistance R_{in} increases P_o to the maximum $P_{o,max}$; an increment in R_L beyond R_{in} then decreases P_o.

5.0 EXPERIMENTAL STUDIES ON A MULTI-STAGE PIN-FIN INTEGRATED THERMOELECTRIC DEVICES

5.1 INTRODUCTION

The previous chapter (Chap. 4) introduced a single-stage integrated thermoelectric device. The concept of an integrated thermoelectric device has the benefit of the hot-side junction experiencing the same temperature as the hot-side heat exchanger since they are one and the same, yielding a power output that is proportional to the square of the inlet temperature. To build upon this device concept, a pin-fin integrated thermoelectric device is introduced. The advantages of a pin-fin thermoelectric device is an increased packing density, higher heat exchanger surface area and an optimum heat exchanger design per flow conditions to induce greater heat transfer. In this chapter the experimental investigations on the performance of a pin-fin integrated thermoelectric device comprised of n- and p-type bismuth-telluride semiconductors applied to low-grade waste heat recovery are performed [159]. The iTED has a rectangular flow channel that uses staggered tube-bank heat exchangers to extract heat from the simulated waste heat source. The cold-side interconnectors are exposed to a simulated finite heat sink. The influence of hot fluid flow rate (Re) and inlet temperature T_{in} (°C), and load resistance R_L (Ω) on the iTED's performance in terms of thermoelectric characteristics (I, V, Q_h, P_o and η) are investigated.

The proposed integrated thermoelectric devices uses a pin-fin heat exchanger to serve two purposes; the first is to bridge the hot-side electrical connections and the second is to incorporate a heat exchanger that induces turbulence, promoting high heat transfer coefficients and heat into the p-n junctions. It has been shown that pin-fins with a height to diameter ratio greater than 2 increases pin heat transfer for lower Reynolds number flow (typically

less than 30,000) [160]. By staggering the pin-fin arrays, pin heat transfer increases due to wake turbulence produced from upstream rows, typically within the first three rows, where then it marginally diminishes [161, 162]

5.2 MATERIALS AND METHODS

An integrated thermoelectric device was made by chemically bonding thin p- and n-type bismuth-telluride cylinders onto the top and bottom surfaces of aluminum rods using a silver filled epoxy ($\rho_e \leq 0.4$ mΩ-cm, κ=7.927 W-m^{-1}-K^{-1}). The p- and n-type semiconductors were bulk 25% Bi_2Te_3-75% Sb_2Te_3 (1.75% excess Se) and 75% Bi_2Te_3-25% Bi_2Se_3 respectively. The aluminum rods were then press-fitted into a dielectric heat exchanger housing (thermally cured, high-resolution SLA NanoTool, FineLine Prototyping). The 6061 aluminum rods act as internal rod bundle exchangers. The p-n junctions not made via the aluminum rods were established through 6061 aluminum interconnectors, which were exposed to cold-plates and acted as terminals when the device was connected to external loads of resistance R_L. Upon fabrication, the device had a total electrical resistance of 29.8 Ω at room temperature. There were a total of 35 p-n junctions and a total of 140 chemically bonded electrical connections. Taking into account the total electrical resistance of all p- and n-type pellets and aluminum components, the average electrical contact resistance per connections was found to be 0.212 Ω at a reference temperature of 25 °C.

Figure 37a depicts an iTED module. The geometry of a leg (single p-n junction) within an iTED module is as follows: the p- and n-type thermoelectric materials had a diameter of of 3.2 mm and a thickness of 1.2 mm; the aluminum rod had a diameter of 3.2 mm and height of 25 mm; the aluminum interconnector had a length of 8 mm, width of 3.5 mm and thickness of 1.5 mm. Only 15.875 mm of the total 25 mm of the aluminum rod was exposed to the working fluid; the remainder was seated within the heat exchanger assembly.

The working fluid of air was directed from the heater to and through the tube bank via electrically and thermally insulated flow channels. The flow channel had a width (W) of 31.75 mm and a height (H) of 15.875 mm. The rods had a transverse spacing to diameter

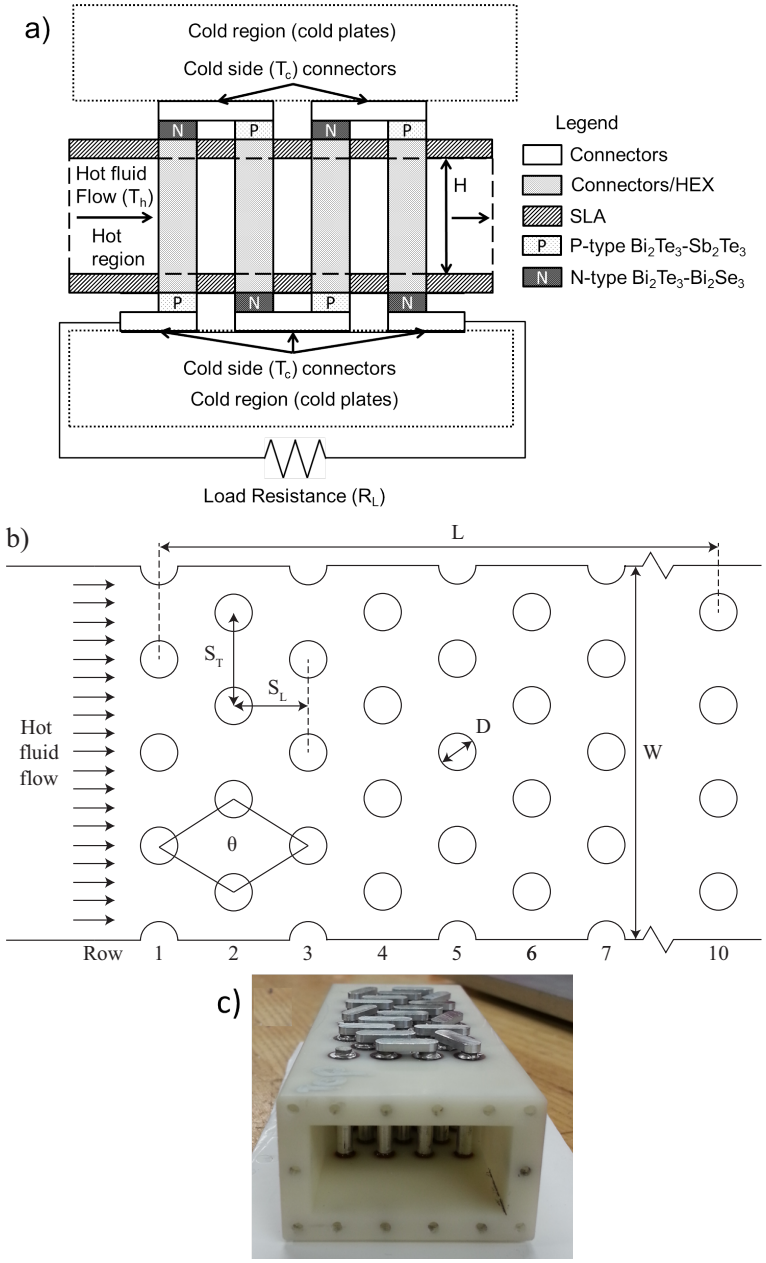

Figure 37: Schematics of a) a sideways cross-sectional view an integrated thermoelectric device, b) a top-down cross-sectional view of the flow channel configuration and c) the fabricated iTED module.

ratio (S_T/D) of 2.5, a longitudinal spacing to diameter ratio (S_L/D) of 2 and a height to diameter ratio (H/D) of 5. The longitudinal and transverse spacings were selected due to the enhancement of heat transfer within the channel for the given flow conditions and geometry [163]. This arrangement reflects a packing density of 15.7% (cross-sectional area of the p- and n-type thermoelectric elements per unit area of the heat exchanger). The staggered rods were assembled in 10 rows, with the rows alternating between 3 and 4 rods. Corbels were printed on the walls for rows that had 3 rods to keep the spacing between rod-to-rod and rod-to-wall constant, as illustrated in Fig. 37b. Figure 37c shows the iTED module with p- and n-type pellets bonded to both the aluminum rods and interconnectors.

5.3 EXPERIMENTAL

Hot air was passed through the iTED via the flow channel with volumetric flow rates ($\dot{\forall}$) varying from 100 to 200 L/min and temperatures between 50 and 150 °C. The volumetric flow rate was measured using a Dwyer VFC-131 rotameter. The inlet and exit temperatures (T_{in} and T_{exit}) of the air were measured with four K-type thermocouples placed at the respective locations. The average and standard deviation was calculated for each of the four thermocouples at the respective locations and was used as the basis of a 95% confidence interval, in which any statistical outlier was removed from the data set. The average air temperatures for the inlet and exit were then calculated based upon the average of the four thermocouples at the respective locations. All thermocouple readings were measured using a National Instruments Data Acquisition system (NiDAQ) and recorded using National Instruments VI-Logger software with a sampling rate of 1 kHz. The heat added to the iTED, Q_h, is expressed by Eq. 5.1,

$$Q_h = \rho_f \dot{\forall} C_p (T_{in} - T_{exit}) \tag{5.1}$$

where $\dot{\forall}$ is the volumetric flow rate, ρ and C_p are the density and specific heat of air, respectively, evaluated at the average of T_{in} and T_{exit}.

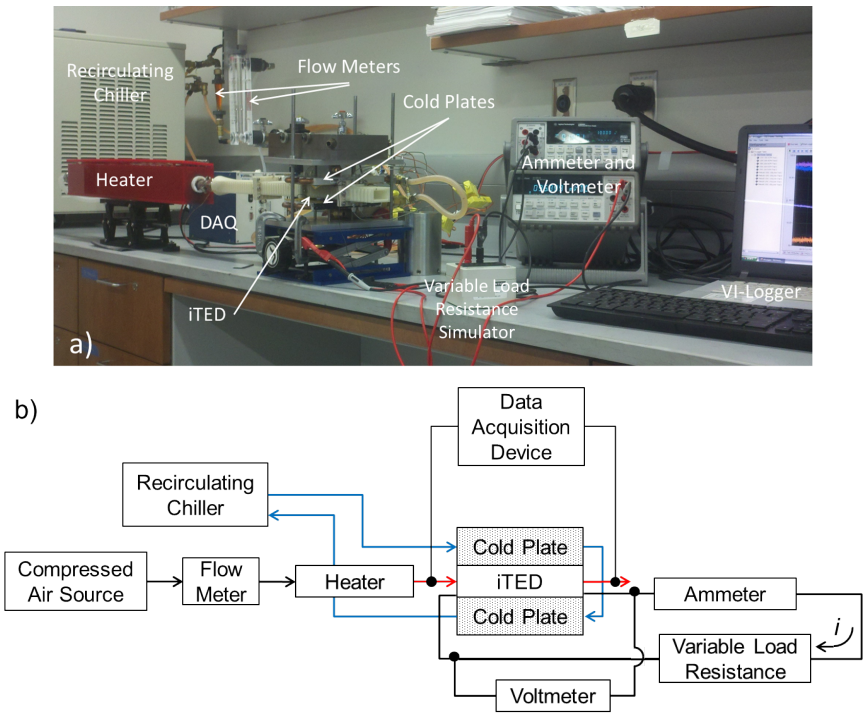

Figure 38: a) Experimental setup of and b) schematic of test setup.

To simulate a finite cold reservoir, the top and bottom surfaces of the iTED were placed into contact with electrically insulated cold plates. The cold plates were maintained at a constant temperature of 20 °C via a 50/50 mixture of water and ethylene glycol passed through a recirculating chiller with a volumetric flow rate of 4 L/min. For each simulated waste heat flow rate and inlet temperature, three tests were conducted at each condition and the average of inlet temperature T_{in} and thermoelectric characteristics (V and I) was used to calculate the power output P_o, heat input Q_h and conversion efficiency η. Figure 38a shows the experimental setup and Fig. 38b is an illustrative schematic.

The iTED was connected electrically in series to a variable electrical load resistance simulator (IET Labs RS-RTD RTD Simlator), and an Agilent U3606A ammeter, both of which represented load circuitry of resistance R_L. The U3606A ammeter was used to measure the produced current I. An Agilent U34401A multimeter was used to measure voltage drop

V across the load resistance simulator and ammeter, which is the summation of the Ohmic V_{Ohm} and Seebeck V_{oc} voltages such that

$$V = V_{Ohm} + V_{oc} = IR_{in} + \sum_{i=1}^{N} (\alpha_p \Delta T_p - \alpha_n \Delta T_n)_i. \tag{5.2}$$

R_{in} is the iTED's internal resistance, α is the temperature-dependent Seebeck coefficient, ΔT is the temperature difference across the TE pellet and N is the number of iTED legs (Fig. 37a). The load resistance simulator's resistance was adjusted between 0-9,000 Ω and the power output of the iTED was calculated via Eq. 5.3,

$$P_o = I^2 R_L = \left[\frac{\sum_{i=1}^{N} (\alpha_p \Delta T_p - \alpha_n \Delta T_n)_i}{R_L + R_{in}} \right]^2 R_L. \tag{5.3}$$

The efficiency of the iTED was calculated using the power output and heat input, expressed as

$$\eta = \frac{P_o}{Q_h}. \tag{5.4}$$

5.4 RESULTS AND DISCUSSION

The thermoelectric performance of an integrated thermoelectric device with a rectangular flow channel expressed in terms of produced electric current I and voltage V, power output P_o and conversion efficiency η, has been experimentally investigated. All thermoelectric characteristics were investigated under various flow conditions (3,020≤ Re ≤6,050, 50≤ T_{in} (°C)≤150) and load resistances ($0 \leq R_L$ (Ω) ≤9,000).

5.4.1 Effect of Inlet Temperature

With a set hot fluid flow rate of 180 L/min, the fluid inlet temperature T_{in} was varied between 49.9, 105.0 and 150.1 °C with uncertainties of 0.4, 0.8 and 1.1%, respectively. The effect of temperature on produced voltage and current are illustrated in Figs. 39a and b. As T_{in} increased from 49.9 °C (Fig. 39a), 105.0 to 150.1 °C (Figs. 39b), and while T_c maintained constant at 20 °C, the maximum voltage produced was 134.8, 308.4 and 471.7 mV respectively. Additionally, the maximum current and subsequent power produced was 0.9, 6.9 and 9.2 mA and 17.7, 529.2 and 1,078.1 μW, respectively. For a constant inlet flow rate, increasing T_{in} from 105.0 to 150.1 °C represents a 1.4-fold (i.e. 140%) increase. If it is assumed the cold-side of the pellet is the same as the cold-side working fluid, than the aforementioned increase in T_{in} represents a 1.5-fold increase in ΔT. The increase in T_{in} resulted in a 1.5-fold increase in V, a 1.3-fold increase in I and a 2.0-fold increase in P_o. The increases in V and I can been seen in Fig. 5.3b and the increase in P_o can be seen in Fig. 40.

It is evident that the V varies linearly with I and it is equal to the Seebeck voltage V_{oc} when I=0. The V_{oc} is directly proportional to the temperature differential across the TE element (Eq. 5.2); a higher T_{in} will create a larger temperature differential across the element and thus a higher V_{oc}, as illustrated by the near one-to-one correspondence of T_{in} to V_{oc} for the 105.0 and 150.1 °C cases.

The P_o shows non-linear behavior with I such that increasing the temperature differential across the thermoelectric elements results in an increase in I and an enhancement in P_o, as seen in Eq. 5.3. For instance, 1.4-fold increase in T_{in} (1.5-fold increase in ΔT) resulted in 1.5-fold increase in V, a 1.3-fold increase in I and a 2.0-fold increase in P_o. The increase in P_o is a 1.4-to-one correspondence to T_{in} as opposed to a two-to-one, which is attributed to the non-linear increase in I, which was potentially reduced from high electrical contact resistances introduced between the pellets and interconnectors.

To compare the Seebeck V_{oc} and Ohmic V_{Ohm} voltages, Eq. 5.2 can be rearranged to solve for the Seebeck coefficient α such that $\alpha = (V - IR_{in})/\Delta T$, which is evaluated with absolute temperatures. The V_{Ohm} is the total produced voltage V_{total} less V_{oc}. Comparing the production of V_{oc} and V_{Ohm} per load resistance at different temperatures, it is evident

increasing the load resistance increases V_{Ohm} and decreases V_{oc} as seen in Fig. 41. When no load is connected to the iTED, i.e. open-circuit voltage, V_{oc} is at a maximum and V_{Ohm} is at a minimum. As R_L is increased up to the optimum load resistance, that is $R_L = R_{in}$, V_{oc} and V_{Ohm} are equal. This optimum load resistance is evidenced by taking the derivative of power output P_o expressed in Eq. 5.3 with respect to R_L and setting it equal to zero. Further increasing R_L past the optimum value, V_{oc} begins to decrease to a minimum whereas V_{Ohm} increases to a maximum.

5.4.2 Effect of Flow Rate

The effect of Re (varied from 100 to 200 L/min with 50 L/min increments) on P_o and V-I characteristics has been shown in Fig. 40. Here, the hot fluid inlet temperature was maintained between 97.7 and 100.4 °C and the flow rate was varied. The Reynolds number was calculated taking into account the temperature and pressure dependent properties of air using the average temperature of the working fluid across the heat exchanger and the inlet channel geometry. The Reynolds number was found to be 3,020, 4,540 and 6,050 for the 100, 150 and 200 L/min cases, respectively. As the Re value increased 1.5- and 2.0-fold from the 100 L/min case, the maximum produced V and I and increases 1.2-, 1.1-fold and 1.2-, 1.1-fold, respectively, as illustrated in Fig. 42. Correspondingly, the maximum P_o increases 1.3- and 1.4-fold for the same increases in Re, as seen in Fig. 40

Increasing the flow rate results in a higher Re, which in turn increases the hot-side convective heat transfer coefficient h. As h increases, the amount of heat transferred between the working fluid and heat exchangers Q_h increases. Thus, an increase in Re results in an increase in Q_h, as shown in Fig. 43; as Re increased 1.5- and 2.0-fold from 3,020, Q_h increases 1.7- and 2.6-fold in comparison to 34.8 W at Re=3,020.

Additionally, an increase in Q_h has the potential to increase the hot-side temperature T_h and ultimately the temperature differential ΔT across the TE elements, if T_c is able to be maintained. A larger ΔT across the TE elements linearly increases V and quadratically increases P_o. However, it is evident from the experiments the increases in developed V and I and subsequent P_o do not scale proportionally with an increase in Re.

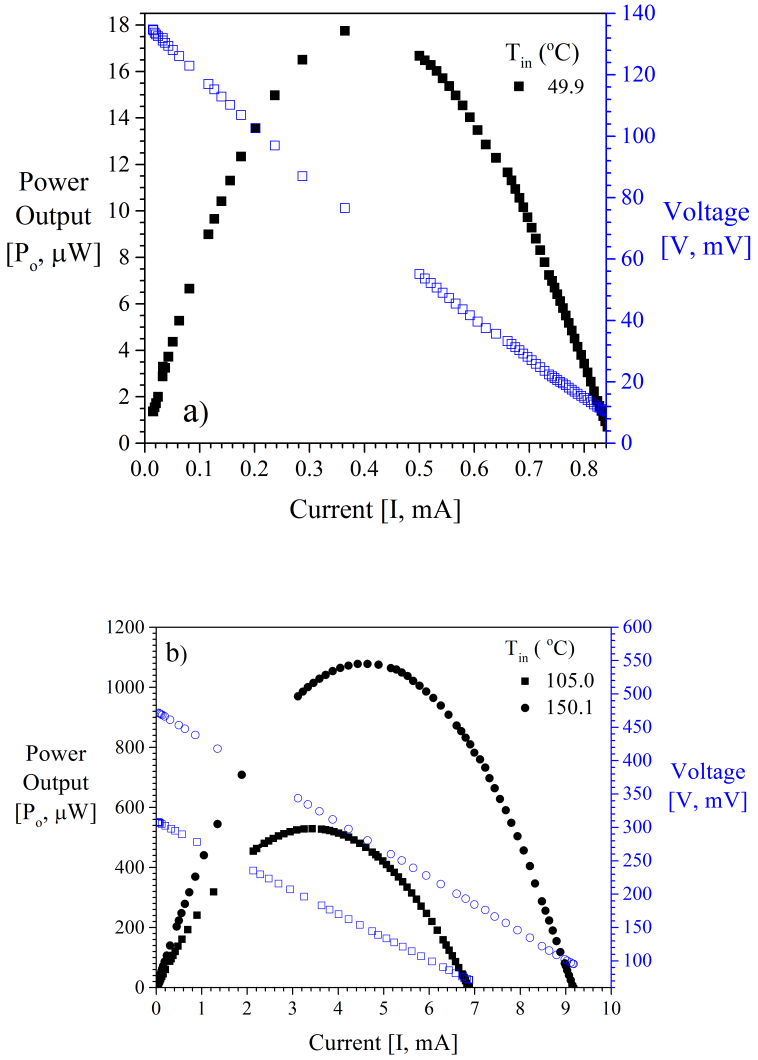

Figure 39: Effect of inlet temperature T_{in} on produced voltage V and current I, and power output P_o of an iTED for a) 49.9 °C and b) 105.0 and 150.1 °C. Hollow symbols correspond to the right y-axis.

5.4.3 Effect of Inlet Temperature and Flow Rate on Efficiency

The efficiency of the device is driven by the temperature differential across the thermoelectric pellets and is a function of Q_h into the device and the materials' intrinsic properties. P- and n-

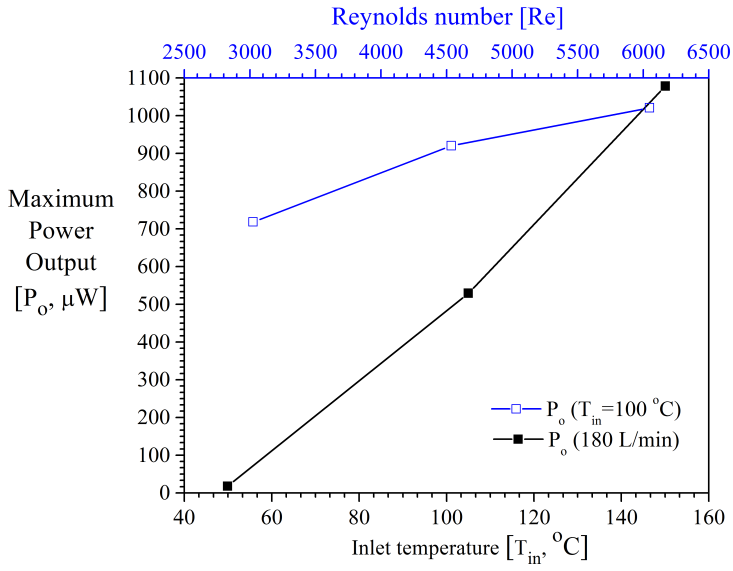

Figure 40: Effect of inlet temperature T_{in} and Re on power output P_o. Hollow symbols correspond to the top x-axis.

type bismuth-telluride semiconductors experience a maximum thermal conversion efficiency when the temperature differential across the element is between 200 and 220 °C [136]. By increasing T_{in}, Q_h increases non-linearly and substantially, from 10.0 to 43.4 and 59.5 W for the 49.9, 105.0 and 150.1 °C cases with a constant flow rate of 180 L/min, respectively, as evidenced in Fig. 43. These values have an uncertainty of ±0.4, ±1.5 and ±1.8 W associated with the respective cases. With a fixed inlet temperature (T_{in}=100 °C), as $\dot{\forall}$ is increased from 100 to 200 L/min by 50 L/min increments (i.e. Re of 3,020, 4,540 and 6,050 respectively), Q_h increases from 34.8 to 60.5 to 91.4 W with an uncertainty of ±0.4, ±0.7 and ±1.0 W respectively, as illustrated in Fig. 43.

For the cases with a constant $\dot{\forall}$=180 L/min and increasing T_{in}, the mass flow rate decreased as T_{in} increased. This was due to decreasing air density with an increase in T_{in}. The temperature difference across the tube banks increased and the Q_h into the device also increased. Additionally, the P_o non-linearly increased with an increase in T_{in} and η of the device linearly increased, as seen in Fig. 44. However, by keeping the T_{in} constant and

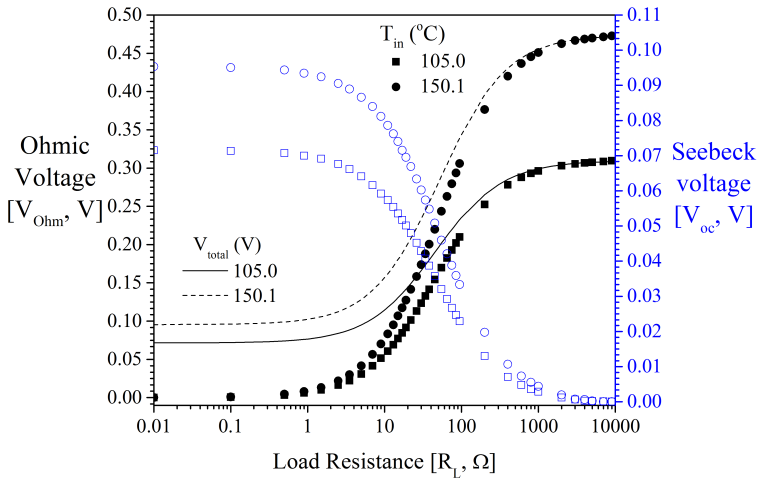

Figure 41: Effect of inlet temperature T_{in} and load resistance R_L on produced Ohmic V_{Ohm} and Seebeck V_{oc} voltages. The total voltage V (expressed as V_{total} in the figure) is the summation of V_{oc} and V_{Ohm}. Hollow symbols correspond to the right y-axis.

increasing $\dot{\forall}$, η of the device decreased. As $\dot{\forall}$ increased, Q_h into the device increased due to increasing the convective heat transfer coefficient as seen in Fig. 43. This resulted in an increased P_o, as seen in Fig. 40. Although Q_h and P_o increased with Re, Q_h increased greater than P_o, which reduced the efficiency of the device, as seen in Fig. 44.

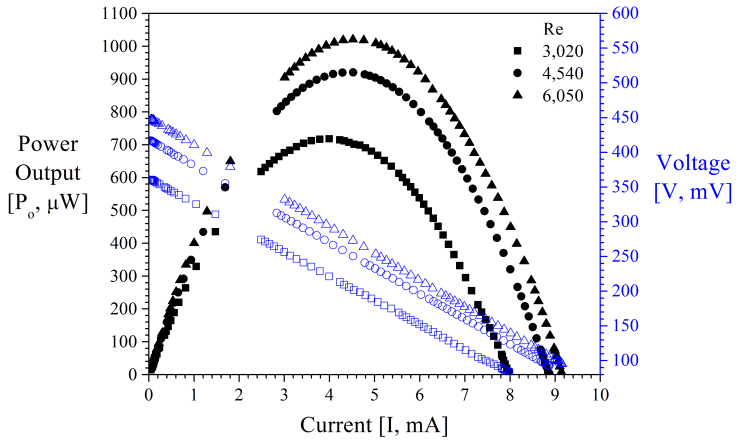

Figure 42: Effect of flow rate in terms of Re on produced voltage, current and power of an iTED. Hollow symbols correspond to the right y-axis.

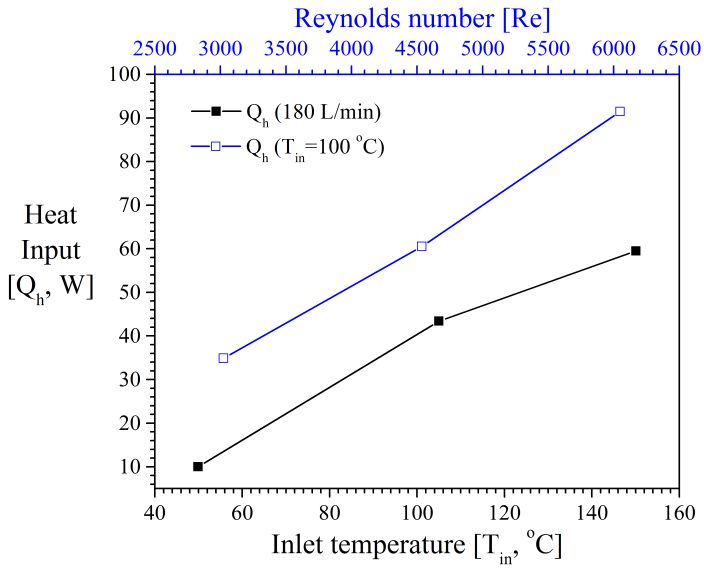

Figure 43: Effect of inlet temperature and Re on heat input Q_h. Hollow symbols correspond to the top x-axis.

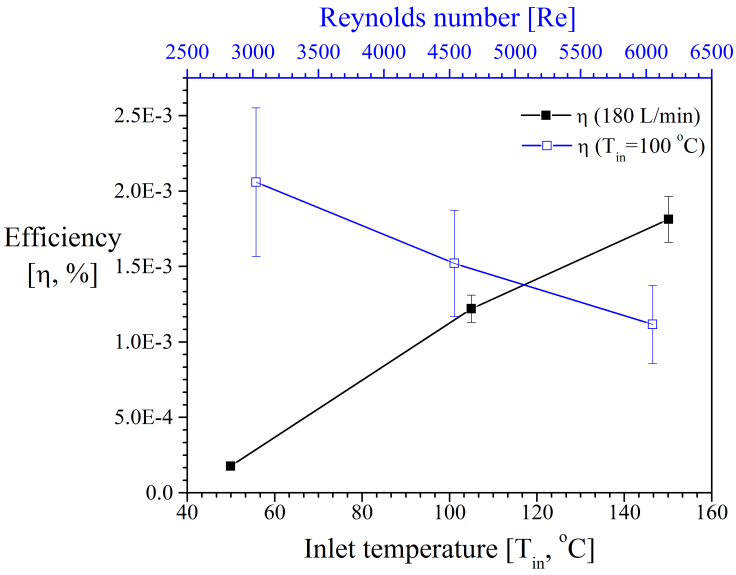

Figure 44: Effect of inlet temperature and Re on efficiency η. Hollow symbols correspond to the top x-axis.

5.4.4 Energy Balance

The flow channel should be well insulated such that the majority of the heat is transferred to the metallic heat exchnagers as opposed to the channel walls. The material selected (NanoTool) for the flow channel has a low thermal conductivity but transfers a substantial amount of heat from the hot fluid and convects it away to ambient as opposed to delivering it to the pellet hot side. Additionally, energy may be lost in the form of Ohmic heating by electrical contact resistances, which decreases I and subsequently P_o. By applying an energy balance to the system (Eq. 5.5), we are able to calculate the energy lost E_{loss} from the system as a function of Q_h and P_o,

$$E_{loss} = Q_h - P_o. \tag{5.5}$$

For all cases, the majority of the energy delivered to the system is lost (≈99%) as a combination of heat escaping through the channel walls, the generation of Ohmic heating

through electrical contact resistances and the inability of by the hot-side heat exchangers to completely extract all the thermal energy from the working fluid. The power output could be increased by either reducing electrical contact resistances, which diminish I, or by increasing ΔT across the TE elements. The temperature difference across the pellets can be increased by increasing the surface area of the hot-side heat exchangers, increasing the hot-side convective heat transfer coefficient h and decreasing the cold-side temperature.

5.4.5 Effect of Load Resistance

To investigate the effects of load resistance on the performance of the iTED, the inlet temperature was maintained at approximately 100 °C (97.7 to 100.4 °C) and the flow rate was increased from 100 to 200 L/min by a 50 L/min increment. The the load resistance R_L was varied between 0 and 9,000 Ω. As R_L increased, V increased from the minimum to the maximum value. However, I decreased from the maximum to the minimum value, as seen in Fig. 45. The maximum P_o occurred when R_L equaled the internal device resistance, R_{in}, as seen in Fig. 46.

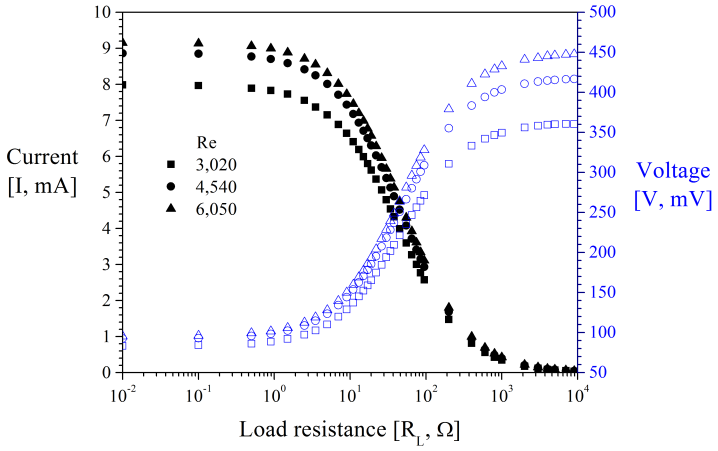

Figure 45: Effect of load resistance R_L on produced voltage V and current I for a constant inlet temperature (T_{in} = 100°C) for various flow rates. Hollow symbols correspond to the right y-axis.

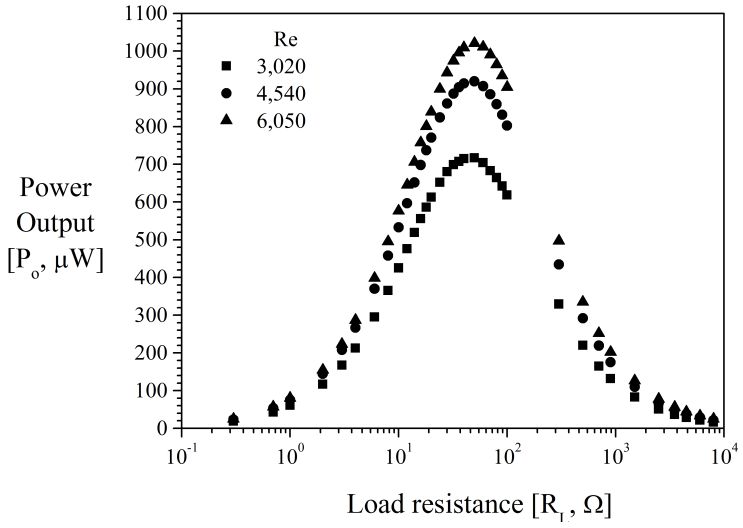

Figure 46: Effect of load resistance R_L on power output P_o.

5.5 CONCLUSION

The performance of an integrated thermoelectric device was studied in terms of produced voltage V and current I, heat input Q_h, power output P_o and conversion efficiency η for various flow rates (3,020$\leq$ Re $\leq$6,050), inlet temperatures (50$\leq$ T_{in} (°C)$\leq$ 150) and load resistances (0$\leq$ R_L (Ω) $\leq$9,000) with a constant cold-side temperature (T_c=20 °C). Performance characteristics and concluding remarks from this chapter are listed as follows:

1. An increase in the fluid inlet temperature T_{in} had a greater effect on the V and I, Q_h, P_o and the η than did an increase in Re. For instance, a 1.4-fold increase in T_{in} (105.0 to 150.1 °C or a 1.5-fold increase in ΔT) resulted in a 1.5- and 1.3-fold increase in V and I, a 2.0-fold increase in P_o, 1.2-fold increase in Q_h and a 1.5-fold increase in η.
2. The power output is proportional to the inlet fluid temperature squared, whereas for a conventional thermolectric device, the power output is near linear with inlet fluid temperature. This indicates the integrated thermoelectric device is capable of a larger power output in comparison to a conventional thermoelectric device with the same geometry

and for the same operating conditions to due decrease thermal resistance between source and sink.

3. For a constant T_{in}, increasing the flow rate resulted in increased thermoelectric performance but decreased efficiency. For instance, a 2.0-fold increase in Re resulted in 1.2-, 1.2-, 1.4- and 2.6-fold increase in V, I, P_o and Q_h, respectively, and a 0.5-fold decrease in η.
4. Increasing the load resistance R_L increases V and decreases I. Additionally, increasing R_L to the value of the internal resistance R_{in} results in maximum power output. This behavior with respect to load resistance is similar to the single-stage iTED and conventional thermoelectric devices.
5. It has been shown experimentally that the effects of T_{in}, Re and R_L have a substantial effect on the thermoelectric performance of an integrated thermoelectric device; increasing T_{in} and matching the R_L to the internal resistance R_{in} results in higher P_o and η.

6.0 UNIAXIAL PRESSING OF BULK BISMUTH TELLURIDE FOR IMPROVED FIGURE OF MERIT

Departing from analytical and numerically modeling techniques introduced in Chaps. 2 and 3, and experimental investigations on novel single- and multi-stage integrated thermoelectric devices introduced in Chaps. 4 and 5, the focus of this chapter is on increasing material performance through material processing techniques. As described in Chap. 2, the thermal conversion efficiency of a thermoelectric device is limited to a maximum dictated by the thermoelectric material's thermal conversion efficiency, expressed in the form of figure of merit. Novel designs are able to increase the power output of a module, however the thermal conversion efficiency will never exceed the maximum of the material used within. Therefore, a multi-faceted approach is necessary to increase device efficiency and power output, and the approach must include material processing.

6.1 INTRODUCTION

From Chap 1, Sec. 1.3, it is evident from literature on CIP and sintering experiments that developing a highly-oriented, anisotropic bulk material with coarse grains should yield a material with low thermal conductivity and electrical resistivity, yielding a large ZT. Contrarily, it was also found through MA, HIP and SPS experiments that small, coherent grains, either uniformly or non-uniformly distributed through the material matrix, act as nanostructures which are able to reduce κ_{ph} without adversely affecting σ, thus increasing ZT [97, 100]; these effects are elaborated upon in great detail [126]. The effect of precursor particle size, compaction pressure, sintering conditions and annealing conditions on the texture and per-

formance of Bi_2Te_3 materials as prepared by CIP and sintering remains unclear. This study quantifies the effects of compaction pressure and annealing time and temperature on the texture of bulk Bi_2Te_3 materials in terms of texture. The texture, as analyzed via diffractograms and the Lotgering factor, will indicate the degree of preferred orientation, as well as crystal size. Samples with the highest degree of preferred orientation are then characterized in terms of thermoelectric performance (α, κ, σ).

6.2 MATERIALS AND METHOD

Samples were prepared using -325 mesh, 99.99% pure bismuth (III) telluride (Bi_2Te_3) powder, CAS number 1304-82-1, provided by Sigma Aldrich, USA. The chemistry was confirmed using XRD. The powder was sieved to between 37-44 μm. The powder was then compacted using an unixial hydraulic press into 6.375 mm diameter and 0.4-0.5 mm thick pellets using a die (MTI, EQ-Die-06D). The die rod surfaces were polished with 0.05 μm alumina powder. To verify that the effects of compaction pressure (P_c) were independent of the die set used, two additional sets of powder were compacted using a 12.7 mm die (MTI, EQ-Die-12D) and an in-house 13.564 mm die made from water-hardened tool steel. Both were polished to a 0.05 μm finish. The samples were compacted using a hydraulic press (MTI, EQ-YLJ-12T) ranging from $100 \leq P_c \leq 2{,}040$ MPa, under ambient conditions. Each pellet was held at pressure for at least 5 minutes.

After uniaxial pressing, additional samples were compacted at the pressure associated with the highest preferred orientation as determined by the Lotgering factor. These were annealed at temperatures ranging from 0.3-0.8 of the melting temperature T_m of Bi_2Te_3 (585 °C) for 3-96 hours in an Ar-flooded, vacuum-environment quartz tube placed in a vacuum furnace (MTI, EQ-DZF-6020-HT500P). The furnace was evacuated to a pressure of $\leq$133 pa and Ar was flowed through at a rate of 200 mL/min as an additional measure to prevent any possible oxidation. During sintering, the heating and cooling rate was set to 1 °C/min.

X-ray diffraction (XRD) patterns were obtained by using a PanAlytical Empyrean system with a cobalt source. Two-theta (2θ) measurements ranged from 5 to 85 degrees with a step

size of 0.002 degrees. A zero-diffraction disk (MTI, SiZero24D05C1) was used with the 6.35 mm samples to eliminate peaks associated with the sample stage. The XRD data was recorded using PanAlytical Data Collector software and analyzed using PanAlytical HighScore software. 2θ peaks and d-spacing were compared to published data, as listed in Results and Discussion. The density of compacted and sintered samples were determined using the Archimedes method. Surface finish and grain sizes were characterized using a Keyence VHX-600 digital microscope. To view grain boundaries, the samples were polished using a silica and etched with a solution of 30% nitric acid in water. ZT measurements were conducted by Temte Inc. [164].

Temte Inc. developed a novel Two Sample Calibration System (2SSC) that utilizes bi-polar transient Harman-based measurements methods. The system simultaneously measures electrical resistivity, thermal conductivity and the Seebeck coefficients over a range of temperature differences. The developed method accounts for heat loss from the sample to surroundings via conduction and radiation heat transfer. This is done by relating the Peltier heat to the inverse of the thermal conductance and total equivalent thermal conductance of all parasitic thermal phenomena. The accuracy of the Seebeck coefficient, electrical resistivity and thermal conductivity measurements are $\pm 0.5\%$, $\pm 1.0\%$, and $\pm 1.0\%$, respectively, with the figure of merit reportable to $\pm 1.0\%$.

An in-house code was developed to find, isolate and measure the area of grains within the resolution of the optical imaging system. The optical micrograph was thresholded incrementally between zero and 255, with the binary values of each thresholded image summed up per integer. The total sum was compared to the previous sum, creating a residual versus threshold curve. The global minimum, or second-derivative of the polynomial fit of the threshold curve, fitted with least error, yielded the optimum threshold value. The optimum image was then median filtered and any grains less than an area specified by the resolution squared were removed, as well as all grains touching the image edge. To separate grains connected by image artifacts, a connectivity algorithm was implemented in the x- and y-directions to eliminate pixels that did not satisfy the specified number of connections as per resolution via a method of contraction and dilation. The border of each grain was determined by a boundary-trace algorithm, from which the area of the grain was determined. This is demon-

strated in the figures below. Figure 47a illustrates the original optical image, Fig. 47b of the binary image of the original and Fig. 47c of the segmented grains.

6.3 RESULTS AND DISCUSSION

6.3.1 Effect of Compaction Pressure

The compaction pressure ranged from 100 to 2,040 MPa. The samples were analyzed via XRD to evaluate the peak integral area intensities via the Lotgering factor F; F indicates the degree of preferred orientation of the $(00l)$ planes such that

$$F = \frac{P - P_o}{1 - P_o}. \tag{6.1}$$

The variable P is defined as

$$P = \frac{I(00l)}{\sum I(hkl)} \tag{6.2}$$

where $I(00l)$ and $\sum I(hkl)$ are the peak integral intensities of all $(00l)$ and (hkl) planes for the sample with supposed preferred orientation, respectively. The variable P_o is defined as

$$P_o = \frac{I_o(00l)}{\sum I_o(hkl)} \tag{6.3}$$

where $I_o(00l)$ and $\sum I_o(hkl)$ are the peak integral intensities of all $(00l)$ and (hkl) planes for the randomly oriented sample (i.e. the non-compacted powder). As F approaches unity, the sample of interest approaches complete preferred orientation. The orientation of interest is the $(00l)$ family, which indicates the covalent bonds between the Bi-Te$^{(1,2)}$ quintet are orientated perpendicular to the basal plane (pressing direction).

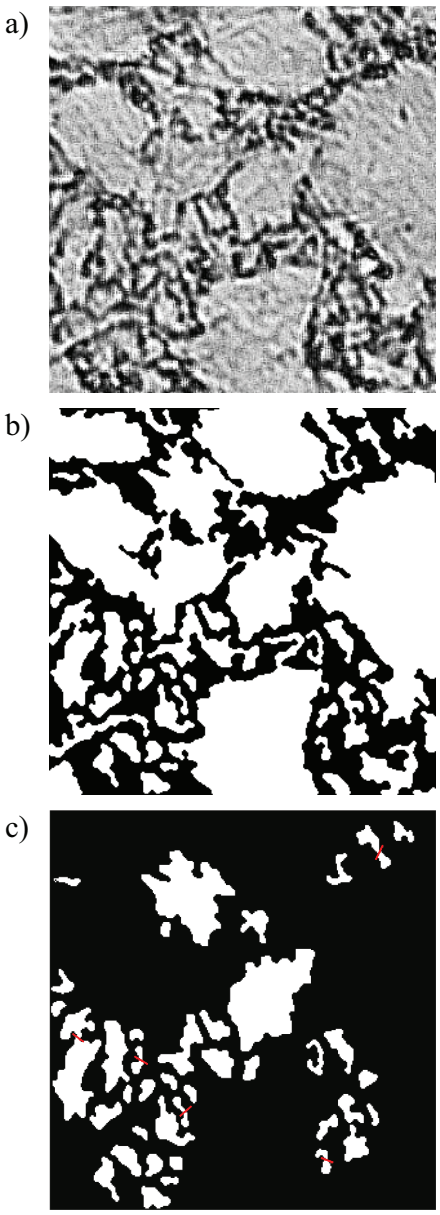

Figure 47: Representative optical images of a) grains before processing, b) binary image of grains after thresholding and median filtering and c) binary image of grains after segmentation and removal of grains below size threshold and those on image boundary. The small red lines between grains on panel c) indicate the break of a grain into two separate grains.

Powder diffraction requires a particle size of less than 10 μm; however the starting powder size used within the experiments was 37-44 μm (-325 mesh). Therefore, to determine P_o, both a sub-10 μm (as prepared via mechanical alloying (MA)) and 37-44 μm powder were examined. The difference of P_o values between the sub-10 and 44 μm powders was less than 9.6%, indicating no major change between the two powders. The P_o was determined to be 0.22±0.03 from the the sub-10 μm powder with a 95% confidence interval.

Figure 48 illustrates the effect of P_c on the normalized intensity peaks for all compacted samples. The baseline powder exhibits high-intensity for the (0,1,5) and (1,0,10) peaks, as illustrated in Figs. 48a-c. A slight increase in compaction pressure (100 MPa) drastically increases the (0,0,3), (0,0,6) and (0,0,15) peaks and a reduction in the (0,1,5), (1,0,10), (0,1,11) and (1,1,0) peaks. Plastic deformation as a results of an increase in P_c breaks the weak van der Waal bonds between $Te^{(1)}$-$Te^{(1)}$ atoms, causing crystals to cleave; as the pressure increases, all peak widths increased indicating either the formation of small grains, increased misorientation strain, or the introduction of defects. When P_c=1,490 MPa, the Lotgering factor F, as expressed by Eqn. 6.1, was at the highest value of 0.55±0.04 as illustrated by Fig. 49. These samples yielded statistically significant results (95% confidence interval) and indicated the PCO of (00l) was greater than 50%. It is evident from Fig. 49 that as P_c increases, F exponentially increases and plateaus around 50-55%; an increase in P_c above 800 MPa did not increase F further.

With an increase in P_c, the density of the material exponentially increases, as illustrated in Fig. 50. When P_c exceeds 1,540 MPa, the samples have a density >99%. Examining the surface of the compacted samples, the surface finish becomes smoother and less porous as a result of increasing compaction pressure, as seen in Fig. 50b, indicating a more dense sample.

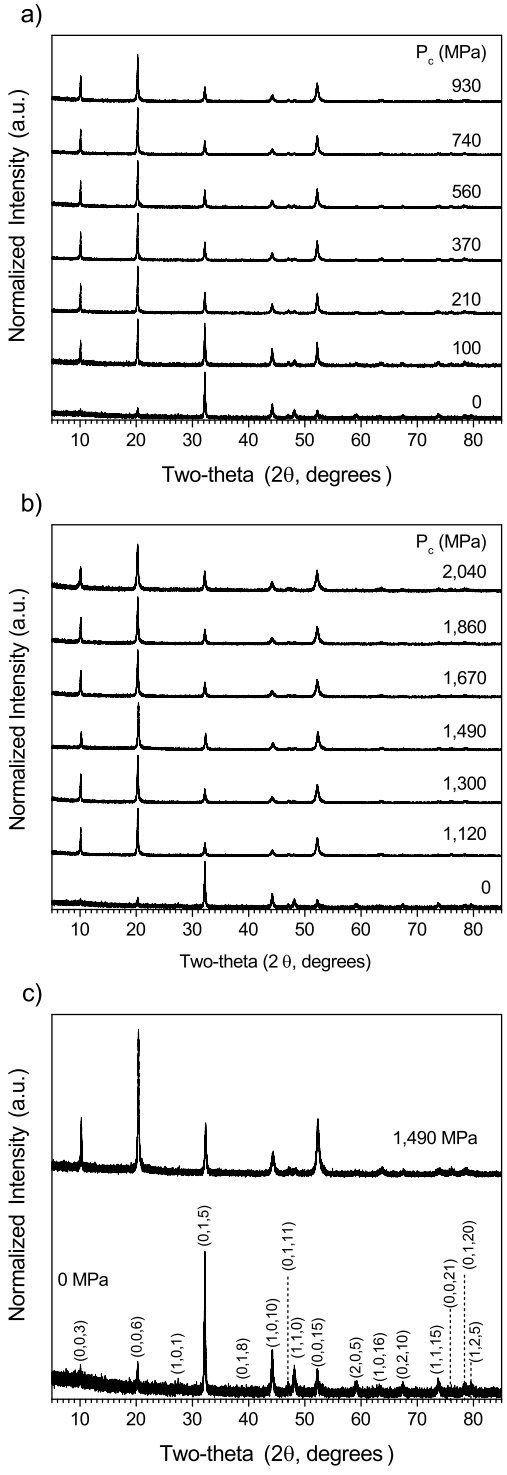

Figure 48: Diffractograms of a) 0 through 930, b) 0 and 1,120 through 2,040 and c) 0 and 1,490 MPa P_c samples, with the latter yielding the highest Lotgering factor.

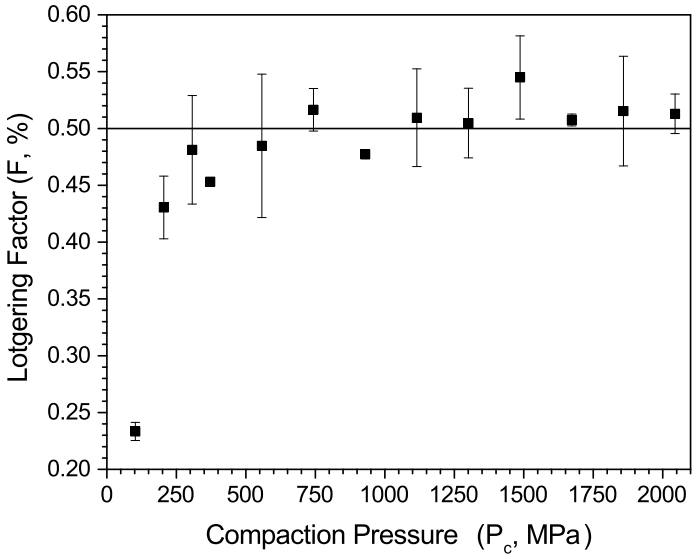

Figure 49: Lotgering factor F versus compaction pressure (P_c, MPa) expressed with 95% confidence interval based upon standard deviation.

It is evident that an increase in P_c yields a drastic change in the microstructure of the sample, as evidenced in Fig. 51. Samples were characterized by imaging a 300x225 μm area and over 2,000 individual grains were analyzed. Analyzing the grain size distribution of samples prepared at 370, 930, 1,490 and 2,040 MPa indicates a constant grain size, in both mean grain size and area; for instance, the mean grain sizes and areas were 39.5±2.1, 30.0±2.2, 44.6±3.10 and 46.2±3.0 μm^2, respectively. The grain size distributions for the 370 and 2,040 MPa samples indicate there is no substantial change, as evidenced by Fig. 51. This trend indicates that increasing P_c did not cleave existing grains, rather introduced defects and intergrain strain.

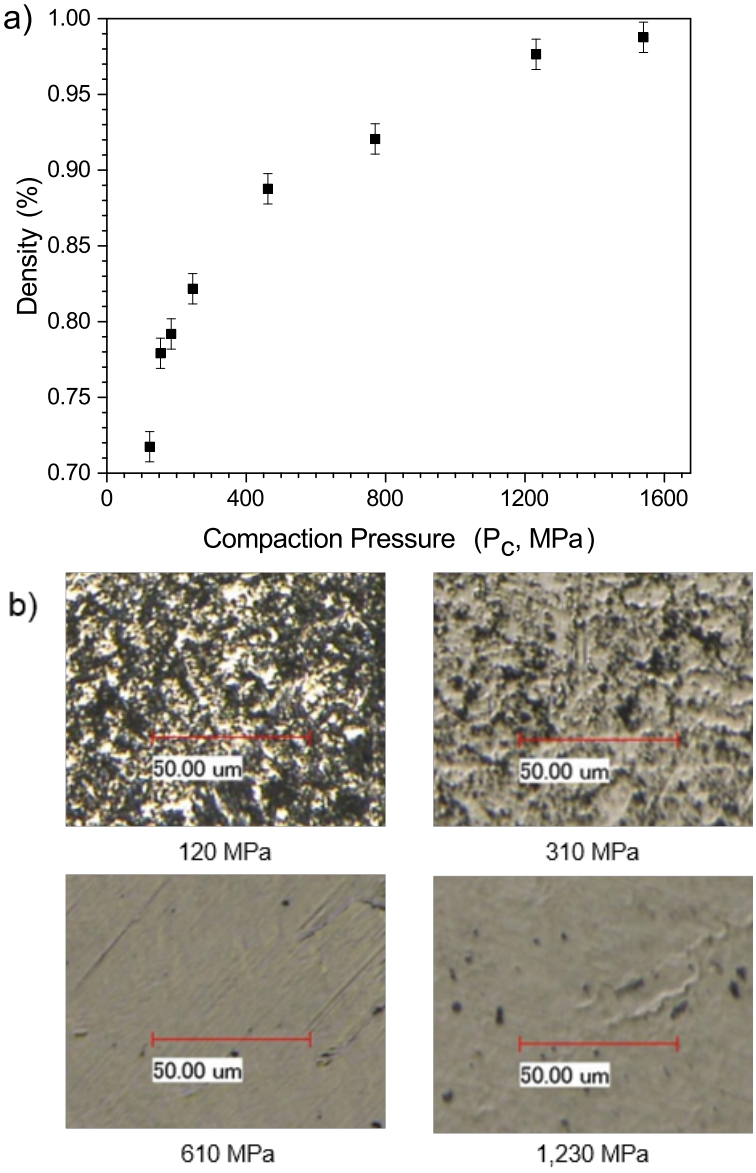

Figure 50: Measured a) density of cold isostatic pressed samples as determined by the Archimedes method and b) optical micrographs of sample surfaces for various P_c values.

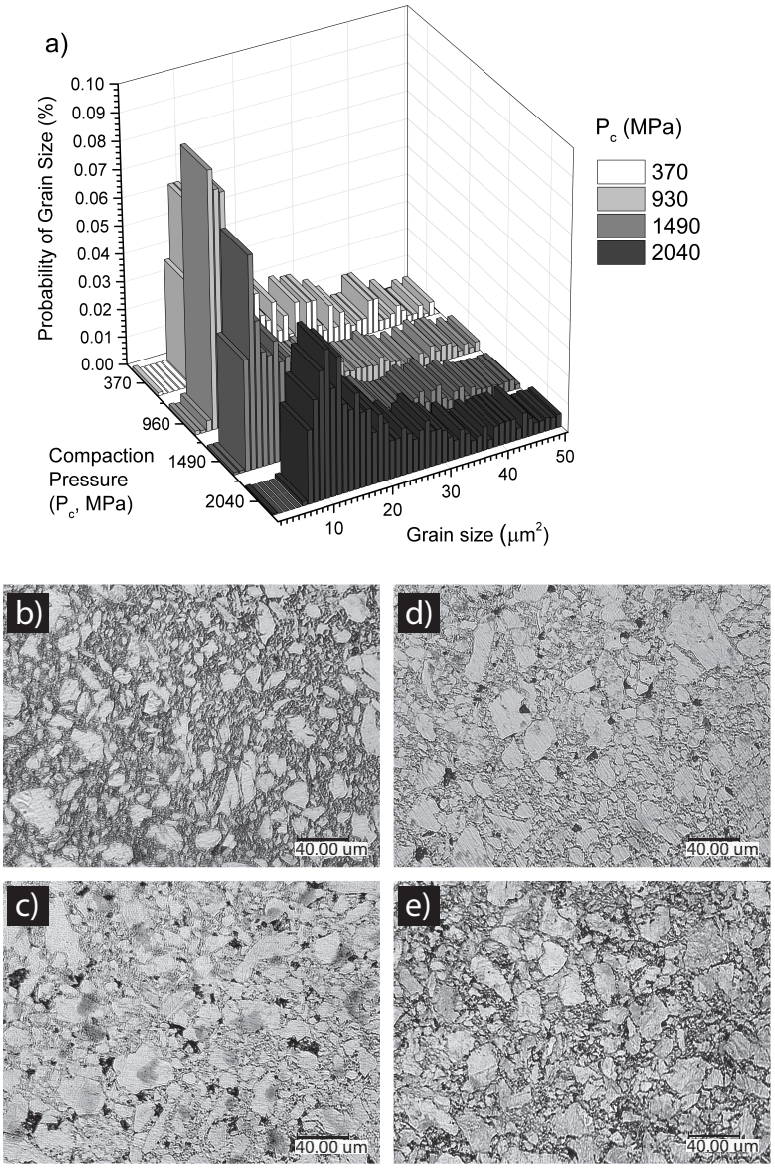

Figure 51: a) Grain size distributions and optical micrographs of samples compact at a compaction pressure of b) P_c=370, c) P_c=930, d) P_c=1,490 and e) P_c=2,040 MPa.

6.3.2 Effect of Sintering Time and Temperature

Since P_c=1,490 MPa yielded samples with the highest F value, said samples were used for an annealing study. Samples with an F above 50% should be thermodynamically stable during annealing, i.e. at certain annealing temperatures (less than 50% of T_m) there should be no temperature-induced static recrystallization, in which the grain boundaries reassemble and reorient itself due to the releases of stored interfacial energy introduced during compaction. Figure 52a illustrates the effect of T_{ann} on the peak intensity of samples annealed for 6 hr. As T_{ann} increase from 0.3-0.8 T_m, the relative intensity of the (00l) families decrease with a marked increase in the (0,1,5), (0,1,11) and (1,1,0) peaks.

It is evident from Fig. 52a that increasing the T_{ann} narrows the diffractogram peaks, indicating the growth of coarse grains and the release of strain energy imparted by compaction, with the former being explained in the proceeding paragraph. The effect of T_{ann} on the diffractogram peak widths and intensities is not fully seen until $T_{ann} \geq$0.5 T_m. Additionally, the release of strain energy changes the texture of the sample. Figure 52b represents the F values of annealed samples; it is evident when T_m is greater than 0.5, the material begins to lose the preferred texture due to static recrystallization brought on by elevated annealing temperatures.

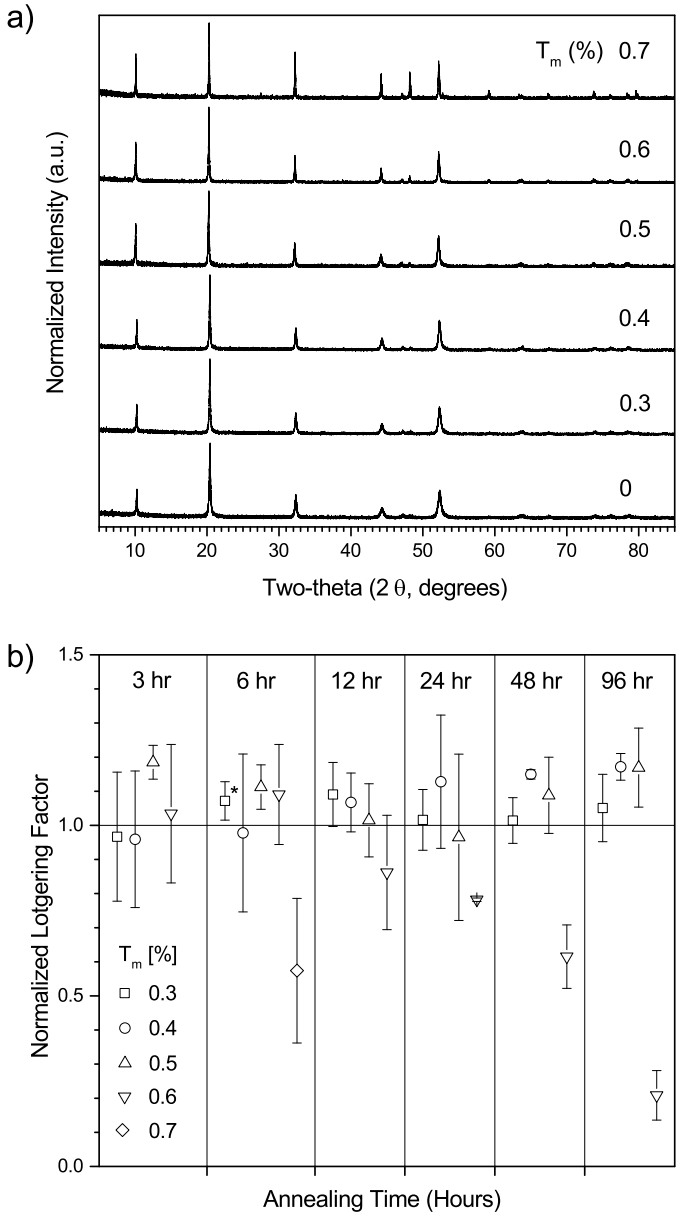

Figure 52: Diffractograms of a) 6 hour-annealed samples (P_c=1,490 MPa) for various percentages of Bi_2Te_3 melting temperature (0.3-0.8 T_m), b) Lotgering factor of aforementioned annealed samples versus annealing time for various T_m.

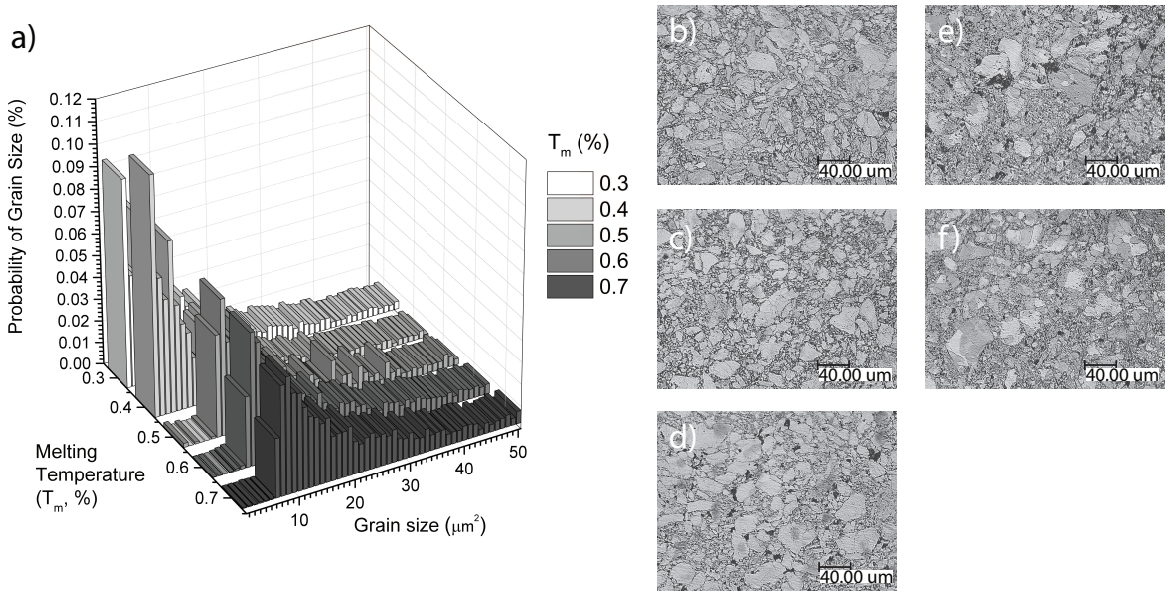

Figure 53: a) Grain size distributions and optical micrographs of b) 0.3 T_m, c) 0.4 T_m, d) 0.5 T_m, e) 0.6 T_m and f) 0.7 T_m samples annealed for 6 hour annealing.

Figure 53 shows the progression of microstructure with an increase in T_{ann} via grain size distributions and optical micrographs. As T_{ann} increases from 0.3 to 0.4 T_m, the average grain size remains nearly invariant. For the 0.3 and 0.4 T_m samples, the average grain sizes are 26.8±1.7 and 22.2±1.0 μm^2, respectively. From 0.5 T_m onward, the grains begin to recrystallize and coarsen, with the average grain size being 50.5±5.3, 40.5±1.5 and 48.0±2.2 μm^2 for the 0.5, 0.6 and 0.7 T_m cases, respectively. In addition to an increase in average grain size, the size distributions shifts to the right, indicating the formation of large grains without the presence of smaller, finer grains. This trend is substantiated by the grain size distributions and optical micrographs, as seen in Fig. 53. Furthermore, this trend is explained by defects within the sample introduced during plastic deformation. A sample with high defect density can retard the growth of grains, hence no major recrystallization takes place at 0.3 and 0.4 T_m. At 0.5 T_m, temperature induced recrystallization promotes grain boundary reassembly and reorientation due to the release of stored interfacial energy introduced during plastic deformation as evidenced by the reduced texture (Figs. 52b).

6.3.3 Figure of Merit

The figure of merit was determined by the 2SSC method proposed by Temte Inc. which simultaneously determines the Seebeck coefficient and electrical and thermal conductivities with low error (less than 1%) [164]. Figures 54a-c represent the temperature-dependent thermal and electrical conductivities, Seebeck coefficient and ZT, respectively of samples compacted at 1,490 MPa, annealed for 96 hours and for various annealing temperatures ($0.3 \leq T_m$ (%)≤ 0.7). It is evident from Fig. 54a that increasing the annealing temperature above 0.5 T_m drastically reduces the electrical resistivity over the entire temperature range of interest. Above 0.5 T_m, the sample reduces thermodynamic stability and strain energy, which was imparted during compaction, is released, conducing the formation of coherent grain boundaries. Samples annealed at 0.7 T_m exhibit an electrical resistivity an order of magnitude that those annealed at 0.3 T_m. The thermal conductivity increases with an increase in T_m due to the formation of larger grains via static recrystallization, as evidenced by average grain size and grain size distributions (Fig. 53).

The Seebeck coefficient becomes more negative with an increase in T_m and remains relatively constant per temperature as seen in Fig. 54b. The thermopower, evaluated as the Seebeck coefficient squared times electrical conductivity, indicates the sample annealed at T_m=0.6 has a substantially larger values for all tested temperatures by an order of magnitude, as seen in Fig. 55. The increase in electrical conductivity is attributed to increase in mean free time between scattering collisions at grain boundaries. The charge carrier density, charge per carrier and carrier mass should be invariant between samples.

It is noted that although the target temperature T often exceeded the annealing temperature T_{ann} of the samples during thermoelectric characterization, the effect of T on crystallography and subsequent performance is minimal. In reference to Fig. 52b, it took a minimum of six hours of annealing to begin to degrade the texture of the sample. The determination of the thermoelectic properties took six minutes per specified temperature. The testing time was two orders of magnitude less that what was necessary to cause a change in texture, thus is inconsequential.

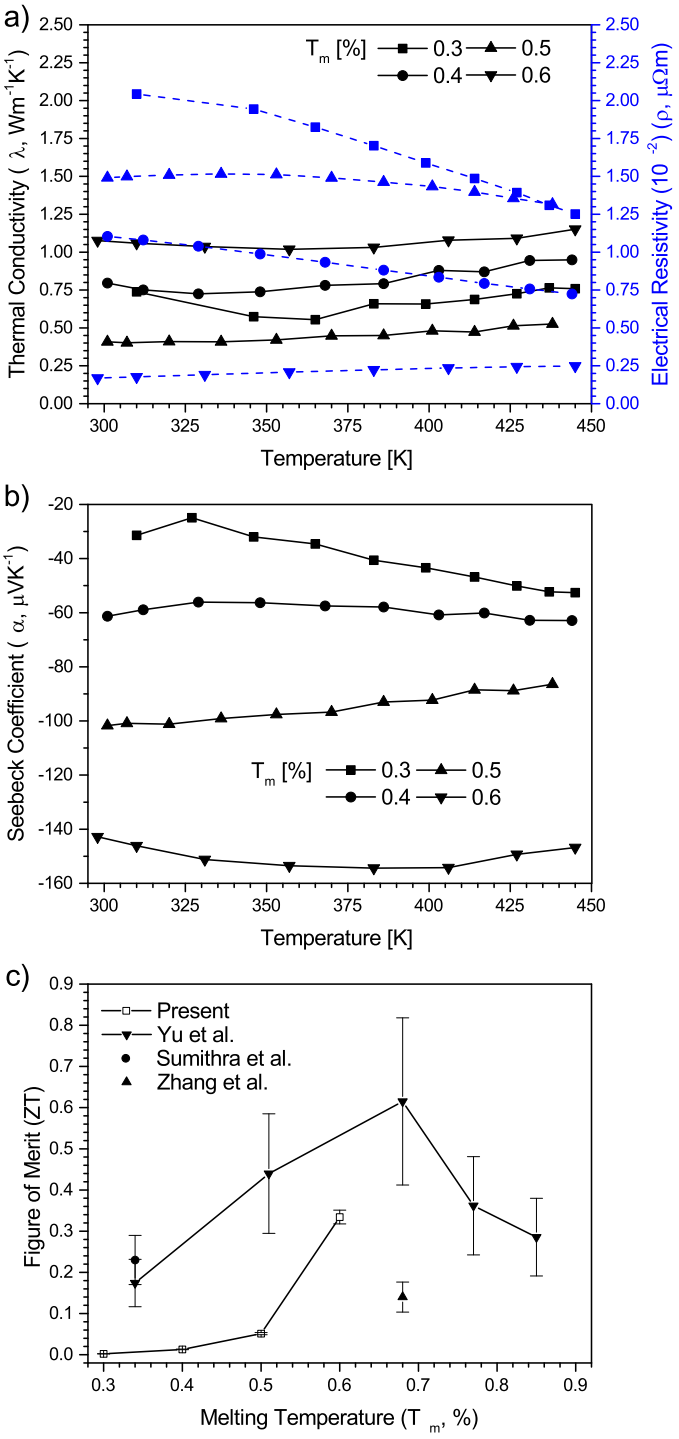

Figure 54: Temperature-dependent a) thermal and electrical conductivities, b) Seebeck coefficient and c) Figure of Merit evaluated at 300K for present work in comparison to Yu et al. [97], Sumithra et al. [165] and Zhang et al. [166] for samples prepared at P_c=1,490 MPa and at various annealing temperatures. The dotted lines in a) correspond to the right-side axis.

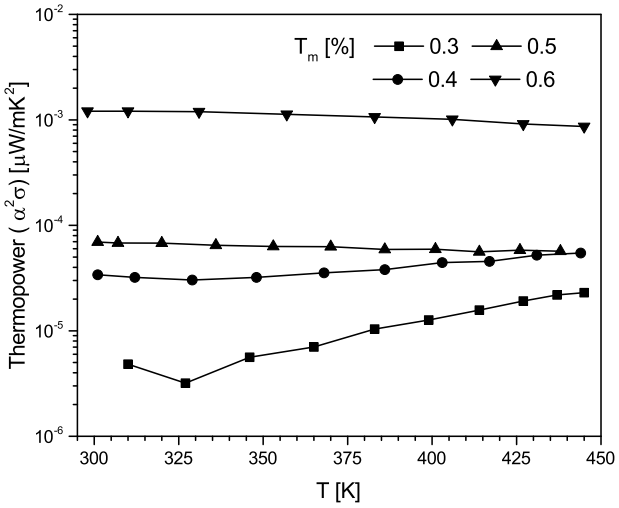

Figure 55: Thermopower of samples prepared at various annealing temperatures per tested temperature.

The figure of merit increases with an increase in T_m as seen in Fig. 54c, with the maximum achieved at 0.6 T_m. The increase in λ is outweighed by the increase in magnitude of α and decrease in ρ with an increase in T_m (i.e. thermopower), resulting in a substantial improvement in ZT. It is noted that the values presented in Fig. 54c from literature for comparison reflect those of nanocrystalline (20-180 nm) Bi_2Te_3 prepared by high-energy mechanical alloying[97], mechanically-alloyed and hot-pressed Bi_2Te_3 [97] and aqueous chemical method hot-pressed Bi_2Te_3 [166]. Error for ZT measurements in Fig. 54c was calculated based upon accuracy values reported in manufacturer literature per equipment used by author in respective source.

The presented method yields comparable results with less energy-intensive preparation procedures and less temperature-sensitive properties than comparable methods. The figure of merit for the 0.6 T_m sample versus temperature is shown in Fig. 56. It is noticed that ZT is maintained over a large temperature range and a maximum value of 0.40 is achieve at 383 K, comparable to the results obtained by Sumithra et al. [165].

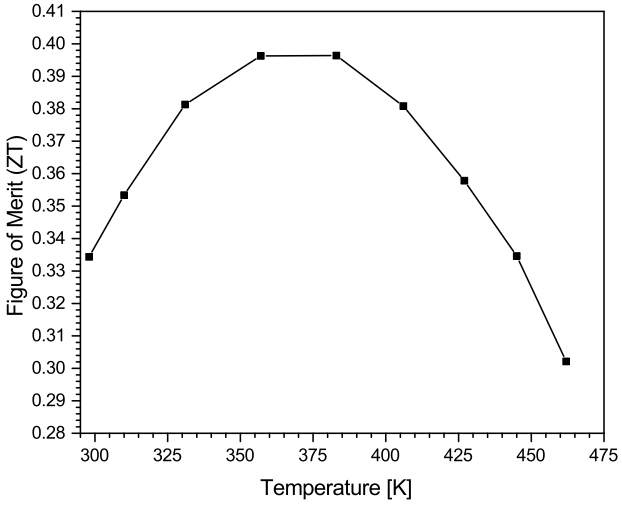

Figure 56: Temperature-dependent figure of Merit of sample prepared at P_c=1,490 MPa and 0.6 T_m for 96 hours.

It is evident that the maximum thermoelectric performance is achieved at a higher annealing temperature. The increase of ZT is linked with the emergence of a secondary preferred crystallographic orientation. Originally, the $(0, 0, l)$ family emerged as the PCO during compaction. During sintering, that PCO was destroyed due to temperature induced static recrystallization and the release of intergrain strain energy. Comparing the summation of the all other possible families $(h, k, 0)$ and $(h, 0, l)$ to the deteriorating $(0, 0, l)$ family indicates the emergence of a stronger, secondary PCO, as seen in Fig. 57. The $(0, 0, l)$ family decreases above 0.6 T_m whereas the $(h, k, 0)$ and $(h, 0, l)$ families increase above 0.6 T_m.

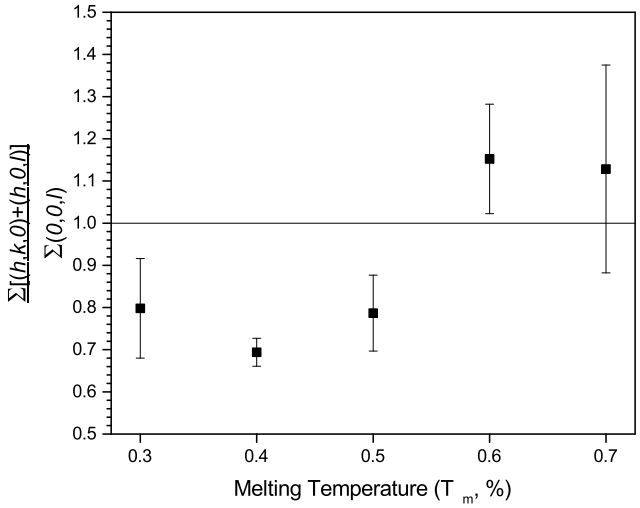

Figure 57: Comparison of summation of (h,k,0) and (h,0,l) families to original PCO of (0,0,l) per annealing temperature T_m.

6.4 CONCLUSIONS

A systematic study was conducted to determine the effect of compaction pressure ($100 \leq P_c$ (MPa)$\leq$2,040), annealing time ($3 \leq T_{ann}$ (hr)$\leq$96) and temperature ($175 \leq T_{ann}$ (°C)$\leq$468) on the preferred crystallographic orientation (PCO), texture and thermoelectric performance, in terms of the Seebeck coefficient, thermal and electrical conductivity and figure of merit on bismuth telluride (Bi_2Te_3) semiconductor. The key finds are presented in the following:

1. It was found an increase in P_c up to a value of 1,490 MPa resulted in an increase in PCO as seen by an increase in the $(00l)$ family as evidenced by a high Lotgering factor of 0.55±0.04; additionally, increasing P_c broadened the intensity peaks of samples as measured by X-ray diffraction, indicating an increase in intergrain strain as opposed to the formation of small grains, as evidenced by optical micrographs and EBSD.

2. Increasing T_{ann} up to 0.5 T_m densified the sample without causing a change in texture; above 0.5 T_m, the sample loses PCO due to the onset of static recrystallization through the releases of stored intergrain energy. The release of intergrain strain conduces the formation of coherent grains which exhibit favorable thermoelectric properties (i.e. low electrical resistivity).
3. Additionally, increasing T_{ann} up to 0.6 T_m increased the magnitude of the Seebeck coefficient, reduced the electrical resistivity and increased the thermal conductivity, yielding marked improvements in the thermopower term and ZT values. Although the thermal conductivity increased with increased T_{ann} due to the growth of larger grains via temperature induced static recrystallization, the increase in thermopower far exceeded that of the thermal conductivity. A maximum ZT value of 0.4 was achieved at 383 K for bulk Bi_2Te_3.
4. The increase in ZT with increasing T_{ann} is linked to the emergence of a secondary PCO. The secondary PCO is a result of temperature induced static recrystallization and the release of intergrain strain energy once T_{ann} exceeds 0.5 T_m. The secondary PCO indicates the emergence of $(h, k, 0)$ and $(h, 0, l)$ families in larger percentages than the original $(0, 0, l)$ family.

7.0 CONCLUSIONS AND FUTURE WORK

This dissertation took a multifaceted approach to increase thermoelectric device performance. To increase device performance, device modeling and design, as well as material processing must be pursued. The first approach was to model thermoelectric devices using a one-dimensional thermal resistance network. This approach had two main objectives. The first objective was to introduce a co-optimization algorithm of thermoelectric material geometry to maximize thermal conversion efficiency and power output based upon realized temperature difference across the thermoelectric junction as a result of experience operating conditions. The second objective was to identify areas of thermal restriction that could be modified or removed to increase material performance. From the employed modeling, a sub-objective was introduced, and that was the resolution of radiation view factors within thermoelectric devices, as presented in Chap. 3. The findings in Chap. 2 were the foundation for the second approach to increasing device performance; the introduction of the integrated thermoelectric device, which was studied experimentally as presented in Chaps. 4 and 5. Furthermore, building upon device modeling and design, the third approach to increasing device efficiency through increasing material efficiency was introduced in Chap. 6. In regard to the presented material, several major contributions have been made as summarized in the following.

7.1 PRIMARY CONTRIBUTIONS

7.1.1 Optimization of TE Material for Improved TED Performance

A complete one-dimensional thermal resistance network of a thermoelectric device was developed, and within, a geometric optimization algorithm was introduced to co-optimize thermoelectric material geometry to maximize thermal conversion efficiency and power output. The formulation of the co-optimization algorithm was based upon the optimization of cross-sectional areas presented by Angrist [136], but was rederived to take into account optimization of length and included area-dependent thermal and electrical contact resistances associated with interfacial bonding material. The presented model was validated with previously published numerical and analytical models. Results indicate optimized geometries are able to achieve substantially higher power densities, on the order of 29%, and volumetric efficiencies, on the order of 22%, in the presence of thermal and electrical contact resistances in comparison to non-optimized geometries.

7.1.2 Resolution of Radiation View Factors with TED

A point of contention in analytical and numerical modeling of thermoelectric devices is the resolution of radiation heat transfer within the thermoelectric device cavity; for low-grade waste-heat recovery devices, it is often accepted to ignore radiation heat transfer due to the complexity of resolving the radiation view factor F_{ij}, however for medium- and high-grade waste-heat recovery devices it is imperative to resolve radiation heat transfer. To address this stated need, direct numerical resolution of F_{ij} for the two primary participating surfaces within a thermoelectric device, the cold- and hot-side ceramics as determined by maximum temperature and emissivity values, was accomplished for a variety of device configurations reflecting various packing densities, height-to-width ratios expected for power generation devices and interconnector thicknesses. The numerical modeling took into the shadow effect produced via interconnector and thermoelectric material geometry via a point-in-polygon algorithm. Additionally, the numerical modeling was extended to hybridized CPU-GPU computing to allow for the rapid solution of high-density grids yielding acceptable residuals.

Results were found to be numerically convergent through the evaluation of the Grid Convergence Index. It was found F_{ij} exponentially decays with packing density and behaves non-linearly with an increase in leg height and interconnector thickness.

7.1.3 Novel Device Design: The Pin-Fin Integrated Thermoelectric Device

Increasing thermoelectric device performance relies on either increasing material efficiency or restructuring the device to allow for the establishment of a larger temperature difference across the thermoelectric material, thus increasing power output. To this end, two novel device designs, the single-stage and pin-fin multistage integrated thermoelectric device, were proposed and tested, with the performance characteristics being quantified for each. The benefits of the integrated thermoelectric device were demonstrated, that is, the reduction in thermal resistance between source and hot-side junction, resulting in unique performance characteristics. The integrated thermoelectric devices exhibit a non-linear increase in power output with increasing fluid inlet temperature, whereas a conventional thermoelectric device exhibits a near-linear increase in power output with increasing hot-side fluid temperature. Thus, the integrated thermoelectric device has improved thermoelectric performance in terms of produced voltage and current and subsequently determined power output in comparison to a conventional device. Additionally, the integrated thermoelectric device was developed in a manner that utilized additive manufacturing.

7.1.4 Effect of Crystallographic Orientation on Figure of Merit

Various methods of material processing have been pursued to capitalize on the anisotropy of thermoelectric materials to improve performance. Attention was focused to the key processing parameters that are responsible for controlling the crystallography and subsequent performance of thermolectric materials, namely compaction pressure and sintering time and temperature. Unaxial compaction studies presented asymptotically increasing trends of degree of preferred crystallographic orientation (PCO) with an increase in compaction pressure. Sintering time and temperature studies provided trends between grain size and size distributions and orientation; increasing annealing time strengthened the texture whereas increasing

annealing temperature above 50% material melting temperature destroyed imparted PCO and facilitated in the formation of large grains. Samples with the highest PCO as prepared by unaxial compression were then sintered at 96 hours between 30% and 60% of the material melting temperature. Above 50% melting temperature, a secondary PCO emerged through the release of intergrain strain energy and temperature induced static recrystallization. It was found ZT exponentially increases with annealing temperature and a maximum ZT of 0.40 could be achieved at 383 K for bulk Bi_2Te_3.

7.2 FUTURE WORK

The work presented within this dissertation definitively answered select questions regarding thermoelectric device modeling and design, and thermoelectric material processing. However, as with all research, answering one question often leads to many newer questions. Questions that arose during this dissertation would be suitable topics of future work as identified and described in the following.

7.2.1 Complete Radiation Modeling of TED Cavity

The presented method of numerically resolving the radiation view factor between two surfaces within a thermoelectric device cavity provided reasonable values that could be included within analytical models. However, it is apparent there is a need to determine all the radiation view factors for all participating surfaces within a thermoelectric device cavity. For instance, determining F_{ij} between the hot-side ceramic and hot- and cold-interconnectors and thermoelectric element legs, as well as the like for the cold-side interconnector and thermoelectric element legs, would provide all necessary information to quickly and accurately model all radiation heat transfer interactions with a given TED cavity. To this end, another question arises; why is modeling limited to a unit cell, but rather a complete device with hundreds of p-n junctions and actual device boundaries? Therefore, future studies on the determination of F_{ij} within a complete thermoelectric device would be apposite. Such a

study would require the extrapolation of the present numerical code to more parallelizable languages, such as OpenCL or CUDA, to take advantage of multi-GPU clusters; utilizing multi-GPU clusters would allow for larger models to be solved in lesser time. The interactions determined per device could be implemented within numerical models prior to CPU computation, allowing for accurate determination of radiation heat transfer without the time-intensive process of resolving F_{ij} per surface.

7.2.2 Integrated Thermoelectric Device Design

The single-stage and subsequent pin-fin integrated thermoelectric devices demonstrated a viable novel device design that allows for greater performance per given operating conditions in comparison to conventional thermoelectric devices. The pin-fin integrated thermoelectric device allowed for the implementation of additive manufacturing to construct the device support structure. Therefore, a pertinent avenue of future study would be the development of the pin-fin integrated thermoelectric device to incorporate turbulence inducing features within the support structure, as well higher-packing density modules. More specifically, turbulators could be printed on the support structure's interior walls to promote downstream turbulence, thus increasing hot-side convective heat transfer coefficients on the hot-side heat exchangers. Moreoever, after the determination of optimal thermoelectric material geometry to maximize power output per given flow conditions, the pin-fin geometry could be modified in such a manner to allow for a higher packing density (i.e. dog-boned) and even include features to promote turbulence and heat transfer (i.e. threading, pitting, etc.). The proposed device design is novel in nature and requires substantial development before the full potential of benefits are realized.

7.2.3 Precursor Particle Size, Grain Boundary Motion and Figure of Merit

Much attention has been devoted to nanostructuring thermoelectric materials to phonon thermal conductivity in an attempt to increase the figure of merit, and rightfully so. Most of the highest-performing thermoelectic materials incorporate some aspect of nanoengineering, whether it is nanoinclusions for select-scale phonon scattering or hierarchical structures for

multi-scale phonon scattering. It would be worthwhile pursuit to determine the effect of precursor particle size, ranging from the tens of nanometers to microns, and also the effect of bi- or tri-modal precursor particle distributions, on the crystallography and thermoelectric performance of materials prepared by uniaxial pressing and sintering. From the work proposed within this dissertation, it was found that materials prepared with micron-sized precursor powder achieved comparable performance to materials prepared via nano-sized precursor powder. Therefore, future study into particle size, size distribution and subsequent contribution to thermoelectric properties would be a valuable endeavor.

The effect of grain boundary motion as a result of annealing time and temperature, of which does not have to be a continuous curve but may encompass ramping and dwelling, is a common approach applied within the steel industry and research labs. Extrapolating these concepts to the development of semiconducting thermoelectric materials would elucidate the development of highly-coherent materials with favorable thermoelectric properties. The effects of sintering temperature and time on the stored energy and stored-energy frequency versus misorientation in relation to thermoelectric properties would provided insightful information on the relation between orientation, of which may be conduced through the release of imparted strain energy through deformation, and thermal and electrical properties. Consequently, a most inevitable future course of study would be these aforementioned effects on the thermoelectric performance of bulk bismuth telluride.

7.3 OUTLOOK

Thermoelectricity is a well-known phenomena with niche applications where steady-state operation and ability to either control temperature precisely, or generate heat, within small spaces, outweighs low thermal conversion. The realization that the use of fossil fuels have an adverse effect on the global climate has led to the development of renewable and sustainable energy technologies, of which thermoelectric devices are included. Thermoelectric devices are able to recover waste heat from virtually any process, improving process efficiency and potentially reducing cost. Even for persons not concerned with the environment, thermoelec-

tric devices are gaining interest to fullfil niche applications, such as remote power generation in harsh environment; thermoelectric devices can power sensors within a nuclear reactor during emergency conditions when no power is available, providing valuable information that could not otherwise be obtained. These motivating forces for the relatively recent renewed interest in thermoelectric device technology have provided an opportunity for the growth and development of thermoelectric devices and materials at an opportune time. These motivating forces have provided the necessary interest into thermoelectricity for the technology to gain traction and implementation in industrial settings. Will the impediment of low thermal conversion efficiency truly hinder large scale applications of thermoelectric devices for waste heat recovery applications?

Figure 58 illustrates the effect of hot-side temperature T_h on thermal conversion efficiency for materials with various ZT values with a fixed cold-side temperature T_c of 300 K. The most state-of-the art materials are just breaking a ZT value of two near room temperature, indicating relatively low thermal conversion efficiency. Increasing ZT non-linearly increases thermal conversion efficiency, and the law of diminishing returns becomes evident. Although increasing thermal conversion efficiency is an important aspect of thermoelectric device development, there is another, more pragmatic perspective to take.

If we are able to capture an overwhelming majority of the waste heat and convert that to electrical energy at a lower thermal conversion efficiency, does that outweigh catching a marginal amount of waste heat and efficiently converting it into electrical energy? With currently existing materials, it appears evident it more beneficial to focus on capturing as much waste heat as possible and converting said thermal energy into electrical energy at a lower efficiency. The integrated thermoelectric device has been demonstrated to have the same thermal conversion efficiency of a conventional thermoelectric device, but is able to produce nearly ten times the amount of electrical power as compared to the conventional device due to its ability to accept a larger heat input, exhibiting a tremendously higher power density. In the author's opinion, regardless of whether research is focused on material efficiency or device performance, pursuing the development of the field of thermoelectricty is necessary to reduce environmental impacts of fossil-fuel based processes and also aid in the implementation of RSE technologies.

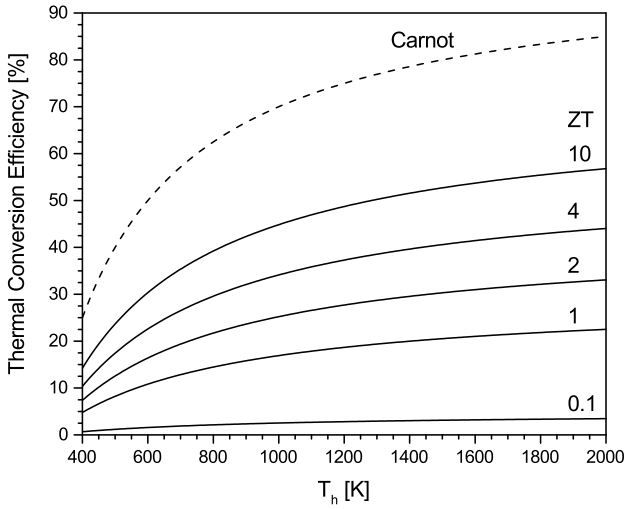

Figure 58: Thermal conversion efficiency for various ZT values versus hot-side temperature for a fixed cold-side temperature (300 K).

APPENDIX A

NOMENCLATURE

(This page is intentionally left blank.)

Variables

A	cross-sectional area, m^2
A_c	flow cross-sectional area, m^2
A_s	surface area, m^2
C_p	specific heat of fluid, J-kg^{-1}-K^{-1}
D	depth or diameter, m
D_h	hydraulic diameter, m
F	Lotgering factor, %
H	height height, m
I	electric current, A
K	thermal conductance, WK^{-1}
L	TE leg height, m
m'	ratio of resistances, dimensionless
$\overrightarrow{n}$	unit normal vector
N	number of junctions
P	pressure, MPa
P_o	power output, W
Q	heat, W
$\dot{Q}$	volumetric flow rate, m^3-s^{-1}
R	electrical or thermal resistance, Ω or KW^{-1}
$\overrightarrow{R}$	line segment vector
Ra	Rayleigh number, dimensionless
Re_{Dh}	Reynolds number, hydraulic diameter ($\rho_f U D_h/\mu$)
S_L	longitudinal spacing, m
S_T	transverse spacing, m
T	temperature, K
$\overline{T}$	average temperature, K
V	voltage, V
$\dot{\forall}$	volumetric flow rate, kg-m^{-3}
W	width, m
Z	figure of merit, dimensionless

Greek symbols

α	Seebeck coefficient, VK^{-1}
γ	ratio of area to length, m
ϵ	emissivity, dimensionless
η	thermoelectric conversion efficiency, dimensionless
θ	packing density, dimensionless
κ	thermal conductivity, W m^{-1} K^{-1}
λ	thermal conductivity, $Wm^{-1}K^{-1}$
μ	dynamic viscosity, N-s-m^{-2}
ν	kinematic viscosity, m^2-s^{-1}
ρ	electrical resistivity, Ω-m
σ	Stefan-Boltzmann constant, $5.67 \cdot 10^{-8}$ $Wm^{-2}K^{-4}$
σ_{el}	electrical conductivity, Ohm^{-1} m^{-1}
ϕ	polar angle, degrees
ψ	ratio of areas, dimensionless

Subscripts

avg	average	in	inlet/internal
ann	annealed	int	interconnector
braze	braze	j	surface j
c	cold side, compaction, contact	L	load
cer	ceramic	loss	loss term
conv	convection	m	melting
Cu	copper	max	maximum
el	electrical	N,n	n-type semiconductor
exit	exit	o	output, random orientation
e^-	electronic	oc	Seebeck potential, open circuit
FA	flow area	Ohm	Ohmic potential
g	grease	opt	optimum
gap	gap	P,p	p-type semiconductor
h	hot side	$\|\|$	parallel
hex	heat exchanger	ph	phonon, lattice
hr	hour	rad	radiation
i	surface i	total	total
res	resistive component		

APPENDIX B

RK DERIVATION

Given the thermal conductance K of the n- and p-type materials, including contact area dependent thermal contacts,

$$K = K_P + K_N + 2K_{c,P} + 2K_{c,N} = \left[\frac{A_P\lambda_P}{L_P} + \frac{A_N\lambda_N}{L_N} + 2A_P\lambda_P + 2A_N\lambda_N\right]. \tag{B.1}$$

Similarly, for the electrical resistance R of the n- and p-type materials and contacts

$$R = R_P + R_N + 2R_{c,P} + 2R_{c,N} = \left[\frac{L_P\rho_P}{A_P} + \frac{L_N\rho_N}{A_N} + \frac{2\rho_{c,P}}{A_P} + \frac{2\rho_{c,N}}{A_N}\right]. \tag{B.2}$$

Multiplying R and K yields

$$\begin{aligned} RK = \left(\frac{A_N}{A_P}\right)\left[4\lambda_{c,N}\rho_{c,P} + 2\lambda_{c,N}L_P\rho_P + \frac{2\lambda_N\rho_{c,P}}{L_N} + \left(\frac{L_P}{L_N}\right)\lambda_N\rho_P\right] + \\ +\left(\frac{A_P}{A_N}\right)\left[4\lambda_{c,P}\rho_{c,N} + 2\lambda_{c,P}L_N\rho_N + \frac{2\lambda_P\rho_{c,N}}{L_P} + \left(\frac{L_N}{L_P}\right)\lambda_P\rho_N\right] + \\ +2\left(L_P\lambda_{c,P}\rho_P + L_N\lambda_{c,N}\rho_N\frac{\rho_{c,P}\lambda_P}{L_P} + \frac{\rho_{c,N}\lambda_N}{L_N}\right) + \\ +4(\rho_{c,N}\rho_{c,N} + \rho_{c,P}\rho_{c,P}) + \lambda_P\rho_P + \lambda_N\rho_N. \end{aligned}$$

Taking the derivative of eqn. B.2 with respect to A_N/A_P and setting it equal to zero and then solving for A_N/A_P yields

$$\left(\frac{A_N}{A_P}\right) = \left(\frac{\lambda_P \rho_N \left(\frac{L_N}{2L_P}\right) + \frac{\lambda_P \rho_{c,N}}{L_P} + \lambda_{c,P}\rho_N L_N + 2\lambda_{c,P}\rho_{c,N}}{\lambda_N \rho_P \left(\frac{L_P}{2L_N}\right) + \frac{\lambda_N \rho_{c,P}}{L_N} + \lambda_{c,N}\rho_P L_P + 2\lambda_{c,N}\rho_{c,P}}\right)^{\frac{1}{2}}. \tag{B.3}$$

Similary, differentiating eqn. B.2 with respect to L_N/L_P and setting it equal to zero and solving for L_N/L_P yields

$$\left(\frac{L_N}{L_P}\right) = \left(\frac{\lambda_N \rho_P \left(\frac{A_N}{A_P}\right)}{\lambda_P \rho_N \left(\frac{A_P}{A_N}\right)}\right)^{\frac{1}{2}}. \tag{B.4}$$

BIBLIOGRAPHY

[1] D. A. Lashof, D. R. Ahuja, Relative contributions of greenhouse gas emissions to global warming.

[2] J. Hansen, M. Sato, P. Kharecha, G. Russell, D. W. Lea, M. Siddall, Climate change and trace gases, Philosophical Transactions of the Royal Society A: Mathematical, Physical and Engineering Sciences 365 (1856) (2007) 1925–1954.

[3] P. N. Pearson, M. R. Palmer, Atmospheric carbon dioxide concentrations over the past 60 million years, Nature 406 (6797) (2000) 695–699.

[4] J. Hansen, D. Johnson, A. Lacis, S. Lebedeff, P. Lee, D. Rind, G. Russell, Climate impact of increasing atmospheric carbon dioxide, Science 213 (4511) (1981) 957–966.

[5] J. Hansen, R. Ruedy, M. Sato, K. Lo, Global surface temperature change, Reviews of Geophysics 48 (4).

[6] M. Meinshausen, N. Meinshausen, W. Hare, S. C. Raper, K. Frieler, R. Knutti, D. J. Frame, M. R. Allen, Greenhouse-gas emission targets for limiting global warming to 2 c, Nature 458 (7242) (2009) 1158–1162.

[7] C. C. Mitigation, Ipcc special report on renewable energy sources and climate change mitigation.

[8] J. H. Williams, A. DeBenedictis, R. Ghanadan, A. Mahone, J. Moore, W. R. Morrow, S. Price, M. S. Torn, The technology path to deep greenhouse gas emissions cuts by 2050: the pivotal role of electricity, Science 335 (6064) (2012) 53–59.

[9] N. Panwar, S. Kaushik, S. Kothari, Role of renewable energy sources in environmental protection: a review, Renewable and Sustainable Energy Reviews 15 (3) (2011) 1513–1524.

[10] Waste heat recovery: Technology and opportunities in u.s. industry, Tech. rep., BCS, Incorporated (2008).

[11] H. C. Oersted, Experiments on the effect of a current of electricity on the magnetic needle, Matrix and Tensor Quarterly 32 (2) (1981) 60–62.

[12] H. C. Ørsted, Thermo-electricity, The Edinburgh Encyclopaedia 18 (1830) 573–589.

[13] H. Snelders, Oersteds discovery of electromagnetism, Romanticism and the Sciences (1990) 228–40.

[14] A. Ampère, Memoir on the mathematical theory of electrodynamic phenomena, uniquely deduced from experience (1826).

[15] M. Faraday, Experimental researches in electricity, Philosophical transactions of the Royal Society of London 122 (1832) 125–162.

[16] J. C. Maxwell, Xxv. on physical lines of force: Part i.–the theory of molecular vortices applied to magnetic phenomena, The London, Edinburgh, and Dublin Philosophical Magazine and Journal of Science 21 (139) (1861) 161–175.

[17] J. C. Maxwell, A dynamical theory of the electromagnetic field, Philosophical Transactions of the Royal Society of London (1865) 459–512.

[18] J. C. Maxwell, A treatise on electricity and magnetism, Vol. 1, Clarendon press, 1881.

[19] O. Heaviside, Electrical papers, Vol. 2, Cambridge University Press, 2011.

[20] O. Heaviside, Electromagnetic induction and its propagation, The Electrician 1886 (1885) 1887.

[21] O. Heaviside, Electromagnetic theory, Vol. 3, Cosimo, Inc., 2008.

[22] O. Heaviside, A gravitational and electromagnetic analogy, The Electrician 31 (18) (1893) 5125–5134.

[23] H. Hertz, W. T. B. Kelvin, Electric waves, Macmillan London, 1893.

[24] T. J. Seebeck, Ueber die magnetische polarisation der metalle und erze durch temperaturdifferenz, Annalen der Physik 82 (3) (1826) 253–286.

[25] G. S. Ohm, Vorläufige anzeige des gesetzes, nach welchem metalle die contaktelektricität leiten, Annalen der Physik 80 (5) (1825) 79–88.

[26] G. S. Ohm, Bestimmung des Gesetzes, nach welchem Metalle die Contaktelektricität leiten: Nebst einem Entwurfe zur einer Theorie des Voltaischen Apparates und des Schweiggerschen Multiplicators, Journal für Chemie und Physik, 1826.

[27] G. S. Ohm, Die galvanische Kette, mathematisch bearbeitet, Riemann, 1827.

[28] L. Graetz, Die Elektrizität und ihre anwendungen, J. Engelhorn, 1906.

[29] E. Velmre, Thomas johann seebeck and his contribution to the modern science and technology, in: Electronics Conference (BEC), 2010 12th Biennial Baltic, IEEE, 2010, pp. 17–24.

[30] J. C. A. Peltier, Nouvelles expériences sur la caloricité des courants électriques, in: Annales de Chimie et de Physique, Vol. 56, 1834, pp. 371–386.

[31] E. Lenz, Einige versuche im gebiete des galvanismus, Annalen der Physik 120 (6) (1838) 342–349.

[32] W. Thomson, On a mechanical theory of thermo-electric currents., Proceedings of the Royal Society of Edinburgh 3 (1857) 91–98.

[33] E. Altenkirch, Über den nutzeffekt der thermosäule, Physikalische Zeitschrift 10 (1909) 560.

[34] E. Altenkirch, Elektrothermische kälteerzeugung und reversible elektrische heizung, Physikalische Zeitschrift 12 (1911) 920–924.

[35] A. Joffe, Heat transfer in semiconductors, Canadian Journal of Physics 34 (12A) (1956) 1342–1355.

[36] A. Joffe, S. Airapetiants, A. Joffe, N. Kolomoetz, L. Stilbans, Increasing the efficiency of semiconductor thermocouples, Doklady Akademii Nauk Sssr 106 (6) (1956) 981–981.

[37] A. F. Ioffe, Semiconductor thermoelements and thermoelectric cooling, Infosearch London, 1957.

[38] A. F. Joffe, The revival of thermoelectricity, Scientific American 199 (1958) 31–37.

[39] A. Joffe, L. Stil'bans, Physical problems of thermoelectricity, Reports on Progress in Physics 22 (1) (1959) 167.

[40] H. Goldsmid, A. Sheard, D. Wright, The performance of bismuth telluride thermojunctions, British Journal of Applied Physics 9 (9) (1958) 365.

[41] H. Goldsmid, Principles of thermoelectric devices, British Journal of Applied Physics 11 (6) (1960) 209.

[42] U. Birkholz, Untersuchung der intermetallischen verbindung bi_2te_3 sowie der festen lösungen $bi_{2-x}sb_xte_3$ und $bi_2te_{3-x}se_x$ hinsichtlich ihrer eignung als material für halbleiter-thermoelemente, Zeitschrift Naturforschung Teil A 13 (1958) 780.

[43] D. M. Rowe, Thermoelectric waste heat recovery as a renewable energy source, International Journal of Innovations in Energy Systems and Power 1 (1) (2006) 13–23.

[44] W. Liu, Q. Jie, H. S. Kim, Z. Ren, Current progress and future challenges in thermoelectric power generation: From materials to devices, Acta Materialia 87 (2015) 357–376.

[45] G. Liang, J. Zhou, X. Huang, Analytical model of parallel thermoelectric generator, Applied Energy 88 (12) (2011) 5193–5199.

[46] T. Fujisaka, H. Sui, R. O. Suzuki, Design and numerical evaluation of cascade-type thermoelectric modules, Journal of Electronic Materials 42 (7) (2013) 1688–1696.

[47] H. Kaibe, I. Aoyama, M. Mukoujima, T. Kanda, S. Fujimoto, T. Kurosawa, H. Ishimabushi, K. Ishida, L. Rauscher, Y. Hata, et al., Development of thermoelectric generating stacked modules aiming for 15% of conversion efficiency, in: Thermoelectrics, 2005. ICT 2005. 24th International Conference on, IEEE, 2005, pp. 242–247.

[48] D. M. Rowe (Ed.), Thermoelectrics Handbook Macro to Nano, CRC Press, Taylor & Francis Group, Boca Raton, 2006.

[49] T. Caillat, J.-P. Fleurial, G. Snyder, A. Zoltan, D. Zoltan, A. Borshchevsky, Development of a high efficiency thermoelectric unicouple for power generation applications, in: Thermoelectrics, 1999. Eighteenth International Conference on, IEEE, 1999, pp. 473–476.

[50] D. Crane, D. Kossakovski, L. Bell, Modeling the building blocks of a 10% efficient segmented thermoelectric power generator, Journal of electronic materials 38 (7) (2009) 1382–1386.

[51] E. E. Antonova, D. C. Looman, Finite elements for thermoelectric device analysis in ansys, in: Thermoelectrics, 2005. ICT 2005. 24th International Conference on, IEEE, 2005, pp. 215–218.

[52] T. Kousksou, J.-P. Bédécarrats, D. Champier, P. Pignolet, C. Brillet, Numerical study of thermoelectric power generation for an helicopter conical nozzle, Journal of Power Sources 196 (8) (2011) 4026–4032.

[53] C. Gould, N. Shammas, S. Grainger, I. Taylor, A novel 3d tcad simulation of a thermoelectric couple configured for thermoelectric power generation, in: International conference on renewable energies and power quality, Spain, 2011.

[54] S. Kumar, S. D. Heister, X. Xu, J. R. Salvador, G. P. Meisner, Thermoelectric generators for automotive waste heat recovery systems part i: numerical modeling and baseline model analysis, Journal of electronic materials 42 (4) (2013) 665–674.

[55] S. Kumar, S. D. Heister, X. Xu, J. R. Salvador, G. P. Meisner, Thermoelectric generators for automotive waste heat recovery systems part ii: parametric evaluation and topological studies, Journal of electronic materials 42 (6) (2013) 944–955.

[56] S. Yu, Q. Du, H. Diao, G. Shu, K. Jiao, Start-up modes of thermoelectric generator based on vehicle exhaust waste heat recovery, Applied Energy 138 (2015) 276–290.

[57] X. Sun, X. Liang, G. Shu, H. Tian, H. Wei, X. Wang, Comparison of the two-stage and traditional single-stage thermoelectric generator in recovering the waste heat of the high temperature exhaust gas of internal combustion engine, Energy 77 (2014) 489–498.

[58] B. V. K. Reddy, M. Barry, J. Li, M. K. Chyu, Comprehensive numerical modeling of thermoelectric devices applied to automotive exhaust gas waste-heat recovery, in: ASME 2013 Heat Transfer Summer Conference collocated with the ASME 2013 7th International Conference on Energy Sustainability and the ASME 2013 11th International Conference on Fuel Cell Science, Engineering and Technology, American Society of Mechanical Engineers, 2013, pp. V001T01A047–V001T01A047.

[59] Y. Hsiao, W. Chang, S. Chen, A mathematic model of thermoelectric module with applications on waste heat recovery from automobile engine, Energy 35 (3) (2010) 1447–1454.

[60] J.-C. Jang, R.-G. Chi, S.-H. Rhi, K.-B. Lee, H.-C. Hwang, J.-S. Lee, W.-H. Lee, Heat pipe-assisted thermoelectric power generation technology for waste heat recovery, Journal of Electronic Materials (2015) 1–9.

[61] C. Liu, X. Pan, X. Zheng, Y. Yan, W. Li, An experimental study of a novel prototype for two-stage thermoelectric generator from vehicle exhaust, Journal of the Energy Institute.

[62] X. Liu, Y. Deng, Z. Li, C. Su, Performance analysis of a waste heat recovery thermoelectric generation system for automotive application, Energy Conversion and Management 90 (2015) 121–127.

[63] J. LaGrandeur, D. Crane, S. Hung, B. Mazar, A. Eder, Automotive waste heat conversion to electric power using skutterudite, tags, pbte and bite, in: Thermoelectrics, 2006. ICT '06. 25th International Conference on, 2006, pp. 343–348.

[64] D. Crane, J. LaGrandeur, Progress report on bsst-led us department of energy automotive waste heat recovery program, Journal of electronic materials 39 (9) (2010) 2142–2148.

[65] D. Crane, C. Koripella, V. Jovovic, Validating steady-state and transient modeling tools for high-power-density thermoelectric generators, Journal of electronic materials 41 (6) (2012) 1524–1534.

[66] D. Crane, J. LaGrandeur, V. Jovovic, M. Ranalli, M. Adldinger, E. Poliquin, J. Dean, D. Kossakovski, B. Mazar, C. Maranville, Teg on-vehicle performance and model validation and what it means for further teg development, Journal of Electronic Materials (2012) 1–10.

[67] D.-J. Yao, K.-J. Yeh, C.-T. Hsu, B.-M. Yu, J.-S. Lee, Efficient reuse of waste energy, Nanotechnology Magazine, IEEE 3 (2) (2009) 28–33.

[68] K. Chau, C. Chan, Emerging energy-efficient technologies for hybrid electric vehicles, Proceedings of the IEEE 95 (4) (2007) 821–835.

[69] Q. Luo, P. Li, L. Cai, P. Zhou, D. Tang, P. Zhai, Q. Zhang, A thermoelectric waste-heat-recovery system for portland cement rotary kilns, Journal of Electronic Materials (2014) 1–13.

[70] H.-K. Ma, C.-P. Lin, H.-P. Wu, C.-H. Peng, C.-C. Hsu, Waste heat recovery using a thermoelectric power generation system in a biomass gasifier, Applied Thermal Engineering.

[71] B. Xiong, L. Chen, F. Meng, F. Sun, Modeling and performance analysis of a two-stage thermoelectric energy harvesting system from blast furnace slag water waste heat, Energy 77 (2014) 562–569.

[72] D. Yang, H. Yin, Energy conversion efficiency of a novel hybrid solar system for photovoltaic, thermoelectric, and heat utilization, Energy Conversion, IEEE Transactions on 26 (2) (2011) 662–670.

[73] N. Wang, L. Han, H. He, N.-H. Park, K. Koumoto, A novel high-performance photovoltaic–thermoelectric hybrid device, Energy & Environmental Science 4 (9) (2011) 3676–3679.

[74] G. Rockendorf, R. Sillmann, L. Podlowski, B. Litzenburger, Pv-hybrid and thermoelectric collectors, Solar Energy 67 (4) (1999) 227–237.

[75] Y. Vorobiev, J. Gonzalez-Hernandez, P. Vorobiev, L. Bulat, Thermal-photovoltaic solar hybrid system for efficient solar energy conversion, Solar energy 80 (2) (2006) 170–176.

[76] E. Chávez-Urbiola, Y. V. Vorobiev, L. Bulat, Solar hybrid systems with thermoelectric generators, Solar Energy 86 (1) (2012) 369–378.

[77] W. Sark, Feasibility of photovoltaic-thermoelectric hybrid modules, Applied Energy 88 (8) (2011) 2785–2790.

[78] F. Brito, J. Martins, E. Hançer, N. Antunes, L. Gonçalves, Thermoelectric exhaust heat recovery with heat pipe-based thermal control, Journal of Electronic Materials (2015) 1–14.

[79] B. Singh, M. F. Remeli, D. L. Chet, A. Oberoi, A. Date, A. Akbarzadeh, Experimental investigation on effect of adhesives on thermoelectric generator performance, Journal of Electronic Materials (2014) 1–6.

[80] C. Tao, G. Chen, Y. Mu, L. Liu, P. Zhai, Simulation and design of vehicle exhaust power generation systems: The interaction between the heat exchanger and the thermoelectric modules, Journal of Electronic Materials (2014) 1–12.

[81] S.-Y. Hu, X. Chi, T. Shih, H. J. Schock, Heat transfer enhancement in thermoelectric power generation, Ph.D. thesis, Iowa State University (2009).

[82] B. Reddy, M. Barry, J. Li, M. K. Chyu, Mathematical modeling and numerical characterization of composite thermoelectric devices, International Journal of Thermal Sciences 67 (2013) 53–63.

[83] B. Reddy, M. Barry, J. Li, M. K. Chyu, Convective heat transfer and contact resistances effects on performance of conventional and composite thermoelectric devices, Journal of Heat Transfer 136 (10) (2014) 101401.

[84] M. Chyu, B. Reddy, M. Barry, J. Li, Enhanced heat transfer characteristics and performance of composite thermoelectric devices, Advanced Computational Methods and Experiments in Heat Transfer XII 75 (2012) 15.

[85] B. V. K. Reddy, M. Barry, J. Li, M. K. Chyu, Thermoelectric performance of novel composite and integrated devices applied to waste heat recovery, Journal of Heat Transfer 135 (3) (2013) 031706.

[86] B. V. K. Reddy, M. Barry, J. Li, M. K. Chyu, A fluid-thermo-electric coupled field analysis of a novel integrated thermoelectric device, Energy Procedia 14 (2012) 2088–2095.

[87] B. V. K. Reddy, M. Barry, J. Li, M. K. Chyu, Three-dimensional multiphysics coupled field analysis of an integrated thermoelectric device, Numerical Heat Transfer, Part A: Applications 62 (12) (2012) 933–947.

[88] B. V. K. Reddy, M. Barry, J. Li, M. K. Chyu, Enhancement of thermoelectric device performance through integratde flow channels, Frontiers in Heat and Mass Transfer (FHMT) 4 (2).

[89] B. V. K. Reddy, M. Barry, J. Li, M. K. Chyu, Thermoelectric-hydraulic performance of a multistage integrated thermoelectric power generator, Energy Conversion and Management 77 (2014) 458–468.

[90] L. Ainsworth, Single crystal bismuth telluride, Proceedings of the Physical Society. Section B 69 (6) (1956) 606.

[91] T. Harman, B. Paris, S. Miller, H. Goering, Preparation and some physical properties of bi_2te_3, sb_2te_3, and as_2te_3, Journal of Physics and Chemistry of Solids 2 (3) (1957) 181–190.

[92] F. J. Strieter, Growth of single crystal bismuth telluride, Advanced Energy Conversion 1 (1961) 125–127.

[93] J. Navratil, Z. Starỳ, T. Plechacek, Thermoelectric properties of p-type antimony bismuth telluride alloys prepared by cold pressing, Materials research bulletin 31 (12) (1996) 1559–1566.

[94] O. Ben-Yehuda, R. Shuker, Y. Gelbstein, Z. Dashevsky, M. Dariel, Highly textured bi_2te_3-based materials for thermoelectric energy conversion, Journal of applied physics 101 (11) (2007) 113707–113707.

[95] C.-N. Liao, L.-C. Wu, J.-S. Lee, Thermoelectric properties of bi-sb-te materials prepared by electric current stressing, Journal of Alloys and Compounds 490 (1) (2010) 468–471.

[96] A. Joraide, Thermoelectric properties of fine-grained sintered (bi2te3) 25-(sb2te3) 75 p-type solid solution, Journal of materials science 30 (3) (1995) 744–748.

[97] F. Yu, J. Zhang, D. Yu, J. He, Z. Liu, B. Xu, Y. Tian, Enhanced thermoelectric figure of merit in nanocrystalline bi_2te_3 bulk, Journal of Applied Physics 105 (9) (2009) 094303–094303.

[98] J. R. Sootsman, D. Y. Chung, M. G. Kanatzidis, New and old concepts in thermoelectric materials, Angewandte Chemie International Edition 48 (46) (2009) 8616–8639.

[99] T. M. Tritt, Thermoelectric phenomena, materials, and applications, Annual Review of Materials Research 41 (2011) 433–448.

[100] K. Biswas, J. He, I. D. Blum, C.-I. Wu, T. P. Hogan, D. N. Seidman, V. P. Dravid, M. G. Kanatzidis, High-performance bulk thermoelectrics with all-scale hierarchical architectures, Nature 489 (7416) (2012) 414–418.

[101] M.-P. Lu, C.-N. Liao, Mechanical and thermal processing effects on crystal defects and thermoelectric transport properties of $bi_2(se, te)_3$ compounds, Journal of Alloys and Compounds 571 (2013) 178–182.

[102] H. Ha, Y. Oh, D. Hyun, Thermoelectric properties of n-type bismuth telluride based alloys prepared by hot pressing and zone melting method.

[103] X. Ji, X. Zhao, Y. Zhang, B. Lu, H. Ni, Synthesis and properties of rare earth containing bi_2te_3 based thermoelectric alloys, Journal of alloys and compounds 387 (1) (2005) 282–286.

[104] J.-J. Shen, T.-J. Zhu, X.-B. Zhao, S.-N. Zhang, S.-H. Yang, Z.-Z. Yin, Recrystallization induced in situ nanostructures in bulk bismuth antimony tellurides: a simple top down route and improved thermoelectric properties, Energy & Environmental Science 3 (10) (2010) 1519–1523.

[105] J. Shen, Z. Yin, S. Yang, C. Yu, T. Zhu, X. Zhao, Improved thermoelectric performance of p-type bismuth antimony telluride bulk alloys prepared by hot forging, Journal of electronic materials 40 (5) (2011) 1095–1099.

[106] L. Hu, H. Gao, X. Liu, H. Xie, J. Shen, T. Zhu, X. Zhao, Enhancement in thermoelectric performance of bismuth telluride based alloys by multi-scale microstructural effects, J. Mater. Chem. 22 (5) (2012) 16484–16490.

[107] J. Yang, X. Fan, R. Chen, W. Zhu, S. Bao, X. Duan, Consolidation and thermoelectric properties of n-type bismuth telluride based materials by mechanical alloying and hot pressing, Journal of alloys and compounds 416 (1) (2006) 270–273.

[108] B. Poudel, Q. Hao, Y. Ma, Y. Lan, A. Minnich, B. Yu, X. Yan, D. Wang, A. Muto, D. Vashaee, et al., High-thermoelectric performance of nanostructured bismuth antimony telluride bulk alloys, Science 320 (5876) (2008) 634–638.

[109] Y. Ma, Q. Hao, B. Poudel, Y. Lan, B. Yu, D. Wang, G. Chen, Z. Ren, Enhanced thermoelectric figure-of-merit in p-type nanostructured bismuth antimony tellurium alloys made from elemental chunks, Nano Letters 8 (8) (2008) 2580–2584.

[110] X. Chen, L. Liu, Y. Dong, L. Wang, L. Chen, W. Jiang, Preparation of nano-sized bi_2te_3 thermoelectric material powders by cryogenic grinding, Progress in Natural Science: Materials International 22 (3) (2012) 201 – 206.

[111] J. Shen, L. Hu, T. Zhu, X. Zhao, The texture related anisotropy of thermoelectric properties in bismuth telluride based polycrystalline alloys, Applied Physics Letters 99 (12) (2011) 124102.

[112] J. Virta, J. Tervo, Experimenting with hot isostatically pressed (hip) nano grained bismuth-telluride-based alloys, in: 9TH European Conference on Thermoelectrics: ECT2011, Vol. 1449, AIP Publishing, 2012, pp. 544–547.

[113] J. Hassel, J. Tervo, Thermoelectric properties of sintered n-type and p-type tellurides, Journal of electronic materials 42 (7) (2013) 1745–1750.

[114] Y. Horio, H. Yamashita, T. Hayashi, Microstructure and crystal orientation of rapidly solidified $(bi, sb)_2$ $(te, se)_3$ alloys by the liquid quenching technique, Materials transactions 45 (8) (2004) 2757–2760.

[115] T.-S. Kim, I.-S. Kim, T.-K. Kim, S.-J. Hong, B.-S. Chun, Thermoelectric properties of p-type 25 bi_2te_3+75 sb_2te_3 alloys manufactured by rapid solidification and hot pressing, Materials science & engineering. B, Solid-state materials for advanced technology 90 (1-2) (2002) 42–46.

[116] Y. Horio, H. Yamashita, T. Hayashi, Microstructure and thermoelectric properties of hot-pressed p-type $bi_{0.5}sb_{1.5}te_3$ alloys prepared by rapid solidification technique, Materials transactions 45 (12) (2004) 3309–3313.

[117] Y. Horio, H. Yamashita, T. Hayashi, Microstructure and thermoelectric properties of hot-pressed n-type $bi_{1.9}sb_{0.1}te_{2.6}se_{0.4}$ alloys prepared using a rapid solidification technique, Materials transactions 46 (11) (2005) 2525–2529.

[118] K. F. Hsu, S. Loo, F. Guo, W. Chen, J. S. Dyck, C. Uher, T. Hogan, E. K. Polychroniadis, M. G. Kanatzidis, Cubic $agpb_msbte_{2+m}$: bulk thermoelectric materials with high figure of merit, Science 303 (2004) 818–821.

[119] F. P. Poudeu, J. D'Angelo, A. D. Downey, J. L. Short, T. P. Hogan, M. G. Kanatzidis, High thermoelectric figure of merit and nanostructuring in bulk p-type $na_{1-x}pb_msb_yte_{m+2}$, Angew. Chem. 118 (2006) 3919 –3923.

[120] A. Saramat, G. Svensson, A. E. Palmqvist, C. Stiewe, E. Mueller, Large thermoelectric figure of merit at high temperature in czochralskigrown clathrate $ba_8ga_{16}ge_{30}$, J. Appl. Phys. 99 (2006) 023708.

[121] J. Drabble, C. Goodman, Chemical bonding in bismuth telluride, Journal of Physics and Chemistry of Solids 5 (1) (1958) 142–144.

[122] T. Caillat, M. Carle, P. Pierrat, H. Scherrer, S. Scherrer, Thermoelectric properties of $(bi_xsb_{1-x})_2te_3$ single crystal solid solutions grown by the thm method, Journal of Physics and Chemistry of Solids 53 (8) (1992) 1121–1129.

[123] H. Goldsmid, F. Underwood, Study of orientation in polycrystalline bismuth telluride alloys, Advanced Energy Conversion 7 (4) (1968) 297–301.

[124] R. Franz, G. Wiedemann, Ueber die wärme-leitungsfähigkeit der metalle, Annalen der Physik 165 (8) (1853) 497531.

[125] L. Lorenz, Determination of heat temperature in absolute units, Ann. Phys. u. Chem (Leipzig) 147 (1872) 429–451.

[126] Y. Lan, A. Minnich, G. Chen, Z. Ren, Enhancement of thermoelectric figure-of-merit by a bulk nanostructuring approach, Advanced Functional Materials 20 (3) (2010) 357–376.

[127] X. Gou, H. Xiao, S. Yang, Modeling, experimental study and optimization on low-temperature waste heat thermoelectric generator system, Applied Energy 87 (2010) 3131–3136.

[128] C.-C. Wang, C.-I. Hung, W.-H. Chen, Design of heat sink for improving the performance of thermoelectric generator using two-stage optimization, Energy 39 (1) (2012) 236–245.

[129] G. Min, D. M. Rowe, Optimisation of thermoelectric module geometry for waste heat electric power generation, Journal of Power Sources 38 (1992) 253–259.

[130] M. Hodes, Optimal pellet geometries for thermoelectric power generation, Components and Packaging Technologies, IEEE Transactions on 33 (2) (2010) 307–318.

[131] A. Z. Sahin, B. S. Yilbas, The thermoelement as thermoelectric power generator: Effect of leg geometry on the efficiency and power generation, Energy Conversion and Management 65 (2013) 26–32.

[132] K. Yazawa, A. Shakouri, Cost-effective waste heat recovery using thermoelectric systems, J. Mater. Res. 27 (9) (2012) 1211–1217.

[133] G. Min, D. Rowe, Optimisation of thermoelectric module geometry for waste heatelectric power generation, Journal of Power Sources 38 (3) (1992) 253–259.

[134] M. Freunek, M. Müller, T. Ungan, W. Walker, L. M. Reindl, New physical model for thermoelectric generators, Journal of electronic materials 38 (7) (2009) 1214–1220.

[135] B. Jang, S. Han, J.-Y. Kim, Optimal design for micro-thermoelectric generators using finite element analysis, Microelectronic Engineering 88 (5) (2011) 775–778.

[136] S. W. Angrist, Direct Energy Conversion, 4th Edition, Allyn and Bacon Inc. (Boston), 1982.

[137] M. M. Yovanovich, M. Tuarze, Experimental evidence of thermal resistance at soldered joints, Journal of Spacecraft and Rockets 6 (7) (1969) 855–857.

[138] F. Meng, L. Chen, F. Sun, A numerical model and comparative investigation of a thermoelectric generator with multi-irreversibilities, Energy 36 (5) (2011) 3513–3522.

[139] D. Kraemer, K. McEnaney, M. Chiesa, G. Chen, Modeling and optimization of solar thermoelectric generators for terrestrial applications, Solar Energy 86 (5) (2012) 1338–1350.

[140] M. F. Modest, Backward monte carlo simulations in radiative heat transfer, Journal of heat transfer 125 (1) (2003) 57–62.

[141] B. Zhu, H. Schock, T. Hogan, T. Shih, A numerical study of convective and radiative heat transfer between parallel plates connected by an array of rods, in: 44th AIAA Aerospace Sciences Meeting and Exhibit. Reno: Published by the Ameri can Institute of Aeronautics and Astronautics, Vol. 1, 2006.

[142] M. Chen, L. A. Rosendahl, T. J. Condra, J. K. Pedersen, Numerical modeling of thermoelectric generators with varing material properties in a circuit simulator, Energy Conversion, IEEE Transactions on 24 (1) (2009) 112–124.

[143] M. Chen, L. A. Rosendahl, T. Condra, A three-dimensional numerical model of thermoelectric generators in fluid power systems, International Journal of Heat and Mass Transfer 54 (1) (2011) 345–355.

[144] X.-D. Wang, Y.-X. Huang, C.-H. Cheng, D. T.-W. Lin, C.-H. Kang, A three-dimensional numerical modeling of thermoelectric device with consideration of coupling of temperature field and electric potential field, Energy 47 (1) (2012) 488–497.

[145] F. Völklein, G. Min, D. Rowe, Modelling of a microelectromechanical thermoelectric cooler, Sensors and Actuators A: Physical 75 (2) (1999) 95–101.

[146] M.-J. Huang, R.-H. Yen, A.-B. Wang, The influence of the thomson effect on the performance of a thermoelectric cooler, International Journal of Heat and Mass Transfer 48 (2) (2005) 413–418.

[147] C.-H. Cheng, S.-Y. Huang, T.-C. Cheng, A three-dimensional theoretical model for predicting transient thermal behavior of thermoelectric coolers, International Journal of Heat and Mass Transfer 53 (9) (2010) 2001–2011.

[148] P. Ziolkowski, P. Poinas, J. Leszczynski, G. Karpinski, E. Müller, Estimation of thermoelectric generator performance by finite element modeling, Journal of electronic materials 39 (9) (2010) 1934–1943.

[149] C. Suter, P. Tomeš, A. Weidenkaff, A. Steinfeld, Heat transfer and geometrical analysis of thermoelectric converters driven by concentrated solar radiation, Materials 3 (4) (2010) 2735–2752.

[150] F. P. Incropera, A. S. Lavine, D. P. DeWitt, Fundamentals of heat and mass transfer, John Wiley & Sons Incorporated, 2011.

[151] J. Ishii, A. Ono, Uncertainty estimation for emissivity measurements near room temperature with a fourier transform spectrometer, Measurement science and technology 12 (12) (2001) 2103.

[152] K. H. Brosnan, G. L. Messing, D. K. Agrawal, Microwave sintering of alumina at 2.45 ghz, Journal of the American Ceramic Society 86 (8) (2003) 1307–1312.

[153] A. Bowley, L. Cowles, G. Williams, H. Goldsmid, Measurement of the figure of merit of a thermoelectric material, Journal of Scientific Instruments 38 (11) (1961) 433.

[154] M. Shimrat, Algorithm 112: position of point relative to polygon, Communications of the ACM 5 (8) (1962) 434.

[155] I. E. Sutherland, R. F. Sproull, R. A. Schumacker, A characterization of ten hidden-surface algorithms, ACM Computing Surveys (CSUR) 6 (1) (1974) 1–55.

[156] J. R. Howell, A catalog of radiation configuration factors, McGraw-Hill Book Company, 1982.

[157] I. B. Celik, U. Ghia, P. J. Roache, et al., Procedure for estimation and reporting of uncertainty due to discretization in cfd applications, Journal of fluids Engineering-Transactions of the ASME 130 (7).

[158] M. M. Barry, K. A. Agbim, M. K. Chyu, Performance of a thermoelectric device with integrated heat exchangers, Journal of Electronic Materials 44 (2015) 1394–1401.

[159] M. M. Barry, K. Agbim, B. Reddy, M. K. Chyu, Experimental investigations on the performance of a thermoelectric device with an integrated heat exchanger and flow channels, 15th International Heat Transfer Conference, Begell House, 2015.

[160] B. A. Brigham, G. J. VanFossen, Length to diameter ratio and row number effects in short pin fin heat transfer, Journal of Engineering for Gas Turbines and Power 106 (1) (1984) 241–244.

[161] D. Metzger, S. Haley, Heat transfer experiments and flow visualization for arrays of short pin fins, in: American Society of Mechanical Engineers, International Gas Turbine Conference and Exhibit, 27th, London, England, Apr. 18-22, 1982, 7 p. Research sponsored by the United Technologies Corp., Vol. 1, 1982.

[162] F. Ames, L. Dvorak, M. Morrow, Turbulent augmentation of internal convection over pins in staggered pin fin arrays, in: ASME Turbo Expo 2004: Power for Land, Sea, and Air, American Society of Mechanical Engineers, 2004, pp. 787–796.

[163] M. Chyu, V. Natarajan, J. Chiou, Y. Hsing, Effects of perpendicular flow entry on convective heat/mass transfer from pin-fin arrays, Journal of heat transfer 121 (3) (1999) 668–674.

[164] D. Vasilevskiy, J.-M. Simard, R. Masut, S. Turenne, System for simultaneous harman-based measurement of all thermoelectric properties, from 240 to 720 k, by use of a novel calibration procedure, Journal of Electronic Materials (2014) 1–10.

[165] S. Sumithra, N. J. Takas, D. K. Misra, W. M. Nolting, P. Poudeu, K. L. Stokes, Enhancement in thermoelectric figure of merit in nanostructured bi2te3 with semimetal nanoinclusions, Advanced Energy Materials 1 (6) (2011) 1141–1147.

[166] T. Zhang, J. Chen, J. Jiang, Y. Li, W. Li, G. Xu, Thermoelectric properties of the bi2te3 compound prepared by an aqueous chemical method followed by hot pressing, Journal of electronic materials 40 (5) (2011) 1107–1110.